Faculteit Wetenschappen
Departement Fysica

Strain measurement for semiconductor applications with Raman spectroscopy and Transmission electron microscopy

Meten van rek voor toepassing in halfgeleiders met Raman spectroscopie en transmissie-elektronenmicroscopie

Proefschrift voorgelegd tot het behalen van de graad van

Doctor in Wetenschappen: Fysica

aan de Universiteit Antwerpen, te verdedigen door

Viveksharma Prabhakara

Promotors:

Prof. Dr. Sara Bals

Prof. Dr. Johan Verbeeck

Prof. Dr. Wilfried Vandervorst

Antwerpen

2021

Chair person:

Prof. Dr. Pierre Van Mechelen, University of Antwerp, Belgium

Promotors:

Prof. Dr. Sara Bals, University of Antwerp, Belgium

Prof. Dr. Johan Verbeeck, University of Antwerp, Belgium

Prof. Dr. Wilfried Vandervorst, Katholieke Universiteit Leuven, Belgium

Admin:

Tania Beyers, University of Antwerp, Belgium

Members:

Prof. Dr. Paul Scheunders, University of Antwerp, Belgium

Dr. Martin Hytch, CEMES – CNRS, France

Dr. Thomas Nuytten, imec, Belgium

Table of Contents

List of abbreviations

1D	One-dimensional
2D	Two-dimensional
3D	Three-dimensional
ADC	Analog to digital converter
ADF	Annular Dark Field
ART	Algebraic reconstruction technique
CB	Conduction band
CBED	Convergent-beam electron diffraction
CCD	Charge coupled device
CUDA	Compute unified device architecture
DAC	Digital to analog converter
DFEH	Dark-field electron holography
DIBL	Drain induced barrier lowering
FBP	Filtered-Back projection
FEM	Finite-element method
FFT	Fast-Fourier transform
FIB	Focussed Ion-beam
FinFET	Fin field effect transistor
FM	Frequency modulation

FT	Fourier transform
FWHM	Full width at half maximum
GPU	Graphical processing unit
HAADF	High Angle Annular Dark Field
HCI	Hot carrier injection
HOLZ	Higher-order Laue zone
HWHM	Half width at half maximum
IOT	Internet of things
LM	Levenberg-Marquardt
LO	Longitudinal optic
MC	Mini-condenser
MOSFET	Metal-Oxide semiconductor Field effect transistor
NA	Numerical aperture
NBED	Nano-beam electron diffraction
nMOS	n-channel metal oxide semiconductor
N-PED	Nano-beam precession electron diffraction
NRMSE	Normalised root mean-square error
pMOS	p-channel metal oxide semiconductor
RAM	Random access memory
RevSTEM	Revolving scanning transmission electron microscopy

RMSE	Root mean-square error
SCE	Short channel effects
SIRT	Simultaneous iterative reconstruction technique
SNR	Signal-to-noise ratio
SRB	Strain relaxed buffer
STI	Shallow trench isolation
TO	Transverse optic
VB	Valence band

Chapter 1: Introduction

The scaling down of the size of transistors for increasing the transistor density and hence the overall computation power of integrated circuits (IC) has been a trend during the past decades. Moore's law as laid down by Gordon Moore in 1965 is an observation that the number of transistors in an elecronic chip doubles every year and this was later revised to a doubling every two years [1]. Recently, it was observed that Moore's law could not be followed due to reliability issues at the nanoscale [2,3]. The decrease in the size of the transistor channels leads to SCE (Short channel effects), power consumption in off-state and hence a loss in the optimal functionality of the transistor and coupled with increase in production cost. FinFETs (Fin Field-effect transistors) are introduced as 3D transistors that provide better electrostatic control over the channel. This enhanced control over the channel helps to overcome some of the SCE in traditional planar MOS transistors [4]. Further, finFETs have significantly higher current density and faster switching times in comparison to planar MOS transistors. Given the advancements finFETs have brought in terms of electrical performance, commercialization of finFETs began with 25 nm transistor by TSMC in 2002, dynamic random access memory by Samsung in 2004 and so on [5].

Originally strain, as induced by the use of the different materials in complex devices [6,7] was viewed as a reliability issue [8–10] , insight has emerged that dedicated strain engineering could also be used advantageously to improve transistor performance. Strain is introduced into semiconductor transistor channels by epitaxially growing materials of varying lattice parameter on top of each other, where the newly grown material conforms with the lattice parameter of the substrate material. The thickness of the strained layer is crucial as strain relaxation occurs above the critical thickness with the formation of misfit dislocations near the interface [11].

Indeed in semiconductor materials, strain modifies the bandstructure and improves or decreases the carrier transport and hence the current drive capability in transistors [12–16]. The mobility enhancement has been found to be effective using compressive stress for p-channel transistors and tensile stress for n-channel transistors [17,18]. Ge shows higher hole mobility in comparison to Si and (110) oriented Ge has higher mobility than (001) oriented Ge, which is also the case for Si [19]. Biaxial compressive stresses were shown to not improve the hole mobility significantly for both Si and Ge devices [20]. However, uniaxial compressive stress has led to maximum hole mobility enhancement in both Si and Ge. Application of uniaxial stress is also easier for short-channel transistors, while biaxial stress application is challenging for semiconductor technology nodes beyond 90 nm. The mobility increases with the application of uniaxial stress and saturates around 3 GPa for Si, while it saturates at around 6 GPa for Ge, thus enabling further enhancement in mobility for Ge in comparison to Si [21].

Since strain nowadays plays such a crucial role, monitoring strain during the development of the related semiconductor process steps as a well as during the actual production has become vital for the semiconductor industry. Strain measurement techniques for semiconductor applications ideally need to be fast (both in terms of ease of alignment, data acquisition and analysis time), precise (< 6 x 10^{-4} for strain and < 200 MPa for stress), accurate (< 1 x 10^{-3}) with spatial resolution down to 1 – 2 nm and posses a wide field of view (> 500 nm for individual devices and up to wafer scale during production).

Many strain measurement techniques have been investigated over the past decades (Table1) and so far, there hasn't been a single universal technique to measure strain at the nanoscale that ticks all the performance metrics. It can be noted that each of the techniques have their own positives and negatives and they are complementary to each other.

Table 1 Performance metrics of some of the existing strain measurement techniques. ***Warning****:the acquisition and analysis time quoted for TEM techniques in this table do not consider the sample preparation time into account. The sample preparation time can range between 3 – 4 hours depending on the complexity of the device.*

Experimental mode	Technique	Sample thickness	Spatial resolution	Precision	Accuracy	Field of view	Acquisition time (per pixel)	Analysis time
TEM	HRTEM	< 50 nm	< 2 nm	1 x 10^{-3}	2 x 10^{-3}	< 100 x 100 nm^2	2 s[a]	< 1 min
	HRSTEM	< 150 nm	< 2 nm	1 x 10^{-3}	1.5 x 10^{-3}	< 50 x 50 nm^2	3-4 µs	< 1 min
	STEM moiré [22–24]	< 150 nm	In the order of 10s of nm	1 x 10^{-3}	2 x 10^{-3}	> 200 x 200 nm^2	30 – 40 µs	< 1 min
	DFEH[25]	< 200 nm	3 – 5 nm	2 x 10^{-4}	1 x 10^{-3}	> 1 x 1 µm^2	4 – 64 s[a]	< 1 min
	CBED[26]	> 200 nm	< 2 nm	2 x 10^{-4} [27][b]	2 x 10^{-4}[b]	unlimited	~200 ms	+ 1 day
	NBED [28–30]	< 200 nm	2.7 – 5 nm	6 x 10^{-4}	2 x 10^{-3}	unlimited	30 ms	30 min[c]
	N-PED [30–32]	< 200 nm	1 - 2 nm	2 x 10^{-4}	1 x 10^{-3}	unlimited	25 ms	10 min[c]

---

[a] Total acquisition time for the full image is the same as for a single pixel due to parallel acquisition

[b] No HOLZ broadening

[c] For 100 images

	Bessel diffraction [33]	< 200 nm	< 1nm[d]	2.5 x 10^{-4}	1 x 10^{-3}	> 200 x 200 nm^2	150 ms	10 min[c]
Raman spectroscopy	Raman Oil immersion [8,34–36]	Bulk sample/ wafer	0.5 – 1 µm[e]	3 x 10^{-4}	Order of 10^{-4}[34]	mm scale	5 min[f]	30 min[c]
X-ray diffraction		Bulk sample/ wafer	0.06 - 0.3 µm	10^{-4} – 10^{-5}	Order of 10^{-4}	mm scale	10 min	5 min

TEM techniques provide the best spatial resolution for nanoscale strain analysis. However, they also need special thin samples which can lead to strain relaxation [11]. Inline techniques like Raman spectroscopy and X-ray diffraction are non-destructive, i.e. they measure the strain in its true state. However, they lack the spatial resolution for nanoscale strain analysis which is essential during the development phase of the semiconductor nanodevices. The accuracy of some of the TEM techniques is validated by measuring the lattice mismatch between an unstrained Ge sample and Si reference (discussed in detail in Chapter 2). For techniques reported in literature like DFEH (Dark-field electron holography) [37] and N-PED (nano-beam precession electron diffraction) [31], accuracy is estimated on a real strained TEM sample that is subject to sample preparation induced relaxation. The relaxation is accounted for by modelling elastic strains on a bulk device and the thin TEM lamella using FEM (Finite-element method) [38]. The TEM techniques are broadly classified into imaging and diffraction-based techniques depending on the real or diffraction space data being analysed. The precision of the TEM techniques is measured as standard deviation on a pristine/strain-free region (usually Si substrate). The real space techniques like HRTEM and HRSTEM have limited field of view and precision but are fast in terms of data analysis. STEM moiré has a wide field of view but is limited by spatial resolution (section 2.1.1.3). DFEH provides wide field of view and spatial resolution but demands more efforts in terms of aligning the microscope that is equipped with a Lorentz lens (for wide field of view) and an electron biprism. CBED (convergent beam electron diffraction) provides good precision and spatial resolution and relies on comparing the relative shifts in the HOLZ (higher-order Laue zones) as a function of strain and thus provides very high accuracy. However, in the presence of non-homogeneties in the sample along the beam direction, due to defects or strain relaxation, the HOLZ lines broaden making the analysis complicated. Often simulations are required to estimate the HOLZ broadening resulting in complicated analysis (extending up to or more than a day) [26]. Thus the technique

---

[d] Theoretical calculation (Supplementary material [33])

[e] Within an ensemble of measurement devices as small as 16 nm can be measured

[f] Even though the acquisition time per pixel is high, the pixel contains strain information of multiple nanodevices.

is not useful for industrial applications that require fast and reliable analysis. On the other hand, the CBED pattern also contains information on variations along the beam direction and a detailed analysis can uncover information on the physical properties of the sample like elastic constants and also relaxation mechanisms [39].

1.1. Stress - strain relations

In this section, we will introduce to stress and strain and also provide the basic conversion formulae using Hooke's law. Stress is a resistive force developed per unit area to an external force applied on the material. The SI unit of stress is Pascals (Pa). If the external force acting on the material tends to compress or shorten the length of the material, then it is referred to as compressive stress, whereas if the external force tends to elongate the material then it is termed as tensile stress.

Strain is the result of stress that identifies the change in the dimension of the material to its original dimension. Hooke's law provides a comprehensive relation between stress (σ) and strain (ε) and states that within the linear elastic regime (as applicable for Si and Ge in typical semiconductor applications [40]), stress and strain are directly proportional to each other.

$$\sigma = E\varepsilon \tag{1}$$

The constant of proportionality E is called the Young's modulus.

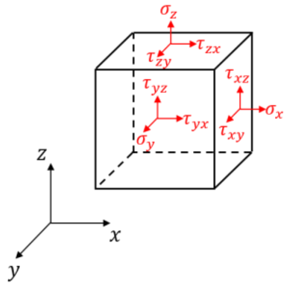

Figure 1 Stress tensor expressed on a cube which is positioned in an xyz cartesian coordinate system

Stress and strain in general are represented as second order tensors.

$$Stress\ \boldsymbol{\sigma} = \begin{bmatrix} \sigma_x & \tau_{xy} & \tau_{xz} \\ \tau_{yx} & \sigma_y & \tau_{yz} \\ \tau_{zx} & \tau_{zy} & \sigma_z \end{bmatrix} \tag{2}$$

where σ is the normal stress and τ is the shear stress represented in the cartesian coordinate system. Similarly, strain can be expressed as a 2nd order tensor:

$$Strain\ \boldsymbol{\varepsilon} = \begin{bmatrix} \varepsilon_{xx} & \varepsilon_{xy} & \varepsilon_{xz} \\ \varepsilon_{yx} & \varepsilon_{yy} & \varepsilon_{yz} \\ \varepsilon_{zx} & \varepsilon_{zy} & \varepsilon_{zz} \end{bmatrix} \tag{3}$$

ε_{xx}, ε_{yy} and ε_{zz} are the normal strains and the remaining components expressed as ε_{ij} represent the change in the displacement field [41,42] of an object in the i^th^ axis with respect to the j^th^ axis.

The stress-strain relation can now be generalised as:

$$\varepsilon_{ij} = \boldsymbol{S_{ijkl}}\sigma_{kl} \tag{4}$$

Where, $\boldsymbol{S_{ijkl}}$ is a 4th order compliance tensor that relates the stress and strain 2nd order tensors.

The compliance tensor has in total 81 elastic coefficients. For a general linear anisotropic elastic solid, owing to the symmetry of stress-strain tensors the number of independent elastic coefficients are reduced to 21. Any pair of indices ij (or ji) are reduced to single indices. The widely used notations are $11 \rightarrow 1$, $22 \rightarrow 2$, $33 \rightarrow 3$, $23 \rightarrow 4$, $31 \rightarrow 5$ and $12 \rightarrow 6$ [43]. For Si and Ge cubic symmetries oriented along x = [100], y = [010] and z = [001] the compliance contains a few independent components and can be expressed as [43]:

$$\boldsymbol{S} = \begin{bmatrix} s_{11} & s_{12} & s_{12} & 0 & 0 & 0 \\ s_{12} & s_{11} & s_{12} & 0 & 0 & 0 \\ s_{12} & s_{12} & s_{11} & 0 & 0 & 0 \\ 0 & 0 & 0 & s_{44} & 0 & 0 \\ 0 & 0 & 0 & 0 & s_{44} & 0 \\ 0 & 0 & 0 & 0 & 0 & s_{44} \end{bmatrix} \tag{5}$$

The semiconductor devices are normally oriented along $x_s = [110]$, $y_s = [-110]$ and $z_s = [001]$. The stress strain relations [35,44] in this rotated system of axes (x_s, y_s, z_s expressed as 1,2,3 for simplicity) and for a triaxial normal stress condition predominant in the epitaxially grown semiconductor devices is expressed as:

$$\begin{bmatrix} \varepsilon_{11} \\ \varepsilon_{22} \\ \varepsilon_{33} \\ 2\varepsilon_{23} \\ 2\varepsilon_{31} \\ 2\varepsilon_{12} \end{bmatrix} = \begin{bmatrix} s'_{11} & s'_{12} & s_{12} & 0 & 0 & 0 \\ s'_{12} & s'_{11} & s_{12} & 0 & 0 & 0 \\ s_{12} & s_{12} & s_{11} & 0 & 0 & 0 \\ 0 & 0 & 0 & s_{44} & 0 & 0 \\ 0 & 0 & 0 & 0 & s_{44} & 0 \\ 0 & 0 & 0 & 0 & 0 & s'_{44} \end{bmatrix} \begin{bmatrix} \sigma_{11} \\ \sigma_{22} \\ \sigma_{33} \\ 0 \\ 0 \\ 0 \end{bmatrix} \tag{6}$$

$$
\text{Where, }\begin{aligned} s'_{11} &= \frac{1}{2}(s_{11}+s_{12})+\frac{1}{4}s_{44} \\ s'_{12} &= \frac{1}{2}(s_{11}+s_{12})-\frac{1}{4}s_{44} \\ s'_{44} &= 2(s_{11}-s_{12}) \end{aligned}
$$

This implies that the compliance matrix is rotated to accommodate for the change in the direction axes. Eq.6 gives a direct transformation from stress to strain and vice-versa under the elastic regime and will be used throughout the thesis for stress – strain conversions.

1.2. FinFETs – from planar to 3D structures

In this section, we introduce to the FinFETs and the 16 nm fins developed by imec which is used for experimental analysis in the thesis. In general, FinFETS are 3D transistors in which the gate is partially wrapped around the channel of the transistor (Figure 2). Sometimes, the gate is placed on many locations along the length of the channel forming multi-gate device structure. The gate makes contact on the left and right side of the channel, which provides better electrostatic control over the channel, enhanced switching characteristics and overcomes other deteriorating short channel effects (SCE) predominant in planar MOS transistors [45]. Thus, finFETs enable extending the gate scaling beyond the planar transistor limits.

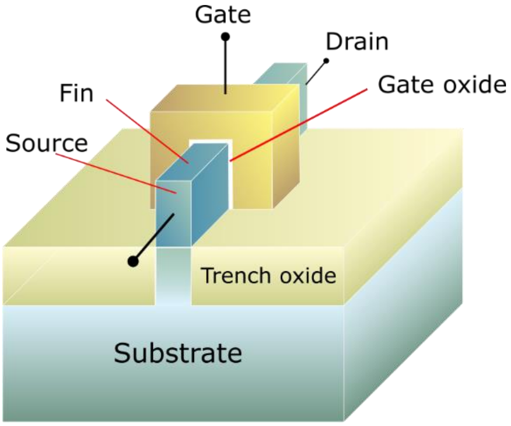

Figure 2 Schematic of a finFET structure. The channel is wrapped by the gate giving better electrostatic control over the channel

The device used for investigation in this thesis is the device stack of a 16 nm finFET developed by imec using the STI-first technique [46] as shown in Figure 3. This sample consists of a silicon substrate on top of which a thick $Si_{0.3}Ge_{0.7}$ layer (~110 nm) is grown epitaxially which is expected to be relaxed completely (due to a high aspect ratio, the structure relaxes by the formation of dislocations). Then a thin layer (~30 nm) of Ge is grown on top of the SRB which will become the channel of the finFET. The fins are 16nm in width and are separated by SiO_2 (Shallow Trench Isolation, STI) using a pitch width of 200 nm. This type of arrangement is beneficial to measure strain from Raman spectroscopy and further explanation about this is given in Chapter 6. The V shape of the Si substrate in the cross section is used especially to trap the defects in the SRB and prevent their propagation into the Ge channel. The gate is still not incorporated into the device as the intention would be to study the strain induced due to the epitaxial growth strategy.

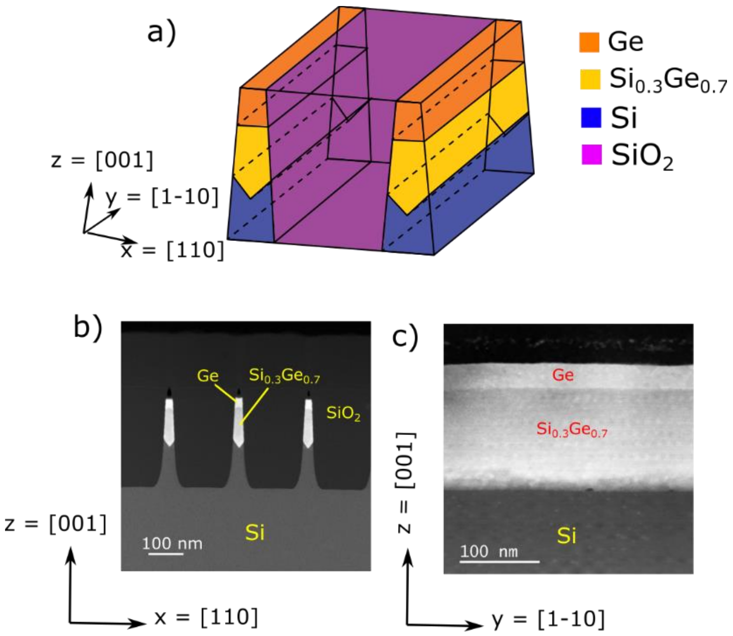

Figure 3 a) Schematic description of the FinFET developed by imec b) Cross section and c) long section of the 16 nm finFET obtained for TEM strain analysis.

Figure 3b and Figure 3c show the HAADF image of the TEM lamellae prepared along the cross section and long section of the finFET, which will be used for TEM strain analysis.

In the next chapter, we explore some of the existing TEM techniques and the Raman technique and discuss their working principles and performance metrics on a reference sample (unstrained Ge on Si).

Chapter 2: Overview of the existing strain measurement techniques

The inline techniques like Raman spectroscopy [36,47] although offering very high strain precision (1-2 x 10^{-4}) lack the spatial resolution required to fulfil the demand for local strain measurement for the latest technology node of semiconductor devices[48] having devices smaller than 20 nm. However the technique is fast, non-destructive and provides accurate and precise measurements on an ensemble of nanodevices and thus increasing the statistical relevance of the strain measurements. The statistical relevance is important as long as the interdevice variation is kept small which is the goal of the semiconductor industry.

With the potential trends of scaling down chip sizes beyond 3 nm in the near future [49], only TEM techniques have the capability to provide the required spatial resolution (< 1 nm) for strain analysis, crystallographic mapping, defect analysis etc. at the nanoscale and even down to single unit cell. The downside is the preparation of special thin FIB (focussed ion beam) samples (~200 nm) which leads to strain relaxation that can hinder the measurement of true strain state. Hence, Raman being a non-invasive and fast technique potentially serves for inline process control and optimization and TEM is often used for closer inspection at the nanoscale during the development phase. In this chapter, we will discuss some of the existing strain measurement techniques in TEM and Raman and expand upon their usefulness and limitations.

2.1. TEM techniques

The TEM techniques can be broadly classified into 1) Imaging techniques and 2) Diffraction techniques depending on the space in which the data is acquired. Imaging techniques make use of real space image or data, while diffraction techniques rely on diffraction patterns (analogous to Fourier space).

2.1.1. Imaging techniques

2.1.1.1. HR(S)TEM and Geometric phase analysis:

High-resolution transmission electron microscopy (HRTEM) and high-resolution scanning transmission electron microscopy (HRSTEM) techniques provide the capability to image atomic resolution projection images of the atomic columns of the crystal lattice. HRSTEM can be applied to slightly thicker TEM samples up to approximately 200 nm, whereas the image contrast greatly reduces for HRTEM for samples thicker than ~50 nm. A typical HAADF-STEM operates in raster scan mode where the beam scans over the sample in a row by row manner. This creates a fast scan direction for the rows and slow scan direction for the columns as illustrated in Figure 4.

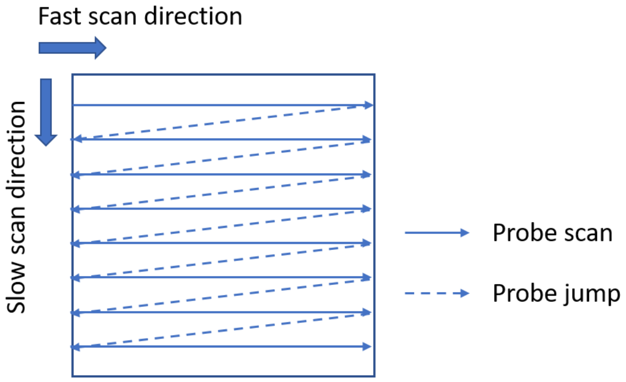

Figure 4 Schematic of the Raster scanning scheme in STEM

Consequently, artefacts appear in the slow scan direction due to sample drift, thermal or mechanical instabilities as we will further discuss in chapter 4. Many image correction techniques are proposed in literature to correct for the slow scan artefacts that typically work with multiple fast acquisitions and later correcting the image series with rigid/non-rigid registration [50]. The field of view is rather limited (< 50 nm) with such fast acquisitions due to the required time to scan large areas with atomic resolution sampling.

Typically, to analyse strain in these atomic resolution images, post processing is performed using methods like GPA (Geometric Phase Analysis) [51]. GPA is a popular image processing technique that computes strain in a high-resolution image by extracting the displacement field that is embedded in the geometric phase of the lattice fringes. Any high-resolution image of a crystal is periodic and is composed of its Fourier components which are also referred to as lattice fringes. Any particular lattice fringe can be represented as a function of its position $\vec{r}$ [51] (The arrow on the top is an indication it is a vector):

$$B_{\vec{g}}(r) = 2A_{\vec{g}}\cos\left(2\pi\vec{g}\cdot\vec{r} + p_{\vec{g}}\right) \tag{7}$$

Where, $A_{\vec{g}}$ is the amplitude of the fringe, $\vec{g}$ the reciprocal lattice vector and $p_{\vec{g}}$ is the initial phase determining its relative position. Note that (·) represents the dot product between the vectors. In the presence of a displacement field $\vec{u}$, $\vec{r} \rightarrow \vec{r} - \vec{u}$ the lattice fringe eq.7 becomes:

$$B_{\vec{g}}(\vec{r}) = 2A_{\vec{g}}\cos\left(2\pi\vec{g}\cdot\vec{r} - 2\pi\vec{g}\cdot\vec{u}(\vec{r}) + P_{\vec{g}}\right) \tag{8}$$

Thus, we can define $P_{\vec{g}}(\vec{r})$, a phase component which contains information of the displacement field $\vec{u}$

$$P_{\vec{g}}(\vec{r}) = -2\pi\vec{g}\cdot\vec{u}(\vec{r}) \tag{9}$$

After decomposing Eq.8 into a sum of exponentials, and selecting either positive or negative exponential term (in this case positive exponential is selected for illustration):

$$H_{\vec{g}'}(\vec{r}) = A_{\vec{g}}(\vec{r})exp\left(2\pi i\vec{g}\cdot\vec{r} + iP_g(r)\right) \qquad (10)$$

In practice, the selection of either positive or the negative exponential (here we refer to as reflection) is performed after computing the Fourier transform of a high resolution image and filtering out the particular reflection using a circular mask. Two such non-collinear reflections are selected and the phase from each reflection $\vec{g}_1(\ \vec{g}_2)$ $P_{\vec{g}_1}(\vec{r})$ $(P_{\vec{g}_2}(\vec{r}))$ is given by (ignoring the constant initial phase term $p_{\vec{g}}$):

$$P_{\vec{g}_1}(r) = -2\pi\vec{g}_1\cdot\vec{u}(\vec{r}) = \ -2\pi\left[g_{1x}u_x(r) +\ g_{1y}u_y(r)\right] \qquad (11)$$

$$P_{\vec{g}_2}(r) = -2\pi\vec{g}_2\cdot\vec{u}(\vec{r}) = \ -2\pi\left[g_{2x}u_x(r) +\ g_{2y}u_y(r)\right] \qquad (12)$$

Eqs.11 and 12 form a set of two linear equations with two unknowns $u_x(\vec{r})$ and $u_y(\vec{r})$, which forms the components of the displacement field in the xy cartesian coordinate system. Solving eqs.11 and 12 gives the displacement field:

$$\begin{pmatrix} u_x \\ u_y \end{pmatrix} = -\frac{1}{2\pi}\begin{pmatrix} g_{1x} & g_{1y} \\ g_{2x} & g_{2y} \end{pmatrix}^{-1}\begin{pmatrix} P_{\vec{g}_1} \\ P_{\vec{g}_2} \end{pmatrix} \qquad (13)$$

Finally, the strain tensors from the 2D image are calculated using the above eqns.

$$\begin{pmatrix} \varepsilon_{xx} & \varepsilon_{xy} \\ \varepsilon_{yx} & \varepsilon_{yy} \end{pmatrix} = -\frac{1}{2\pi}\begin{pmatrix} a_{1x} & a_{2x} \\ a_{1y} & a_{2y} \end{pmatrix}\begin{pmatrix} \frac{\partial P_{\vec{g}_1}}{\partial x} & \frac{\partial P_{\vec{g}_1}}{\partial y} \\ \frac{\partial P_{\vec{g}_2}}{\partial x} & \frac{\partial P_{\vec{g}_2}}{\partial y} \end{pmatrix} \qquad (14)$$

HR(S)TEM combined with GPA provides a fast, reliable measurement with good precision and accuracy [52,53]. Figure 5 shows the strain map on 16nm finFET along the long-section obtained from HRSTEM and GPA. We can observe the effect of slow scan distortions in the ε_{zz} strain map resulting in the horizontal line artefacts and the effect is pronounced while imaging higher fields of view where higher dwell times (pixel acquisition time) of 20-50 µs is used to ensure the probe positioning is stabilised and a good SNR (signal-to-noise ratio) is available. Thus lower fields of view (~50 nm) are usually imaged in HRSTEM which permits for shorter dwell times (upto 2 µs) and in combination with scan distortion correction routines such as multi-frame scanning and using rigid or non-rigid registration to average the multiple frames to estimate and correct for deformations in the images [50]. More details on overcoming the slow scan distortions while imaging larger fields of view (upto 200 nm) are discussed in chapter 4. HRSTEM with GPA provides good precision around 1 x 10^{-3} (over 3 nm spatial resolution) and the precision depends inversely on the size of the mask used in FFT (Fast-Fourier transform) to filter out frequencies/reflections which further dictates the strain spatial resolution. The accuracy was predicted to be around 1.5 x 10^{-3} [52]. The GPA post-processing is extremely fast and requires less than 1 minute and has the possibility for real time applications by further enhancing the speed using system level programming languages like C++. The drawbacks of HRSTEM are limitations in field of view (< 50 nm) implying reduced slow scan artefacts using image correction routines.

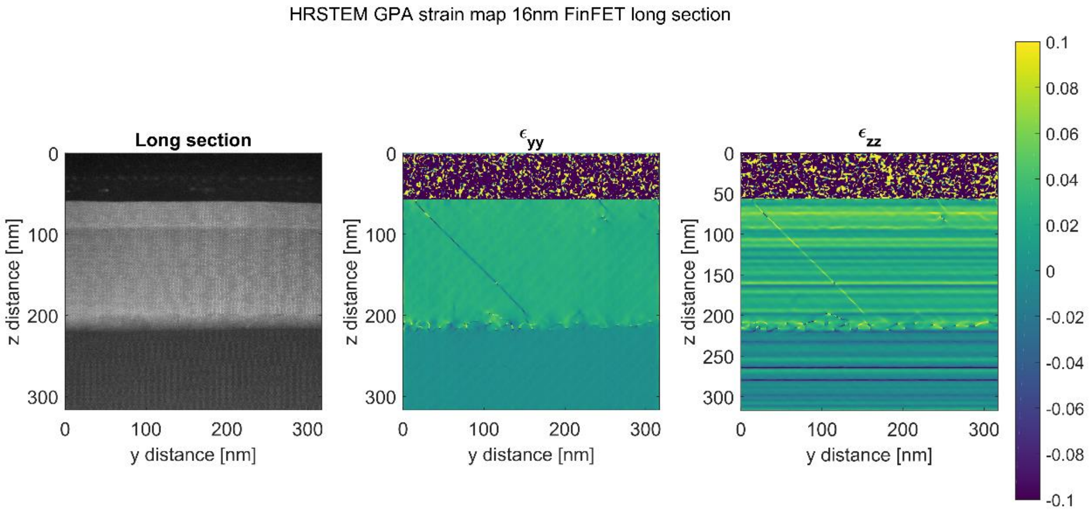

Figure 5 HRSTEM with GPA strain map on the 16 nm finFET long-section TEM sample. Notice the horizontal line artefacts in ϵ_{zz} due to the scan distortion and sample drift.

2.1.1.2. Dark-field electron holography:

Dark-Field electron holography (DFEH) was proposed by Hytch et.al [37] which is a real space based technique that uses a biprism to interfere coherent beams from a reference region on the sample and the strained region. The sample is tilted to the two-beam condition[g] to increase the intensity in the specific diffracted beam of interest and the objective aperture is used to select the diffracted electron beams from the lattice planes of interest. The incoming beam is split and passed through the reference and strained region in the sample. The phase image is reconstructed from the resulting dark field interference pattern or the hologram from the reference and strained regions. Finally, the strain maps are calculated from the resulting phase images using GPA processing. Hytch et.al. have also laid down the genesis and

---

[g] The the sample is tilted with respect to the incoming electron beam direction which results in a single strongly diffracted beam while the rest of the diffracted beams are weak in intensity.

theoretical understanding to the holographic dark-field technique[h] [25]. The dark field interference pattern or fringe essentially contains the phase difference between the two paths i.e. from the diffracted beams in the reference region and the region of interest/ strained region. The phase contribution can be written as the sum of four principal components:

$$\phi_{\vec{g}}(\vec{r}) = \phi_{\vec{g}}^{G}(\vec{r}) + \phi_{\vec{g}}^{C}(\vec{r}) + \phi_{\vec{g}}^{M}(\vec{r}) + \phi_{\vec{g}}^{E}(\vec{r}) \tag{15}$$

Where, G,C,M,E refers to the contributions from geometric phase, crystalline lattice, magnetic contribution and electric fields. The geometric phase term here relates exactly to the phases analysed in the GPA processing as explained earlier. Strain introduces a displacement field $\vec{u}$ into the crystal lattice where the positional coordinate $\vec{r} \rightarrow \vec{r} - \vec{u}$ would result in the geometric phase term as a function of $\vec{r}$:

$$\phi_{\vec{g}}^{G}(\vec{r}) = -2\pi\vec{g} \cdot \vec{u}(\vec{r}) \tag{16}$$

It is important to have a uniform thickness of the sample so that the amplitude of the diffracted beams from the reference region and the strained region remain the same and to ensure maximum dark field interference fringe contrast. Under the first approximation, the crystalline and electrostatic phases cancel out (or a constant phase change is produced) for uniformly thick samples and are not directly dependent on the strain and a direct measurement of the geometric phase becomes possible. Another stringent requirement in terms of sample preparation for the DFEH strain measurement involves maintaining a constant crystalline phase i.e., any changes to the diffraction conditions, for example on regions exhibiting bend contours should be avoided. The geometric phase information is absent in the transmitted beam (zeroth order Bragg reflection) and this configuration serves as a means for assessing and correcting the systematic errors for the DFEH.

Two non-collinear diffraction beams are necessary to calculate the 2D strain tensor, and the sample is tilted in the two beam conditions for maximizing the intensities in the two diffracted beams. There can always be some sample or image shift between the two holograms due to the reorientation of the crystal to the new diffraction condition in between the data acquisition. Equivalent sample areas could be identified due to a wide field of view (~1 µm) and by analysing the phase and amplitude images of the hologram it is possible to correct for image shifts. However, it can be challenging for uniformly layered samples.

The technique offers good spatial resolution (3 - 5 nm), good accuracy (1 x 10^{-3}) and precision (2 x 10^{-4}) with a an excellent field of view up to 1 µm. However, the spatial resolution is tuneable and increasing the spatial resolution for the latest technology node semiconductor devices (< 3nm) would

---

[h] We use the same notations as described in the original paper of DFEH for the sake of consistency

compromise the field of view [54]. Although the technique provides excellent performance metrics for strain measurement, it demands more efforts in terms of alignment and requires a stable microscope equipped with Lorentz lens for large field of view mapping [26]. Cooper.et.al [55] examined electron dose dependence of precision (standard deviation of strain on a reference Si sample) by acquiring DFEH data at multiple acquisition times varying from 4 – 64 seconds. The reported precision values varied from 2 x 10^{-3} to 5 x 10^{-4} and is inversely proportional to the acquisition time due to increase in SNR with acquisition time/ electron dose.

2.1.1.3. STEM moiré technique

The STEM moiré technique is a methodology to increase the field of view of the STEM image while maintaining local strain information. Moiré fringes are used throughout a wide variety of applications in physics and engineering to bring out small variations in an underlying lattice by comparing with another reference lattice. This method was recently demonstrated in STEM to provide local strain measurement in crystals by comparing the crystal lattice with the scanning raster that then serves as the reference [22]. A moiré pattern is created in STEM by intentionally imaging at lower magnification where the step size or the pixel size becomes very close to the lattice spacing [23]. Moiré interference is a phenomenon based on the interference between two nearly identical patterns and STEM moiré can be understood as the interference between the periodic crystal lattice and the scanning grid created by the STEM probe. The scanning grid is the periodic arrangement of the points sequentially visited by the STEM probe. The scanning grid is easily tuneable in the STEM mode and hence provides the flexibility for adjusting the interference phenomenon and hence the moiré pattern. STEM moiré theory and formation is more formally explained in terms of the sampling theory used in digital signal processing. The Nyquist criterion states that the minimum frequency required to sample a signal should be twice the highest frequency of the signal under consideration [56]. Figure 6 illustrates the moiré effect in the frequency domain.

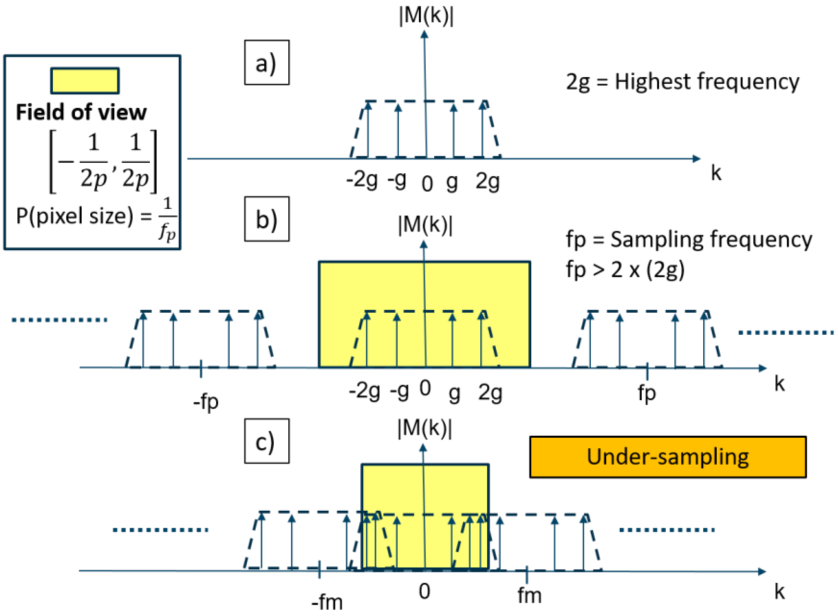

Figure 6 a) Frequency spectrum of an example signal with discrete frequency components with the highest frequency at 2g b) Frequency spectrum of the data after sampling with the frequency fp.The replicas of the central band are centered at the integral multiples of the sampling frequency fp. The sampling frequency fp > 2 x highest frequency and the Nyquist criterion is satisfied and the frequency bands do not overlap resulting in the complete representation of the data inside the visible Fourier space $\left[-\frac{1}{2p},\frac{1}{2p}\right]$, *which is equal to the sampling frequency (represented in yellow) c) Formation of the moiré due to the overlapping frequency components from the sampling replicas caused by undersampling*

Figure 6 a shows the frequency spectrum of a hypothetical signal with discrete frequency response with the maximum frequency given by 2g. Sampling the signal with a frequency fp that is greater than twice 2g (Nyquist criterion) results in the frequency response as shown in Figure 6b. The replicas of the central frequency are centred at an integral multiple of the sampling frequency fp and they do not overlap. The visible Fourier space is restricted to $\left[-\frac{f_p}{2},\frac{f_p}{2}\right]$ in the frequency domain. Under-sampling or sampling with a frequency less than two times 2g results in the replicas to overlap and the frequency response is not identical to the original data. This is called as 'aliasing' or the moiré effect. A more detailed analysis will follow in chapter 3.

The STEM moiré effect in general has been exploited in a number of applications including: 1) low dose imaging [57] on beam sensitive organic compounds 2) extended field of view in comparison to HR(S)TEM [24] 3) evaluation of strain, rotation and defects [58] in functional oxides and crystallographic materials [59]. The technique is advantageous for fast data acquistion and analysis. The moiré imaging technique relies on image processing algorithms like GPA for extracting strain information. The spatial resolution of the moiré technique is inferior to the HR(S)TEM imaging due to the higher spacing of the moiré fringes in comparison to the crystal lattices in case of HR(S)TEM. STEM moiré is also prone to the drift and scan artefacts in the slow scan direction as seen for HRSTEM. Both HRSTEM and STEM moiré require reference region in the field of view for strain analysis. However, the significance of sample drift is much lower due to the magnification of moiré imaging which is around 0.5 to 1 order lower than HRSTEM. The scan noise due to scan fluctuations are still apparent in the geometric phase information for the moiré technique. The performance would be similar to that of HR(S)TEM with precision around 1 x 10^{-3} for spatial resolution of 3 nm, accuracy around 2 x 10^{-3} [60] field of view upto 250 nm.

2.1.2. Diffraction techniques

Diffraction techniques mainly rely on data from the diffraction space and extract the spatial distribution and fine structures in the diffraction patterns. In general, diffraction patterns are directly connected to the lattice parameters of the material under investigation. Unlike imaging techniques, diffraction techniques are less sensitive to sample drift and scan distortions. Thus, they provide better precision in comparison to imaging techniques that operate in the scanning mode. In this section, we will introduce to some of the TEM diffraction based techniques widely used in the field of semiconductor strain analysis.

2.1.2.1. Nano-beam electron diffraction (NBED)

Nano-beam electron diffraction is a technique in which a quasi parallel probe is used to produce ideally spot diffraction patterns or diffraction discs with a relatively small radius [28–30,61]. Figure 7 shows the diffraction pattern acquired by NBED for a Si sample using a Thermo Fischer Titan, aberration corrected microscope operated at 300 kVolt acceleration voltage. The condenser aperture (C2) is 20 µm in diameter and the convergence angle of the beam on the sample is ~ 0.2 mrad (in the microprobe mode (Appendix A 1.1.1.3). The spatial resolution NBED offers is measured to be around ~2.7 – 5 nm [29,62].

In general, variations in the lattice parameters of the material results in consequent variation in the positions of the center of diffraction spots or discs in the diffraction pattern according to Bragg's law [63]. The key for strain analysis is to identify the relative shift of the center of these spots with respect to a reference diffraction pattern. For NBED, the autocorrelation of the diffraction patterns is performed, where the peaks of the autocorrelation function coincide with the center of the discs. The coordinates of the center of discs are calculated at sub-pixel resolution using a paraboloid or disc-fit. Commercial software called "Epsilon", version: 1.2.1.40 from Thermo Fisher Scientific is used for our NBED analysis.

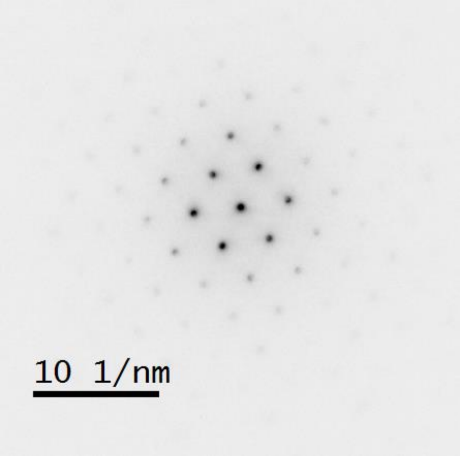

Figure 7 Nano-beam diffraction pattern of Si in [110] zone axis

Experimentally, the quasi-parallel probe scans across the region of interest on the sample and diffraction patterns are acquired at every beam positions on the sample. Each diffraction pattern is compared with a reference diffraction pattern (usually Si substrate[i]) and the strain tensor is computed for each beam position. Note that the strain measured here is actually the lattice mismatch between Si and the strained region. A conversion has to be done to measure strain with respect to the bulk material (Appendix 5)

The 2D distortion matrix D, strain ε and rotation Ω are calculated as:

$$D = (G^t)^{-1} G_0^t - I \tag{17}$$

$$\varepsilon = \frac{1}{2}(D + D^t) \tag{18}$$

$$\Omega = \frac{1}{2}(D - D^t) \tag{19}$$

Where G and G_0 are the reciprocal vectors from the strained and reference diffraction patterns and I is the identity matrix. The accuracy and precision of the technique has been assessed on a bulk Ge sample with the reference Si substrate (Appendix A2.2) as shown in Figure 8. The average lattice mismatch between Ge and Si is measured (~100 nm away from the interface due to presence of misfit dislocations near the Si-Ge interface in these strain relaxed systems [11]) and compared with the theoretical value which gives the accuracy of the technique. The precision is measured as the standard deviation of the measured strain on the reference unstrained/pristine Si region. Accordingly, the accuracy is measured at 2.5 x 10^{-3} and precision as 7 x 10^{-4}. The measured precision is close to the reported precision of 6 x 10^{-4} in literature for a spatial resolution of 3 nm [26].

---

[i] The strain measured in this case is the lattice mismatch between the region of interest and the reference Si substrate.

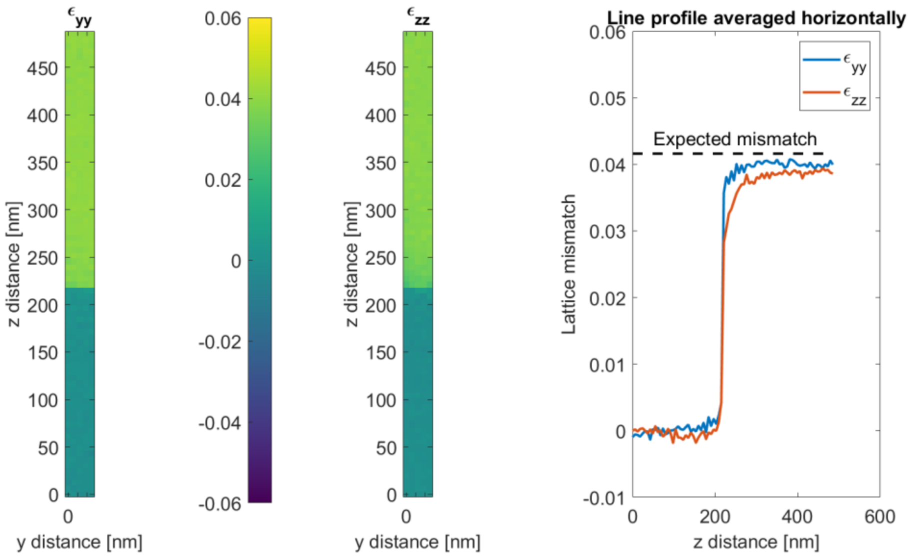

Figure 8 Strain map using NBED on Ge layer on top of Si substrate. The Si substrate is used as the reference for lattice mismatch calculation. The line profile averaged horizontally is spanning from Si to the Ge region. The horizontal line shows the expected mismatch between lattice parameters for Ge and Si.

Multiple or dynamic scattering in electron diffraction experiments is a fundamental problem related to a very strong interaction between the electron beam and the sample. The electrons are scattered multiple times within the specimen, leading to several unwanted effects, from nonlinearities in the intensity of the diffracted beams to a nonhomogeneous shape of the diffracted discs, significantly complicating the extraction of structural information. Hence, a quasi-parallel probe is used in NBED as opposed to a converging probe in HRSTEM which is intended to keep the diffraction discs as small as possible in order to avoid redistribution of intensities within the discs stemming from multiple elastic scattering processes and thus limiting the spatial resolution. Precession was introduced to NBED (Nanobeam electron diffraction with precession (N-PED)) to circumvent multiple scattering problem and the approach leads to averaging out diffraction patterns acquired at different tilt angles, thus partially cancelling the influence of multiple scattering. The intensity in the diffraction spots becomes more uniform resulting in an improved precision better than 2×10^{-4}, accuracy 1×10^{-3} [31,53] and spatial resolution of 2 nm. The technique relies on specialised hardware to tilt the incoming beam direction (upto 0.5° to 2°) with respect to the main crystallographic direction. Consequently, the electrons are weakly scattered inside the crystal and thus reducing the multiple scattering effect. The direction of the incident beam is kept constant while the incidence angle is varied azimuthally and the patterns are averaged over different configurations. This results in quasi-kinematical diffraction patterns which are easier to interpret [32].

2.1.2.2. Bessel diffraction technique

Bessel diffraction was introduced by Guzzinatti.et.al [33] to reduce the hardware complexity in N-PED for strain measurement. The main idea behind Bessel diffraction is to realise a hollow-cone illumination where the rays from different directions are present simultaneously, instead of sequential illumination in the case of N-PED. This is achieved by placing a ring/annular shaped aperture in the condenser C2 lens plane (Figure 9a). This greatly minimizes the hardware complexity for the case of N-PED where the beam is tilted and rotated at each scan position in the sample plane and a corresponding “untilting” required below the sample plane to obtain spot diffraction patterns [64–66].

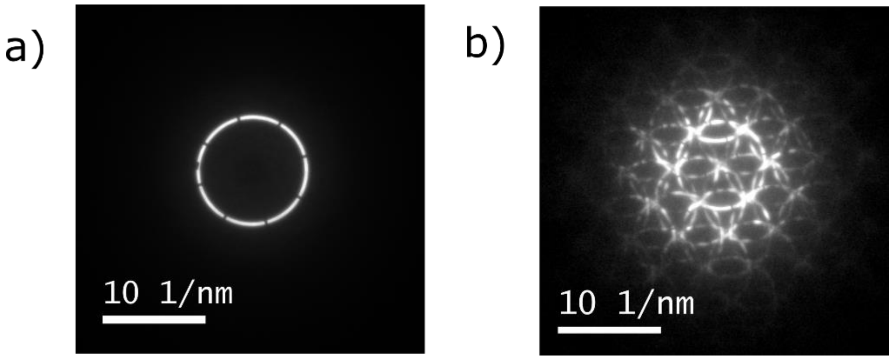

Figure 9 a) Image of the Bessel aperture (Imaged in the diffraction plane with no sample in place) b) Bessel diffraction pattern from Si substrate oriented at [110] zone axis

The conical illumination from an infinitely thin annular aperture is described by a Bessel auxillary function and hence the name “Bessel diffraction”. In a realistic scenario, the aperture has a finite width annulus (space between the inner and outer rings) and hence the Bessel beams are only an approximation to the conical illumination from an infinitely thin annular aperture [67,68] as stated in the original paper. The diffraction pattern created by Bessel diffraction is different from the NBED/N-PED where the spots are replaced by rings as shown in Figure 9b. This requires treating the diffraction data with a dedicated analysis, based on computing the autocorrelation of each diffraction pattern and subsequent extraction of the centre of the rings after background extraction and normalization [69,70].

Figure 10 shows the strain map of unstrained bulk Ge on top of Si TEM sample as investigated earlier in section 2.1.2.1. This unstrained sample system (Appendix A2.2) serves as a ground truth to access the accuracy and precision of the technique independent of sample non-homogeneties due to for example strain relaxation. The accuracy and precision was measured at 1 x 10^{-3} and 5 x 10^{-4}. As been discussed earlier in section 2.1.2.1, the accuracy is measured by comparing the average lattice mismatch between Ge and Si (~100 nm away from the interface due to presence of misfit dislocations near the Si-Ge interface in these strain relaxed systems [11]) and the theoretical value. The precision is the standard deviation of the measured lattice mismatch on the reference unstrained/pristine Si region.

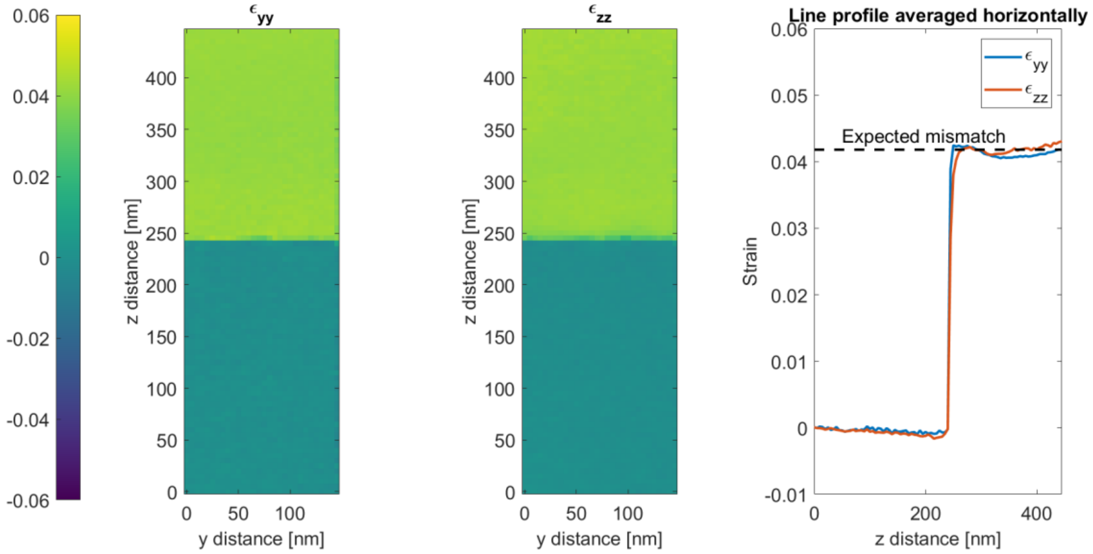

Figure 10 Strain map using Bessel diffraction on Ge sample on top of Si substrate. The Si substrate is used as the reference for strain calculation. The line profile averaged horizontally is spanning from Si to the Ge region. The horizontal line shows the expected theoretical mismatch between lattice parameters for Ge and Si.

The experiment was done using Thermofischer Titan microscope operating at 300 kV acceleration voltage. The convergence angle was given by $\alpha \approx 6\ mrad$. Because the convergence angle was slightly lower than the Bragg angle, large overlaps of the rings are avoided that can complicate the analysis. Choosing even lower convergence angles however, reduces the spatial resolution.

In general, the precision of the TEM techniques can vary depending on the sample and the experimental conditions, for example the variations can be attributed to the thickness of the sample under investigation, the electron dose used [71] for acquisition and hence the overall SNR of the dataset. Hence, a determination of optimal electron dose level prior to the measurement to get good SNR aids to achieve the best possible precision depending on thickness of the sample of interest. However, Xianlin Qu and Qingsong Deng [72] have reported dominant knock-on beam damage in Si for higher electron dose rates around $1.8 - 2.6\ \times 10^{20} e^{-} cm^{-2} s^{-1}$and this can result in detrimental effects for strain measurement. For a typical experimental beam current of 35 pA and a total scanned area of approximately 450 x 100 nm^2 the estimated dose rate is 4.86 x 10^{17} $e^{-} cm^{-2} s^{-1}$and is well below the reported limits for beam damage.

2.2. Raman strain measurement technique

Raman spectroscopy is a non-destructive tool to characterize a variety of material parameters like for instance mechanical stress in crystalline materials. It is used primarily to study the vibrational energy levels in a crystal using laser light as an excitation source. Since the technique is non-invasive, i.e. it does not require special thin samples as opposed to the TEM techniques mentioned earlier and is therefore not prone to sample preparation induced strain relaxation. The excitation of Raman active phonons is sensitive to the incoming and outgoing light polarizations. The Raman scattering efficiency I is given by:

$$I = C \sum_{j} \left| e_{out}^{T} R_j e_{in} \right|^2 \tag{20}$$

where, C is a constant and R_j is the Raman tensor corresponding to the jth phonon, e_{out} and e_{in} are the outgoing and incoming polarisation vectors. The superscript T corresponds to the transposed vector.

In Si and Ge crystals, there is one longitudinal optical phonon (LO) and two transverse optical phonons (TO) resulting in a total of three active Raman peaks at k = 0 (central point of the Brillouin zone) [47]. The three phonons are degenerate in the bulk crystal due to the crystal symmetry while strain alters the symmetry and lifts this degeneracy [73]. The key to strain measurement using Raman is the identification of the relative shift in the peak positions of the phonons with respect to the bulk unstrained crystal. The relative phonon peak shifts are sensitive to the stress developed in the material [35] and the stress-strain relation in the elastic regime (eq. 6) is used to further calculate strain. Thus, Raman strain measurement is an indirect technique to measure strain and the relation between the peak shifts and the stresses are explained in detail in chapter 6.

For the confocal Raman microscope operating in the backscattering configuration (Appendix A1.2), the incoming light polarization is restricted to the transverse direction and hence one can excite only the LO phonon out of the three Raman active phonons (again a more detailed discussion on the incoming/outgoing polarization conditions for excitation of specific phonons is provided in chapter 6). Therefore, this approach gives information of the overall stress in a material while lacking the ability to measure individual stress tensors. The introduction of high numerical aperture (NA) objective lenses and oil immersion lenses provides higher convergence angles and increases the longitudinal component of the electric field near the focal plane and thus enables the excitation of the TO phonons that are traditionally forbidden in the backscattering configuration [74].

Considering a He-Ne laser light source operating at 633 nm, the diffraction-limited spatial resolution (Abbe limit $\lambda/_{2.8} \approx 226\, nm$, numerical aperture(NA) = 1.4) of the laser source is lower than the nanoscale device dimension which needs to be probed, but the technique remains applicable when employing the concept of nano-focussing [75,76]. In this concept, a parallel array of nanodevices is probed which forms a waveguide-like structure allowing specific modes for transmission depending on the polarization conditions. This leads to an enhancement of the local electric field and hence amplifying the Raman signal from the nanodevices[77]. The signal collected from such an array of nanodevices is the sum over multiple devices and the calculated stress is averaged over the probed location. Hence, it does not provide details on the nanoscale spatial strain distribution inside one particular nanodevice like in the case of TEM. However, averaging over multiple devices can be an asset as it improves the statistical significance of the results as long as the interdevice variation is kept small.

Motivation

From investigations of the state of the art techniques, we can notice that TEM techniques are applicable during the development phase but are destructive (due to FIB sample preparation) and too slow for the production phase, whereas Raman is fast, non-invasive and will target in-line monitoring. Hence, in this thesis we compare the strain measurements from the TEM nanoscale strain measurements with the Raman techniques on semiconductor finFETs and analyse the differences due to strain relaxation from TEM sample preparation.

Given the advantages TEM diffraction techniques (NBED, N-PED, CBED and Bessel diffraction) and DFEH have in comparison to other imaging techniques (HR(S)TEM) in terms of parameters like precision and field of view, it is tempting to choose the former for strain analysis. However, the diffraction techniques are relatively expensive in terms of data acquisiton and processing time, higher data storage and require specialised diffraction cameras like CCD (charge coupled device). Imaging techniques like HRSTEM and moiré on the other hand are very fast in terms of acquisition and strain analysis and efficient in data volume. Another advantage of the imaging techniques is the provision for straightforward interpretation of defects in the sample in comparison to diffraction based techniques where analysing the defects through diffraction patterns requires detailed analysis and is often complicated and time consuming [39]. The imaging techniques also provide extended spatial resolution up to a single unit cell (precision decreases with increase in spatial resolution) that is needed for the next generation of semiconductor devices (for example, 3 nm technology node). However, there are limitations currently attached to imaging techniques like HRSTEM and moiré, i.e. STEM moiré is limited in spatial resolution and HRSTEM is limited by the field of view and precision. Hence, novel approaches are necessary in order to improve some of the aforementioned drawbacks.

The state of the art TEM techniques are measuring strain on 2D projection images or projection of diffraction patterns along a specific crystallographic zone axis. Hence, one requires two orthogonally oriented cross-sectioned TEM samples are required for measuring strain along the three Cartesian coordinates which requires extra effort and analysis time. Also relaxation between the two samples will not be the same depending on the thicknesses of the samples, since TEM samples can be prone to sample preparation induced relaxation. In addition, the techniques lack the ability to measure strain through the projection direction. To overcome these limitations and to enable a true 3D strain measurement, we attempt as a proof of concept, high-resolution tomography based 3D strain analysis on a Si-Ge test structure.

Finally, Raman strain measurement relies on sensitive deconvolution of the TO (tranverse optic) and LO (longitudinal optic) phonon peaks in the Raman spectrum (details in section 6.2). The TO and LO peaks overlap each other strongly within the spectral resolution of the spectrometer and the deconvolution is rather challenging. Hence, we explore new polarisation geometries like radially polarised incoming light that enhances the TO contribution in the spectrum [74,78] which can ease the deconvolution problem and facilitate improved precision for Raman stress–strain measurements.

Outline of the thesis

The research problems mentioned in the motivation section is tackled individually in different chapters. In chapter 3, we will introduce a novel quadrature demodulation technique for improved spatial resolution in STEM moiré.

In chapter 4, we will introduce a new scan strategy called "Block-scanning" that provides a wider field of view in comparison to HRSTEM with reduced scan artefacts. In chapter 5, we present 3D strain tomography on a Si-Ge test structure and the proof of concept for 3D strain analysis in Si-Ge materials. In chapter 6, we will discuss in detail the Raman spectroscopy-based strain measurement and newer setups for improved precision in strain measurement. We also compare the results with TEM-based techniques. Finally, we provide general conclusions and an outlook.

Chapter 3: Moiré demodulation technique

This chapter contains large excerpts from the published paper:

V. Prabhakara, D. Jannis, A. Béché, H. Bender, J. Verbeeck, Strain measurement in semiconductor FinFET devices using a novel moiré demodulation technique, Semicond. Sci. Technol. 35 (2020) 34002. https://doi.org/10.1088/1361-6641/ab5da2.

First author contributions include experimental design and experimentation, strain analysis, idea formulation and writing the manuscript, D.J was responsible for setting up the scan engine for software control along with python inferface, A.B. has contributed with the initial experimentation for evaluation of the moiré imaging, H.B has contributed by reviewing the manuscript and J.V has contributions for idea formulation and manuscript revision.

3.1. Introduction

The Moiré imaging technique provides a fast and dose efficient approach to extract sensitive strain information from a crystal lattice. Moiré fringes can be used to extract small variations in an underlying lattice by comparing with another reference lattice and are used throughout a wide variety of applications in physics and engineering. The scanning raster serves as the reference and has been recently demonstrated in Scanning Transmission Electron Microscopy imaging to provide local strain measurement in crystals. In the previous chapter, we have explained the formation of moiré fringes using the sampling theorem and it has been seen that the moiré fringe is formed due to undersampling, i.e. the sampling frequency is lower than twice the highest frequency in the sampled data and thus deliberately violating the 'Nyquist criterion'. A careful choice of the scanning grid (with specific direction and spacing) that serves as the reference would result in moiré patterns in the STEM imaging and using image processing techniques like GPA, enables to extract reliable strain information [79]. The spatial resolution using the moiré imaging technique is rather limited because in order to obtain the actual strain value, a region containing a full period of the fringe is required, which results in a compromise between strain sensitivity and spatial resolution. In this chapter, a proposition to an advanced setup is made which makes use of an optimised scanning pattern and a novel phase stepping demodulation scheme. The setup provides a much improved spatial resolution (1 – 3 nm) over conventional moiré imaging in STEM while conserving the conventional advantages of being fast and having high sensitivity along with wider field of view (~ 200 - 250 nm).

3.2. STEM moiré theory

STEM moiré correspond to a phenomenon caused by interference between a chosen sampling grid which is the periodic arrangement of the points sequentially visited by the STEM probe and the crystal lattice. The STEM probe here is assumed to be infinitely small, which allows us to express the scanning grid as a 2D Dirac comb. The illuminated crystal lattice is then sampled at these points. A continuous image of the sample, independent of the specific imaging mode in STEM, can be expressed as an intensity variation of a detector signal (e.g. a High Angle Annular Dark Field detector) depending on the probe position $I(y, z)$.

Sampling in STEM is analogous to multiplication of this image function by a 2D Dirac delta comb $S(y, z)$

$$S(y,z) = \sum_{m=-\infty}^{m=\infty} \sum_{n=-\infty}^{n=\infty} \delta(y - mp_y)\delta(z - np_z) \tag{21}$$

With p_y and p_z the spatial sampling step in y and z directions. We get a resulting discrete image:

$$I(y_m, z_n) = I(mp_y, np_z) \tag{22}$$

In frequency space, this becomes a convolution of the Fourier transform (FT) of the image $I(u, v)$ with the FT of the 2D sampling grid which transforms to:

$$S(u,v) = \sum_{m=-\infty}^{m=\infty} \sum_{n=-\infty}^{n=\infty} \delta(u - mf_{py})\delta(v - nf_{pz}), \tag{23}$$

with, $f_{py} = \frac{1}{p_y}, f_{pz} = \frac{1}{p_z}$.

The discrete frequency spectrum of the sampled image is then written as

$$I_c(u,v) = I(u,v) * \sum_{m=-\infty}^{m=+\infty} \sum_{n=-\infty}^{n=+\infty} \delta(u - mf_{py})\delta(v - nf_{pz}) \tag{24}$$

Note that we have taken the finite size of the sampling grid (the field of view) as a cut-off into the image spectrum rather than in the Fourier transform of the grid to keep the delta functions.

$$I_c(u,v) = \sum_{m=-\infty}^{m=+\infty} \sum_{n=-\infty}^{n=+\infty} I(u - mf_{py}, v - nf_{pz}) \tag{25}$$

This results in an infinite series of replicas with the central one occupying the frequency range $\left[\frac{-1}{2p_y}, \frac{1}{2p_y}\right] \cup \left[\frac{-1}{2p_z}, \frac{1}{2p_z}\right]$. If the maximum frequency in the image $u\_\max < {}^1\!/_2\, p_y$ and $v\_\max < {}^1\!/_2\, p_z$, the sampling satisfies the Nyquist criterion and each replica is separated from all other replicas (Figure 11b). In the case of under-sampling, aliasing occurs, leading to the formation of moiré fringes by the replication of frequencies from outside the central portion into this region (Figure 11c).

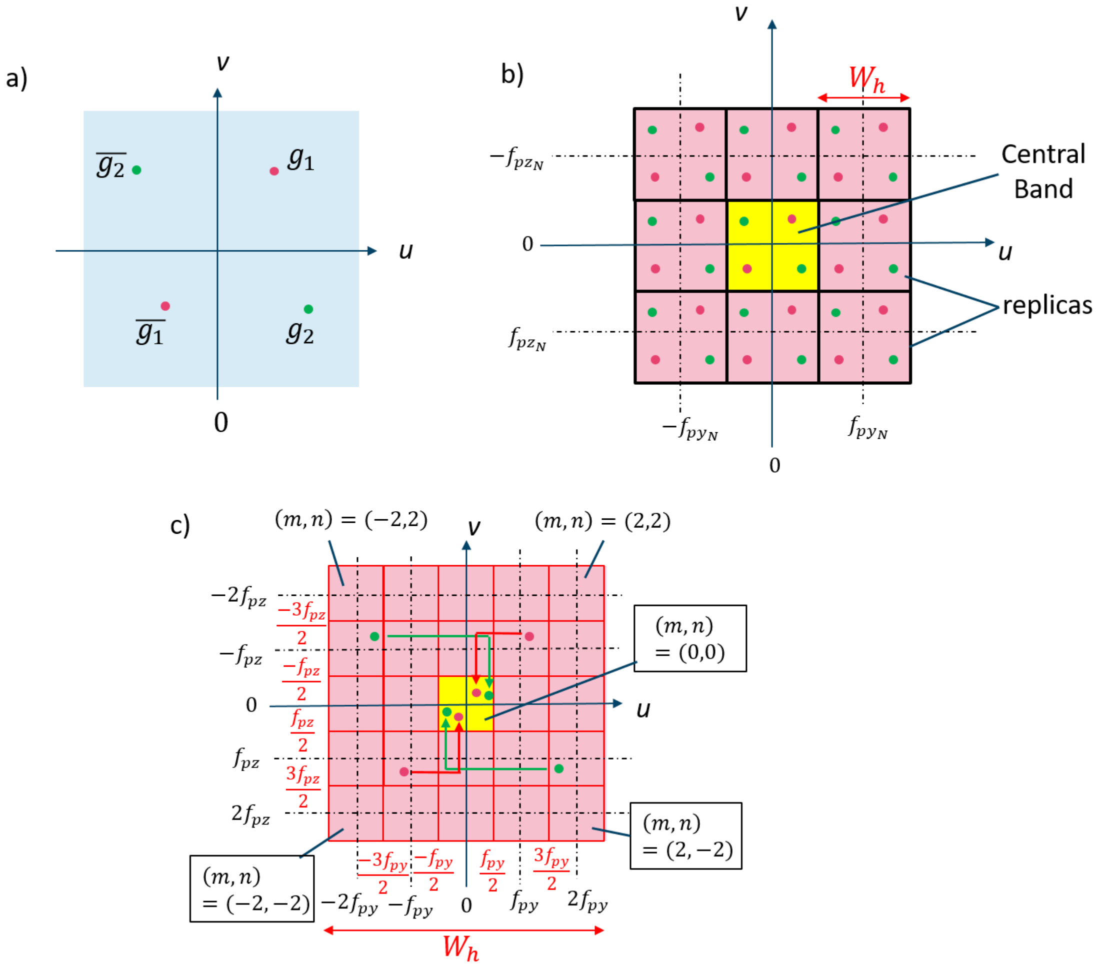

Figure 11 a) Frequency represenation of a periodic 2D signal.b) Sampling with Nyquist criterion results in an infinite amount of replicas indicated by red boxes with dimensions determined by the sampling frequency. c) moiré effect with sampling frequency lower than the highest frequency. The replication due to the finite sampling results now in a mixing up of the position of the frequency components which is best noted in the central replica marked in yellow. This mixing up is the essence of the moiré effect where frequencies appear different from what they really were without sampling. The frequencies get aliased and a high resolution frequency spectrum is now divided into smaller moiré windows with index (m,n) due to a lower sampling frequency in the moiré compared to a high resolution image. The arrow indicates the translation of frequencies into the new smaller central band.

As an example, we can assume an image made of two sinusoids (g_1, g_2) as shown in Figure 11a. A sampling frequency f_{py} and f_{pz} is chosen such that the Nyquist criterion is not satisfied, which results in the moiré effect (Figure 11c). The yellow window represents the central replica with each red box an identical replication. The index of each window is represented by (m,n) and the frequencies that are outside the yellow window are translated into the yellow window by shifting the window over $(mf_{py}\ ,nf_{pz})$. For example, the frequency g_1 is shifted one window down in v and one window left in u and so on [80]. This leads to a new apparent spatial frequency (the moiré frequency) within the central frequency band:

$$g'_y = g_y - mf_{py} \tag{26}$$

$$g'_z = g_z - nf_{pz} \tag{27}$$

Where, g_y and g_z are the frequency components in y and z directions. For a projection image of Si or Ge along the [110] zone axis, the y axis is considered along the $[1\bar{1}0]$ direction and the z axis along the [001] direction. The lattice spacing for Si is different in these two directions where $a_{1\bar{1}0} = 0.384\ nm$ and $a_{001} = 0.543\ nm$ (Figure 12a). This means, for any fundamental frequency of the crystal in y and z directions, g_y and g_z, we have $g_y > g_z \in (u, v)$. In conventional STEM, a square scanning grid is implied that means $f_{py} = f_{pz}$. In general, this results in the creation of 1D moiré fringes as m and n are not necessarily the same.

Figure 12d shows an experimental image obtained with a square scanning grid, resulting in only one fringe direction to be visible while the other is too high in frequency. These 1D moiré fringes are easily observed for a probe aberration corrected instrument (the probe has to be smaller than the lattice spacing) and readily reveal strain as a slight change of the moiré fringes in different locations of the image.

The resulting distortion of the apparent symmetry by the formation of 1D moiré can be circumvented and a more interpretable situation is created if the symmetry of the scanning grid matches the symmetry of the lattice by adjusting the scan pattern to obey:

$$\frac{g_y}{f_{py}} = \frac{g_z}{f_{pz}} = U, \tag{28}$$

with U the under-sampling factor > 0.5. This can be done by adjusting the strength of the signals driving the scan coils. In this case, all the frequencies transform as:

$$g'_y = g_y - mf_{pz}\frac{g_y}{g_z} = g_y\left(1 - m\frac{f_{pz}}{g_z}\right) = g_y\left(1 - \frac{m}{U}\right) \tag{29}$$

$$g'_z = g_z - nf_{py}\frac{g_z}{g_y} = g_z\left(1 - n\frac{f_{py}}{g_y}\right) = g_z\left(1 - \frac{n}{U}\right) \tag{30}$$

If m=n, this transform is an angle preserving scaling factor and the moiré fringes will have the same symmetry as the lattice. An experimental example is shown in Figure 13a.

When strain occurs in the lattice, frequencies will shift by Δg and a relative shift of the diffracted spots can be obtained in the diffraction pattern (as in NBED). The strain in a particular direction is expressed as:

$$\varepsilon = \frac{|\Delta\vec{g}|}{|\vec{g}|} \tag{31}$$

When under-sampling occurs, an apparent strain will appear in the moiré fringe as

$$\varepsilon' = \frac{|\Delta\vec{g}|}{|\vec{g'}|} = \frac{|\Delta\vec{g}|}{\sqrt{\left(g_x - mf_{px}\right)^2 + \left(g_y - nf_{py}\right)^2}} = \alpha\varepsilon \tag{32}$$

The strain gets magnified by a boost factor α which makes it much more apparent as can be seen both in Figure 13a and Figure 14. This boosting is shape preserving (ε' stays parallel to ε) only in the case where the scan grid matches the symmetry of the crystal and a situation is chosen where m=n.

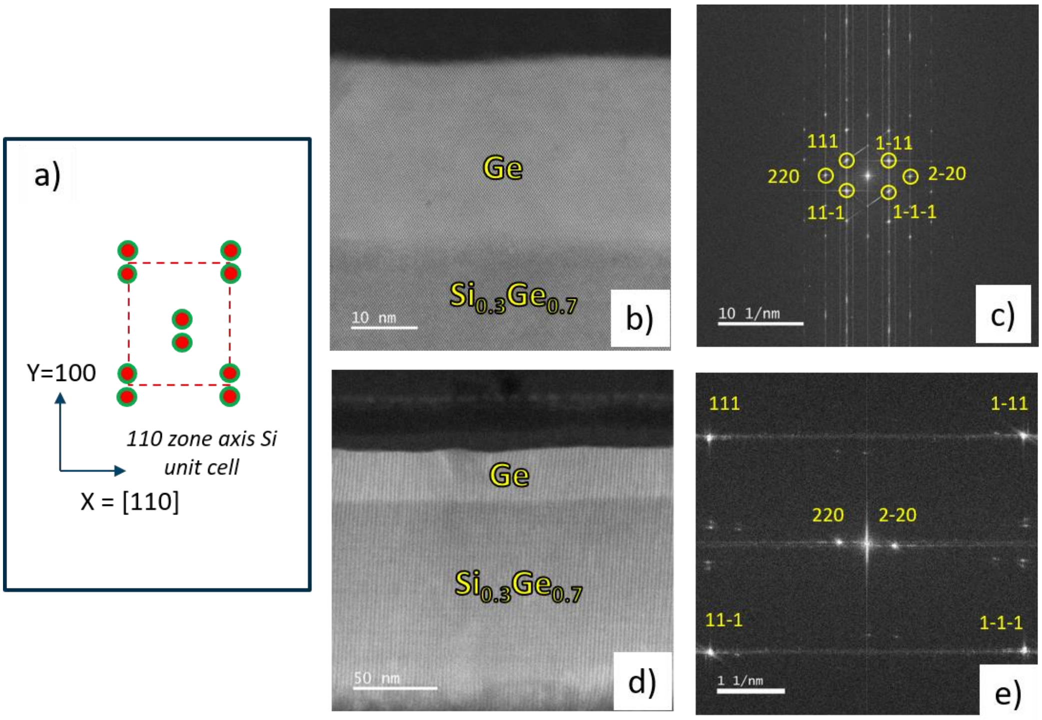

Figure 12 a) Diagram of the unit cell of Si and Ge in [110] zone axis b) HRSTEM image of the SiGe and Ge interface on the 16 nm finFET and its corresponding Fourier transform or diffractogram c). d) 1D moiré *created on the Si and Ge material by undersampling at lower magnification and its corresponding diffractogram e). The undersampling results in clear* moiré *fringes in d) caused by only the {002} spots being replicated to rather low frequencies and a mixing up of the frequency components as in e). The moiré fringes are sentive to strain as seen by the slight wavyness and tilting of these fringes as a function of the location on the sample.*

The lattice spacing and the atomic positions in the real space image have a direct relation with the sinusoidal components in the FT. This is not true for a diffraction pattern, which, has an inverse relation. Since we are using GPA for strain analysis on real space images, we can directly relate the frequency components with the atomic positions as normally done in GPA.

To understand the origins of the boosting factor and to obtain a mathematical relation, let us consider the reference frequency or unstrained frequency as g_{ref} and the strained frequency as $g_s = g_{ref}(1+\delta)$, δ is the strain. After sampling with the STEM probe with frequency f_s satisfying the Nyquist criterion, the digital frequency ($Spatial\ frequency\ of\ crystal/Sampling\ frequency$) of the reference and strained area becomes $\frac{g_{ref}}{f_s}$ and $\frac{g_s}{f_s}$. The strain δ calculated for the high resolution images which should always satisfy the Nyquist criterion is

$$Strain_H = \frac{{g_s}/{f_s} - {g_{ref}}/{f_s}}{{g_{ref}}/{f_s}} = \delta \tag{33}$$

So the obtained strain value is independent of the sampling frequency as long as the Nyquist criterion is satisfied.

Now, consider the situation of moiré fringes created using a different sampling frequency f_m that do not satisfy the Nyquist criterion, so the digital frequencies ($Spatial\ frequency\ of\ the\ crystal/Sampling\ frequency$) obtained with this type of sampling now is

$$g_{ref,m} = \frac{g_{ref}}{f_m} - n \tag{34}$$

$$g_{s,m} = \frac{g_s}{f_m} - n = \frac{g_{ref}(1+\delta)}{f_m} - n \tag{35}$$

where n is the moiré window from which the frequency is being translated. Now, the strain obtained by moiré imaging is

$$Strain_M = \frac{\frac{g_s}{f_m} - n - \left(\frac{g_{ref}}{f_m} - n\right)}{\frac{g_{ref}}{f_m} - n} = \frac{\delta}{1 - \frac{nf_m}{g_{ref}}} \tag{36}$$

$$Strain_M = \alpha\ Strain_H$$

Where $\alpha = \frac{1}{1-\frac{nf_m}{g_{ref}}}$ is the amplification factor.

So, the strain values for the moiré fringes do depend on the sampling frequency and the moiré window from which the frequency is translated, and hence it becomes important to calibrate these parameters or have a preset in order to obtain the required amplification factors for the sensitive extraction of strain information.The amplification factor is plotted as a function of the under-sampling factor U showing how apparent-strain boosting is especially strong for low frequency moiré fringes (Figure 14). This also implies a hard trade-off between strain sensitivity and spatial resolution.

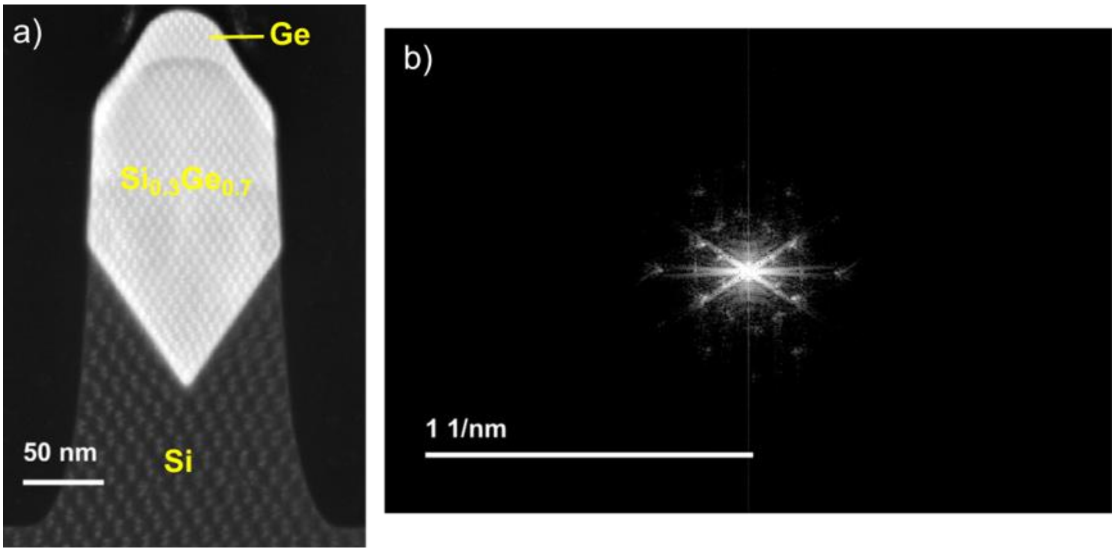

Figure 13 2D moiré fringes on a Si-Ge 100nm FinFET in [110] zone axis and its corresponding b) diffractogram. Note the effect of local strain becoming visible as a distortion of the moiré *fringe pattern in different locations of the sample.*

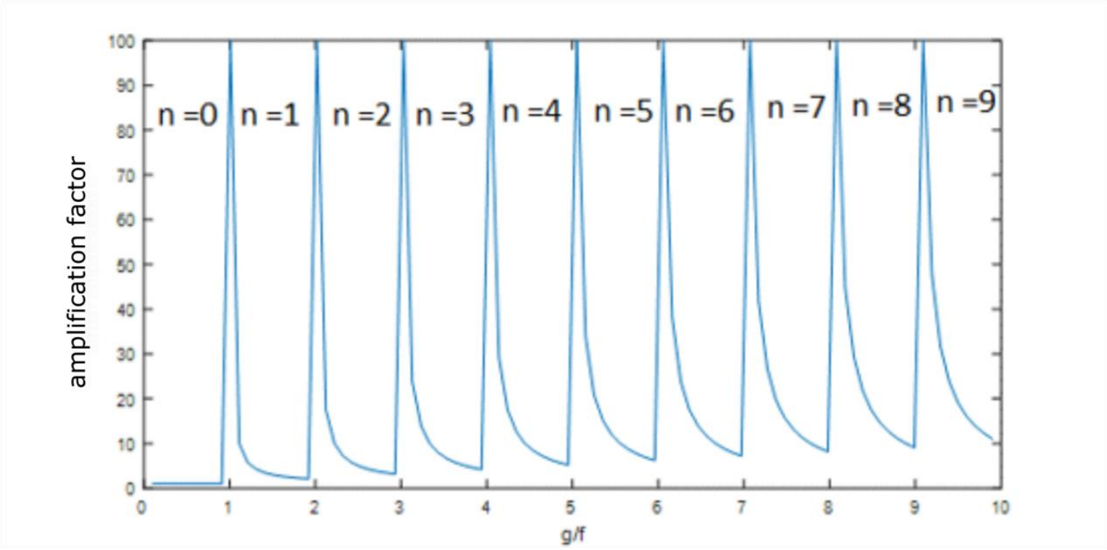

Figure 14 Amplification factor α as a function of under-sampling. Note how strain magnification depends in a sensitive and nonlinear way on the choice of $U = {}^{g}/_{f}$ *and n is the moiré window (eq. 36). The value of n equal to zero is for an oversampled high resolution image and it does not have any amplification (α=1). The amplification factor is extremely high when n = U.*

In order to determine the frequency of the moiré fringe (related to the strain), one needs at least an area of the order of a period of the fringe. Another limitation comes from the fact that strain should not shift frequencies outside the central frequency replica. Otherwise m and n may differ for different areas of the sample leading to a much more complicated analysis. This limits the tolerable strain variation in a single image as the amplification factor goes up.

Strain analysis of moiré STEM images can be typically performed using GPA. As described in the introduction section, GPA requires a mask in the frequency space to isolate frequencies/reflections and later extract strain from the geometric phases. This selection mask determines also the spatial resolution that can be obtained and determines the signal to noise ratio in the resulting strain map. The larger the radius of the mask, the higher is the spatial resolution and the more noise enters the estimated strain map. The mask radius is chosen to prevent selecting more than one diffraction spot at a time and is typically chosen smaller than half of the selected reference frequency. This reference lattice vector is used to demodulate the measured signal which then reveals the strain with respect to this reference.

Moiré images inherently boost the strain information as given by eq.36 and it is necessary to rescale the apparent strain to the actual strain values. As the strain magnification is significantly higher for low frequency moiré fringes, it is tempting to choose the undersampling as demonstrated in Figure 15a where strain is readily apparent from the moiré image due to the boosting effect.

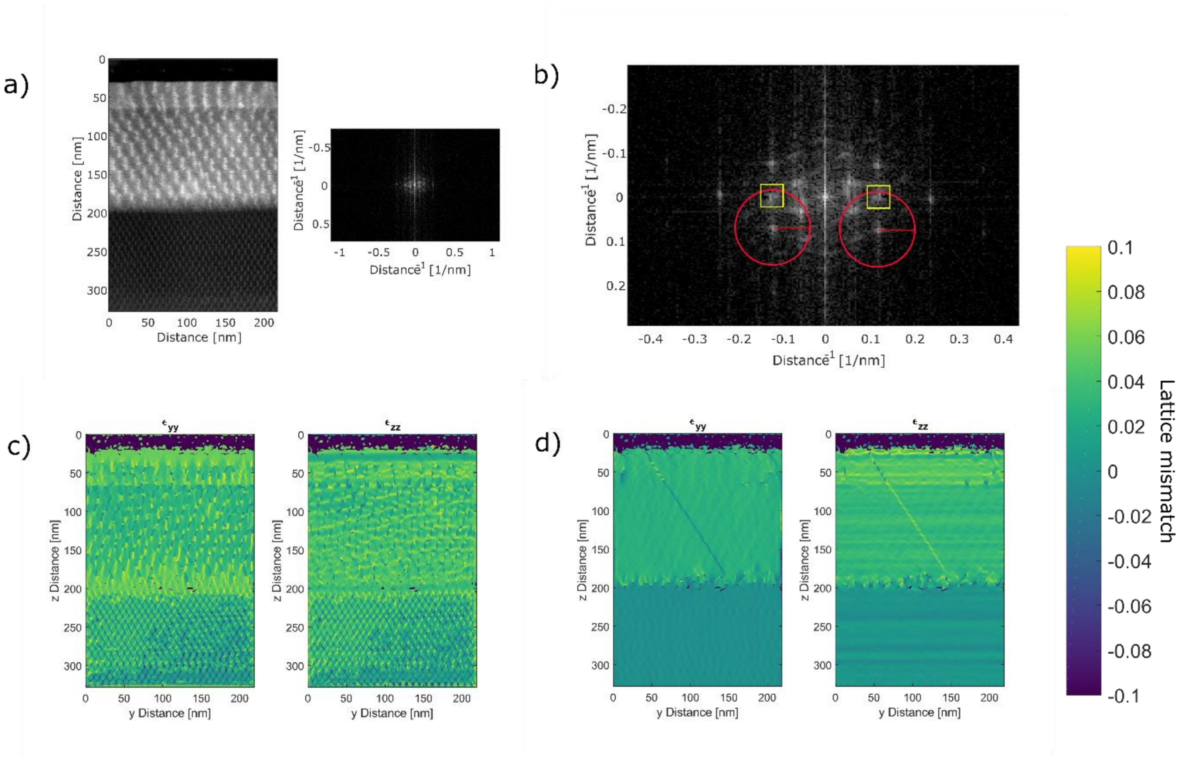

Figure 15 2D moiré on the 16 nm Fin long section and its corresponding FFT b) GPA Masks used to isolate the regions in the FT. The yellow squares are the undesired interfering frequencies c) Normal strain ε_{yy} and ε_{zz} in the y and z directions obtained by GPA d) Comparing normal strain ε_{yy} and ε_{zz} in the y and z directions obtained by GPA on moiré with quadtrature demodulation. A reliable strain map is obtained with the application of Quadrature demodulation

The low frequency moiré fringes have multiple spatial frequencies possibly having different m and n values that tend to cluster near the centre and can be very close to each other. This results in unwanted overlaps inside the GPA mask and the strain maps become unreliable with precision ~2.5x 10^{-2} (Figure 15 c), especially as each of these frequencies should be converted from apparent strain to actual strain with different scaling factors (Figure 15 b). In order to overcome this difficulty and to increase the practical usefulness of moiré strain mapping, an alternative method was developed that allows significant suppression of unwanted reflections in the FT while enhancing the reflection of interest. This approach which acts to select one particular reflection while suppressing the rest, provides the option to greatly increase the size of the GPA mask and consequently increase the spatial resolution. Further, the performance of the technique is discussed in more detail in section 3.5.

3.3. Extending the spatial resolution with quadrature demodulation

The idea of extracting a particular reflection in the FT of the moiré image would enable one to use a much larger mask size before demodulating the signal back to an image of the strain. This would result in higher spatial resolution and the suppression of artefacts. This is achieved by moiré phase stepping interferometry and Quadrature demodulation. The principle of moiré phase stepping interferometry is to phase shift the moiré fringes in different specific directions in repeated experiments.

If we shift the experimental scanning grid over Δy and Δz in y and z directions,

$$S(y,z) \rightarrow S(y-\Delta y, z-\Delta z) \tag{37}$$

and applying the Fourier shift theorem, we get the Fourier transform of the sampling grid

$$S(u,v) \rightarrow S(u,v)e^{i2\pi(u\Delta y+\ v\Delta z\ )} \tag{38}$$

This results in phase shifting of the different components in the spectrum and eq.25 becomes

$$I(u,v) = \sum_{m=-\infty}^{m=\infty} \sum_{n=-\infty}^{n=\infty} I\left(u - mf_{my}, v - nf_{mz}\right)e^{i2\pi(u\Delta y+v\Delta z)} \tag{39}$$

This equation shows that it is sufficient to shift the sampling grid by a reference lattice fringe spacing $\Delta y = \frac{1}{g_y}$ and $\Delta z = \frac{1}{g_z}$ to cause a 2π phase shift of these moiré fringes in the under-sampled image.

Now that we have the capability to phase shift the frequency components in the recorded moiré images by spatially shifting the sampling grid, we can apply an extended version of quadrature demodulation i.e., application on the 2D image datasets. Quadrature demodulation is commonly used in telecommunication (e.g. FM (frequency modulation) radio) [80] and allows to extract a given sideband of a modulated signal. In our case the 'carrier frequency' is a reference spatial frequency and the 'signal' is the strain or deviation with respect to this signal. The schematic in Figure 16, gives an example of a particular reflection extraction from phase shifted sinusoidal signal, which is essentially the essence of Quadrature demodulation.

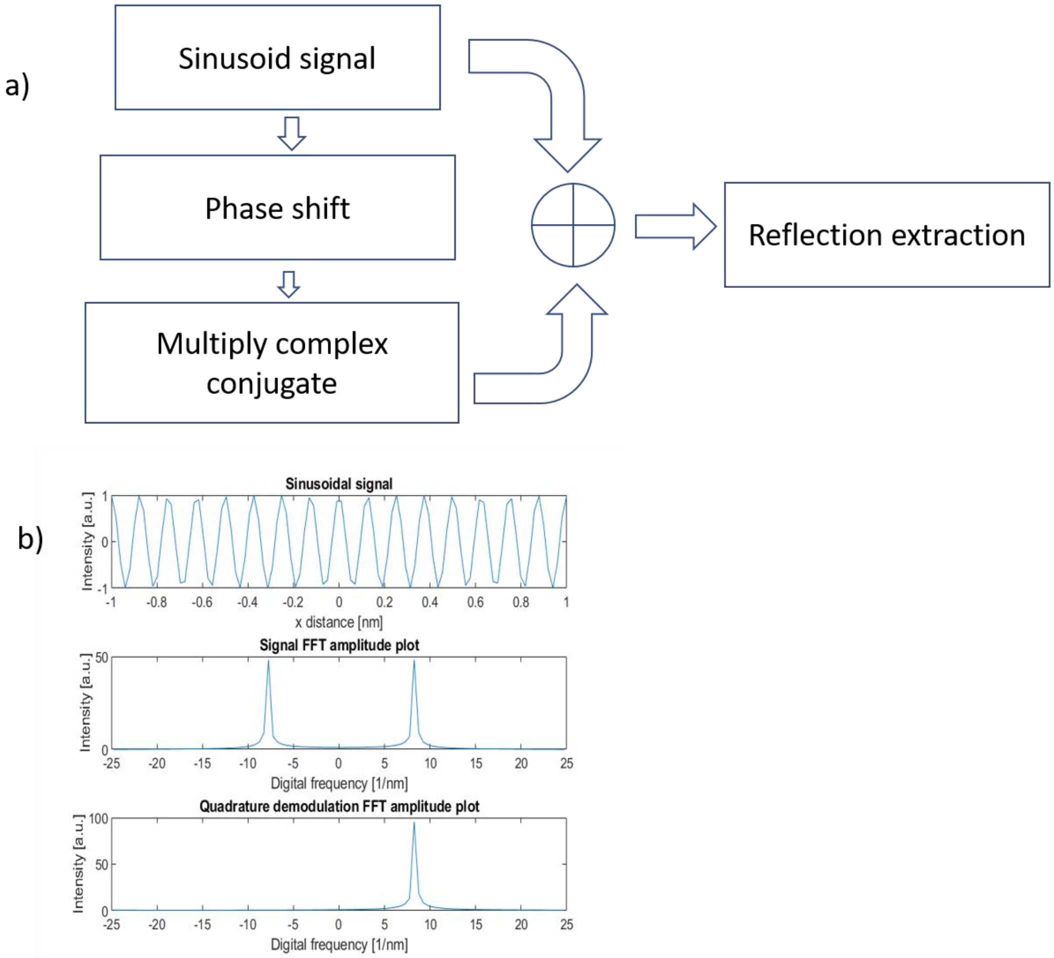

Figure 16 a) Schematic flow for the quadrature demodulation b) Illustration of quadrature demodulation on a sinusoidal signal resulting in the extraction of the positive reflection in the FT

Consider a sinusoidal signal $x_{in} = Acos(\omega t + \emptyset)$, where A is the amplitude, ω is the angular frequency, t is the time and $\emptyset$ is the phase. x_{in} can be further decomposed into

$$x_{in} = \frac{A}{2}\left(e^{i(\omega t + \emptyset)} + e^{-i(\omega t + \emptyset)}\right) \tag{40}$$

This can be further rewritten as

$$x_{in} = A'\left(e^{i\emptyset} + e^{-i\emptyset}\right) \tag{41}$$

Where, $A' = \frac{A}{2}e^{i\omega t}$. Now x_{in} is phase shifted by $\frac{\pi}{2}$ resulting in x_c.

$$x_c = A'\left(e^{i\left(\emptyset+\frac{\pi}{2}\right)} + e^{-i\left(\emptyset+\frac{\pi}{2}\right)}\right) \tag{42}$$

Now, x_c is multiplied by $e^{-i\frac{\pi}{2}}$ which is a complex conjugate of the phase shift resulting in x_q.

$$x_q = A'\left(e^{i\emptyset} - e^{-i\emptyset}\right) \tag{43}$$

Finally, x_q is added to the original signal x_{in}, to extract the positive frequency/ reflection of the sinusoidal signal,

$$x_{out} = 2A'e^{i\emptyset} \tag{44}$$

An illustration of the application of quadrature demodulation on a simple sinusoidal signal is shown in Figure 16 b, resulting in the extraction of the positive refection in the FT and strongly suppressing the negative side of frequency/reflection. Since, we now have the general premise for the frequency extraction, we apply our understanding to the frequency extraction for the case of 2D moiré images to alleviate the problem of unwanted overlaps inside the GPA mask as illustrated in Figure 15b.

For this purpose, we apply a 4x4 array of shifts of the scanning pattern, resulting in 16 independent and phase shifted moiré images. The applied shift can be represented as a 4x4 matrix S targeted to bring out the strain along 2 non-collinear reference reflections $\vec{g}_1$ and $\vec{g}_2$.

$$\vec{S} = \frac{1}{4}\begin{bmatrix} (0,0) & \left(a_{y_1}, a_{z_1}\right) & \left(2a_{y_1}, 2a_{z_1}\right) & \left(3a_{y_1}, 3a_{z_1}\right) \\ \left(a_{y_2}, a_{z_2}\right) & \left(a_{y_1} + a_{y_2}, a_{z_1} + a_{z_2}\right) & \left(2a_{y_1} + a_{y_2}, 2a_{z_1} + a_{z_2}\right) & \left(3a_{y_1} + a_{y_2}, 3a_{z_1} + a_{z_2}\right) \\ \left(2a_{y_2}, 2a_{z_2}\right) & \left(a_{y_1} + 2a_{y_2}, a_{z_1} + 2a_{z_2}\right) & \left(2a_{y_1} + 2a_{y_2}, 2a_{z_1} + 2a_{z_2}\right) & \left(3a_{y_1} + 2a_{y_2}, 3a_{z_1} + 2a_{z_2}\right) \\ \left(3a_{y_2}, 3a_{z_2}\right) & \left(a_{y_1} + 3a_{y_2}, a_{z_1} + 3a_{z_2}\right) & \left(2a_{y_1} + 3a_{y_2}, 2a_{z_1} + 3a_{z_2}\right) & \left(3a_{y_1} + 3a_{y_2}, 3a_{z_1} + 3a_{z_2}\right) \end{bmatrix} \tag{45}$$

Where, $\frac{1}{\vec{g}_1} = \vec{a}_1 = \left(a_{y_1}, a_{z_1}\right)$ and $\frac{1}{\vec{g}_2} = \vec{a}_2 = \left(a_{y_2}, a_{z_2}\right)$; y, z being the horizontal and vertical coordinates of the Cartesian coordinate system.

Each index of the matrix can be written as:

$$\vec{S}_{k,l} = \frac{k\vec{a}_1}{4} + \frac{l\vec{a}_2}{4} \tag{46}$$

The shifts result in a complex factor that is applied to a specific frequency component in the frequency domain:

$$f_{kl}(\vec{g}) = \exp\,(i2\pi\vec{g}\cdot\vec{S}_{kl}) \tag{47}$$

This means that we can single out any specific spatial frequency of interest by multiplying each sub-diffractogram $I(u,v)_{kl}$ with the complex conjugate of the above matrix and then summing up over all k,l indices. This results in constructive interference of a selected frequency g while destructive interference occurs approximately for all other frequencies

$$I_{demod}(u,v)_{g_y,g_z} = \sum\nolimits_{kl} I(u,v)_{kl} f_{kl}^{*}\left(g_y,g_z\right)) * \delta\left(u-g_y, v-g_z\right) \tag{48}$$

with the delta function doing the actual demodulation. Converting this back to real space leads to the demodulated strain component with respect to the selected reference frequency.

$$I_{demod}(y,z)_{g_y,g_z} = \mathcal{F}^{-1}\left(I_{demod}(u,v)_{g_y,g_z}\right) \tag{49}$$

The selectivity improves with a $n \times n$ shifting matrix with increase in n, but this comes at the expense of an increase in the measurement time as n^2. A minimal choice would be n=2, but we show in the experimental section that n=4 provides a more realistic compromise. In fact, the suppression rate for any other frequency $\vec{g}$ in the discrete Fourier space of the image can be calculated as.

$$SR(\vec{g},\vec{g}_{desired}) = \frac{1}{16}\sum_{k,l} f_{k,l}(\vec{g}) {f^{*}}_{k,l}(\vec{g}_{desired}) < 1 \tag{50}$$

Ideally this suppression preserves frequencies close to the desired frequency as these carry the strain information but achieves a high suppression for frequencies that are further away.

3.4. Experiment

In order to implement the above mentioned idea in a transmission electron microscope, it is necessary to obtain software control over the probe scan engine. Making use of a custom built scan engine [81,82] , we are able to freely program the scanning pattern in an aberration corrected Thermofischer Titan^3 STEM instrument operating at 300 kV. We tune the scanning step-size to 17/16th of the lattice spacing of the silicon substrate in the y and z directions, i.e., $p_{yh} = \frac{17}{16} d(Si)_{1\bar{1}0}$ and $p_{zh} = \frac{17}{16} d(Si)_{001}$. This results in a distorted under-sampled (U=17/16=1.0625) moiré image that images the rectangular [110] projection of the silicon and germanium lattice as a square. This implies that n=m=1 and brings us into the central band with an amplification factor of $\propto = 17$ (eq.36). However, in a realistic scenario, there can be small deviations in the experimental sampling frequency while tuning the step-size and thus propagating the error into the amplification factor calculation. Hence, determining the experimental sampling frequency is crucial in order to determine the correct amplification-factor. The procedure is straightforward and illustrated in Appendix 6.

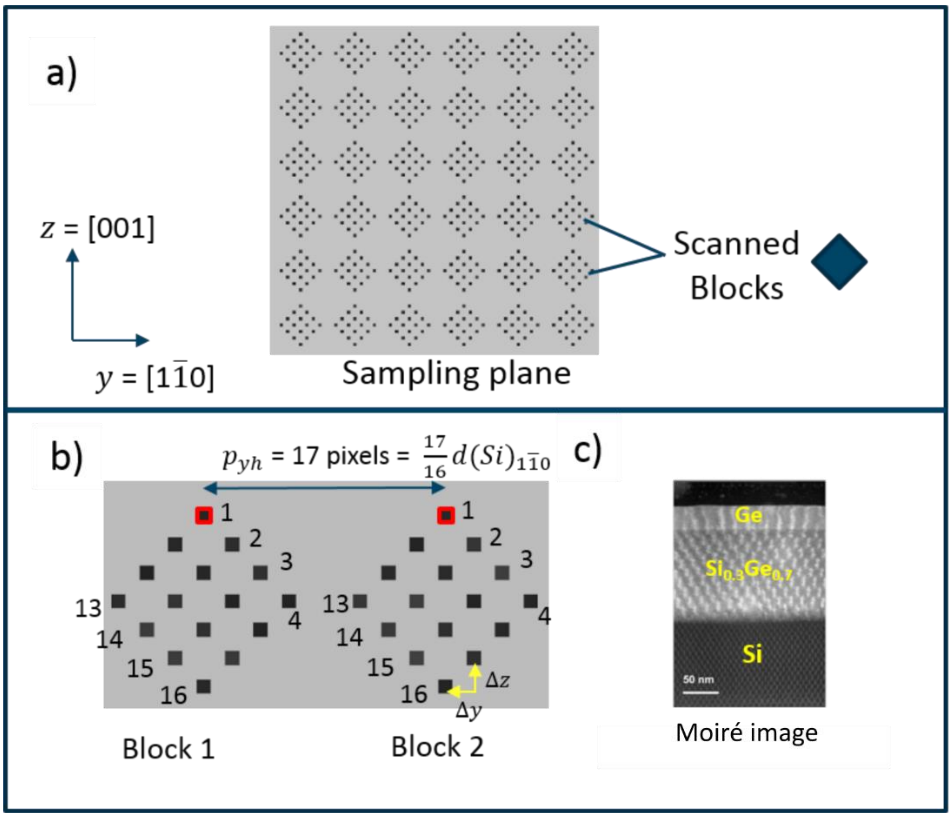

Figure 17 a) Overview of the scanning pattern where the black squares represent probe positions that are visited sequentially in blocks of 4x4 pixels. The order of the probe visiting positions inside each block is shown in Figure 23b. c) moiré image obtained by using only pixel 1 from each block, marked in red in b. The pixel step size is $d_{1\bar{1}0}/16$ in y direction and $d_{001}/16$ in z-direction. This makes the pixel size for the moiré image $^{17}/_{16}$ th of the lattice spacing of Silicon($d_{1\bar{1}0}$or d_{001}depending on the direction).

The experimental scanning strategy is illustrated in Figure 17. The STEM probe is scanned in a block fashion where each block takes the shape of a diamond (Figure 17a). Each pixel in a block is numbered from 1 to 16 forming the pixel index. The distance between the equal index pixels from neighboring blocks is 17/16 times the lattice spacing in the y and z directions ($d_{1\bar{1}0}$ and d_{001}). The same index pixels are extracted from each block forming 16 moiré subimages. Each of these moiré images are imaged from a sampling grid that is formed by slightly shifted probe positions with a shift vector given by eq. 45 with $g_1 = \frac{1}{d_{11\bar{1}}}$ and $g_2 = \frac{1}{d_{1\bar{1}\bar{1}}}$. The shift of the sampling probe is given by

$$\vec{S}_{k,l} = k(\Delta y - \Delta z)\widehat{g_1} + \ l(-\Delta y - \Delta z)\widehat{g_2}\ (with\ k, l = 0 \ldots 3) \tag{51}$$

with Δy and Δz chosen to be $\Delta y = \frac{d_{1\bar{1}0}}{8}$ and $\Delta z = \frac{d_{001}}{8}$ as sketched in Figure 17b.

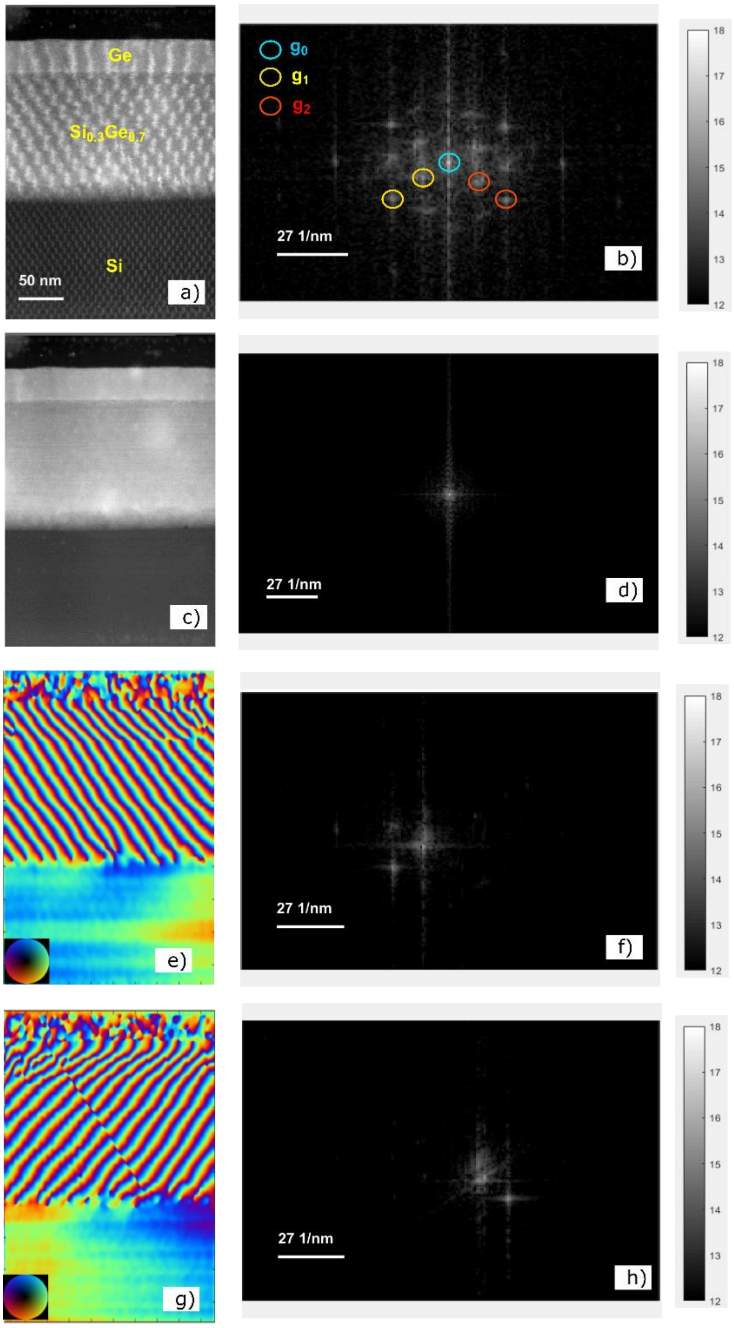

Figure 18 a) Moiré on the 16nm Fin longitudinal direction b) and its diffractogram c) Demodulation to either g_1 and g_2 with a 4x4 shift matrix is shown as the phase of the demodulated wave in y,z-space (e,g) and g0 with the real value in x,y-space (c) and the absolute value of amplitude in frequency space of g_0, g_1 and g_2 (d,f,h).

Applying quadrature demodulation as explained in the previous section, we obtain the demodulated result for $g = g_0$, $g = g_1$, $g = g_2$ with a 4x4 shift matrix as shown in Figure 18. Note the selection of the desired frequencies while a strong suppression of the unwanted frequencies occur. There are two reflections in g1 and g2 corresponding to Si and $Si_{0.3}Ge_{0.7}$ material having different lattice spacings, but both are maintained after the quadrature demodulation process selecting Si as the reference lattice. This shows that the strained components remain while the other unwanted components are strongly suppressed.

The suppression factor for each of the selected frequencies g_0, g_1, g_2 can be calculated (Figure 19). Quadrature demodulation keeps the selected frequencies while strongly suppressing the other unwanted frequencies by destructive interference. The suppression factor of the undesired frequency is the damping factor that is applied to the undesired frequencies while maintaining the desired frequencies. From Figure 19 we can infer that the effect of quadrature demodulation is similar to applying a 2D sinc function[j] enhancement factor centred at the selected frequency while the other frequencies away from the selected frequency are greatly suppressed. As an example, if the frequency g_1 is selected, the suppression factor for the other two frequencies $\frac{Ig_0}{Ig_1} = 4.5e^{-17} \approx 0$ and $\frac{Ig_2}{Ig_1} = 1.5e^{-16} \approx 0$ i.e., the ratio of the absolute value of amplitude of undesired frequency to that of the selected frequency in the Fourier space.

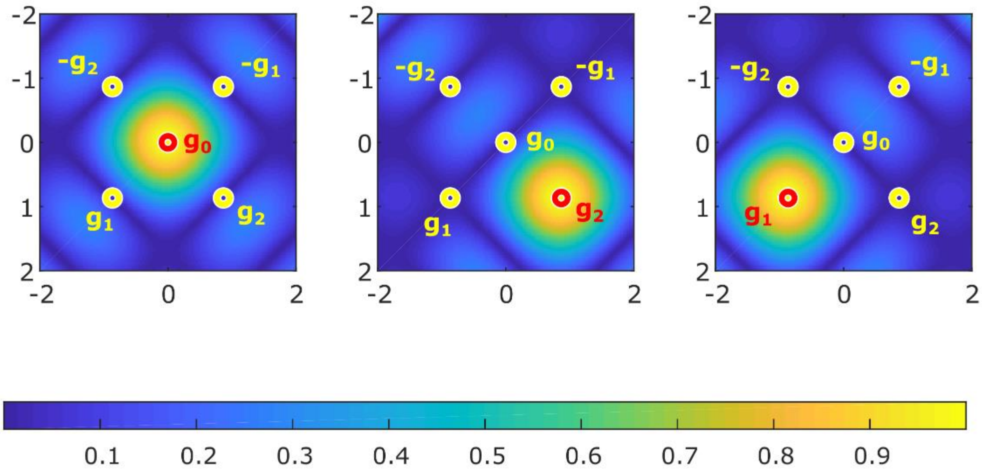

Figure 19 The figure illustrates the enhancement factor applied on three desired frequency sidebands g_0, g_1 or g_2. The centres desired frequencies g_0, g_1 and g_2 are highlighted with the red dot and the centres of undesired frequencies are highlighted in yellow.

---

[j] The sinc function locally modifies and enhances the frequency components of interest. Hence, we use a circular gaussian filtering mask with FWHM 90% for GPA i.e. low damping in order to reduce the effect of further smoothening from the GPA mask.

3.5. Results and discussion

GPA is used to extract strain from any two non-collinear frequency sidebands like g_1 and g_2 that are selected from quadrature demodulation after suppressing the rest of the unwanted frequencies. At first, we will analyse the accuracy and precision of the moiré demodulation technique. To this purpose a reference bulk Ge sample is selected which is epitaxially grown on top of Si substrate (Appendix A2.2) and moiré demodulation technique is applied to measure the lattice mismatch between bulk Ge and Si. The relative difference between the two lattice parameters can be interpreted as an estimate of the accuracy of the technique. Figure 20a shows the 2D moiré image from one of the 16 shifted moiré subimages. Notice the sensitive variation of moiré fringes to the variation in the lattice distances between Si and Ge. The lattice mismatch between Ge and Si measured using the moiré demodulation technique is $\varepsilon_{yy} = (3.9 \pm 0.3) \times 10^{-2}$ and $\varepsilon_{zz} = (3.9 \pm 0.6) \times 10^{-2}$. The values quoted here are the average lattice mismatch in the Ge area (marker in red) and the error values are the standard deviation of the lattice mismatch and is a measure of precision.

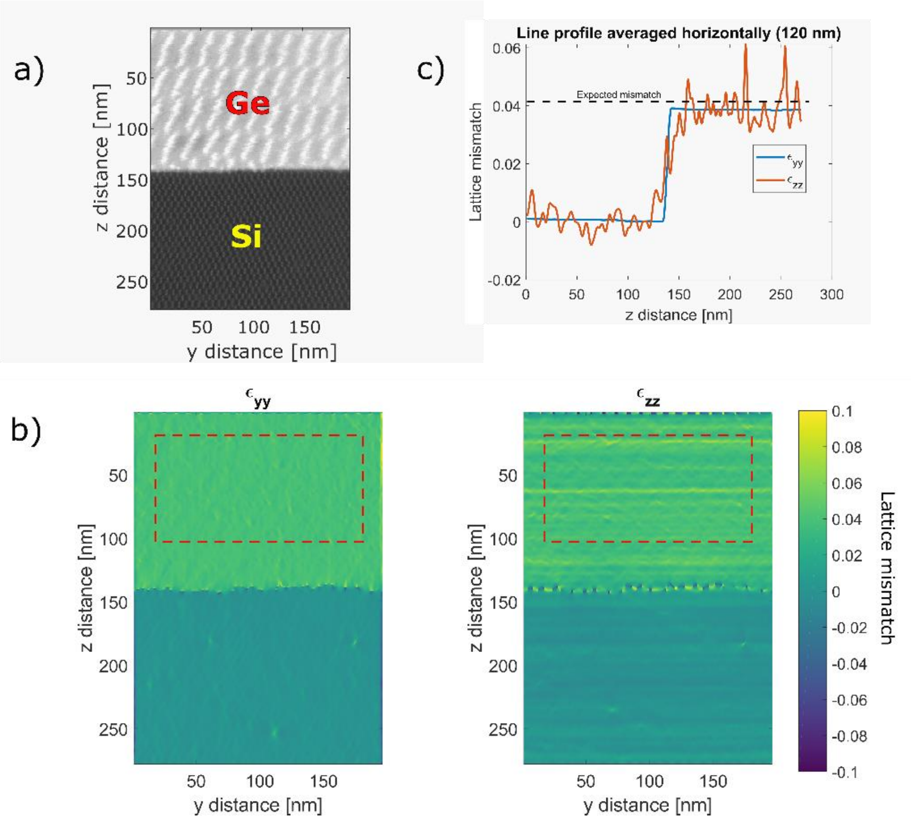

Figure 20 a) 2D moiré on bulk Ge sample on top of Si substrate b) strain maps ε_{yy} and ε_{zz} measured from the moiré demodulaton technique. The horizontal line artefacts in ε_{zz} are the slow scan artefacts due to sample drift and electromagnetic distortions from scan coils. c) Line profile drawn from the strain maps averaged over 120 nm horizontally in the y direction and the dashed line indicates the expected mismatch between Ge and Si.

The precision was observed to have an inverse relation with the spatial resolution (size of the mask in GPA) and the spatial resolution in this case was ~1.5 nm. Better precision can be obtained at the cost of the spatial resolution and the precision degrades to 3.5 x 10^{-3} (In the fast scan direction[k]) while targeting a spatial resolution of 1 nm. Moiré demodulation technique provides an independent choice for the spatial resolution upto one pixel size (in this case 1.0625 times the lattice spacing). The horizontal line artefacts in ε_{zz} in Figure 20 b are due to the sample drift and the electromagnetic distortion of the scan coils and is seen mostly in the slow scan direction during the STEM raster scanning. This also explains the lower precision observed in ε_{zz} in comparison to ε_{yy}. The accuracy measured as average lattice mismatch between Ge and Si is 2 x 10^{-3}.

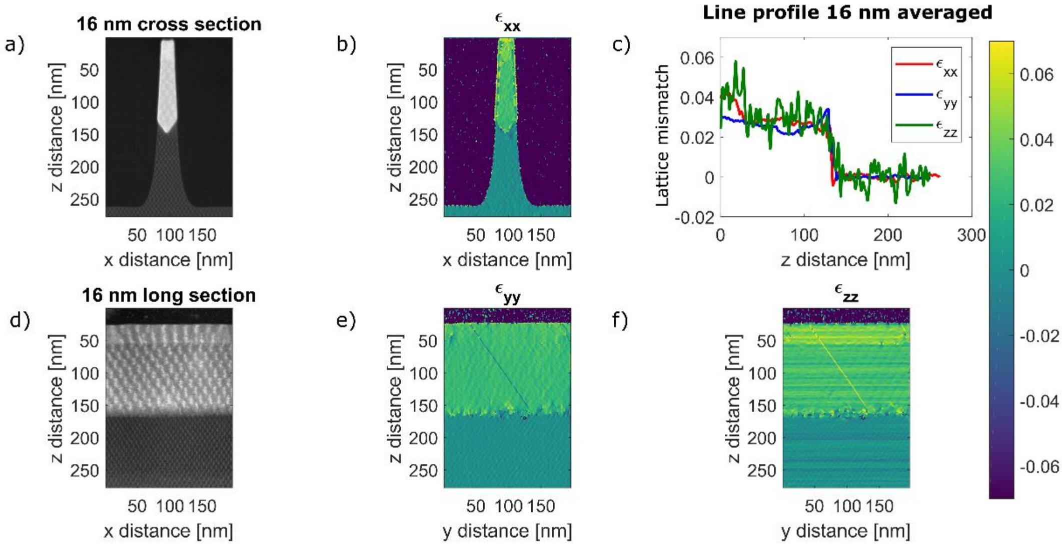

Figure 21 Moiré strain measurement on the 16 nm FinFET along the a) cross and d) long section providing 3D strain information (assuming uniform strain along the thickness of the lamella). f) Slow scan distortions are visible as horizontal lines in ε_{zz} lattice mismatch map, also resulting in a noisier ε_{zz} line profile. c) Line profile calculated from the strain maps, the line profiles are averaged horizontally over 16 nm.

Moiré strain measurement was also applied to a 16 nm FinFET device as shown in Figure 21. Figure 21 a) and d) show the 2D moiré on the cross section and long section TEM lamella of the 16nm FinFET. Lattice mismatch maps in the three perpendicular directions ε_{xx}, ε_{yy} and ε_{zz} are shown with respect to Si substrate. The spatial resolution was ~1.5 nm, chosen by the size of the GPA mask in FT resulting in a precision calculated as standard deviation of strain in the Si substrate region is 3 x 10^{-3} (Fast scan direction). Slow scan distortions due to sample drift and electromagnetic interference of the scan coils or vibration are visible as horizontal lines in the ε_{zz} map. Analysing the strain values in Table 2 (with respect to bulk Ge) for ε_{xx} reveals that there is relaxation of the Ge layer in the x direction. This can be explained

---

[k] In principle two orthogonal acquisitions can be taken by rotating the scan direction so that both ε_{yy} and ε_{zz} are calculated along the fast scan directions, thus eliminating the slow scan artefacts. However, the shear strain will still be affected by slow scan artefacts.

due to the decreased device dimension along the x direction (~16 nm) in comparison to the dimension along z (~27 nm). However, Ge conforms with the lattice distances of $Si_{0.3}Ge_{0.7}$ in the y direction as seen in the ε_{yy} line profile Figure 21 c. Since the Ge lattice is larger than that of $Si_{0.3}Ge_{0.7}$ in its natural state and due to this conformation, it is compressively strained in the y direction. This results in an elongation in the z direction due to the Poisson effect [83] and can be seen in the ε_{zz} line profile. To summarise, a uniaxial strain (y-axis) is seen along the channel of the finFET. The strain is almost completely relaxed across (x-axis) the channel and there is a small tensile strain along the growth direction (z- axis). Again higher standard deviations are observed in ε_{zz} due to slow scan artefacts.

Table 2 Average Strain measured on the Ge region on a 16 nm finFET. The error values are the standard deviations in the measured region.

Technique	**ε_{xx} Ge (across the channel)**	**ε_{yy} Ge (along the channel)**	**ε_{zz} Ge (Growth direction)**
Moiré demodulation	$(-1 \pm 3) \times 10^{-3}$	$(-14 \pm 3) \times 10^{-3}$	$(2 \pm 6) \times 10^{-3}$

3.6. Conclusion

Standard STEM moiré strain mapping using GPA suffers from reduced spatial resolution and interference from unwanted fringes and can lead to unreliable strain maps. A novel demodulation technique based on a generalisation of quadrature demodulation is realised which was shown to significantly improve the spatial resolution (1 – 3 nm) and gives a more reliable and precise strain map ($1\text{-}3 \times 10^{-3}$) at the expense of a somewhat longer acquisition as compared to conventional moiré imaging. However, scan distortions are visible in the slow scan direction due to sample drift and higher pixel acquisition time of 50 - 80 µs to make sure all settling time issues with probe positioning are stabilised and a good SNR is available.The strain information is more reliable in the fast scan direction which would facilitate the calculation of normal strain in that direction. Two orthogonally scanned images can be used to calculate normal strains (to avoid slow scan distortion) in the two perpendicular directions but limits the capability for shear strain calculation. This approach is applicable for epitaxial strain study given that the shear strains are ideally negligible for epitaxially grown materials. The technique also offers flexibility in the choice of field of view especially when compared to atomic resolution HR(S)TEM based methods. The method is near real-time in terms of acquisition and data analysis and provides the capability to trade spatial resolution for precision. Since moiré has the ability to boost strain values, it is highly sensitive and strain precision can be comparable to diffraction based methods without the need for specialised and slow diffraction cameras.

Chapter 4: HAADF-STEM block scanning technique

This chapter contains large excerpts from the published paper:

V. Prabhakara, D. Jannis, G. Guzzinati, A. Béché, H. Bender, J. Verbeeck, HAADF-STEM block-scanning strategy for local measurement of strain at the nanoscale, Ultramicroscopy. 219 (2020) 113099. https://doi.org/10.1016/j.ultramic.2020.113099

First author contributions include experimental design and experimentation, strain analysis, idea formulation and writing the manuscript, D.J was responsible for setting up the scan engine for software control along with python inferface and HAADF multislice simulation, G.G. has contributed with the analysis of Bessel diffraction, J.V has contributions for idea formulation and manuscript revision. The rest of the authors contributed to reviewing the manuscript.

4.1. Introduction

Imaging techniques such as high resolution scanning transmission electron microscopy (HR-STEM) imaging and HRTEM (High resolution transmission electron microscopy) are able to resolve individual atomic columns of a crystal. In combination with image processing techniques like GPA these techniques offer spatial resolution for strain measurement up to a single unit cell. Image patterns obtained by HR-STEM are relatively insensitive to thickness of the sample and can also work with slightly thicker samples (~200 nm) as opposed to HRTEM, which requires thinner samples ~50 nm leading to larger strain relaxations [84]. However, the field of view in HRSTEM is typically rather limited (< 50 nm section 2.1.1.1) due to necessary acquisition time to scan large areas with atomic resolution sampling which introduces artefacts due to sample drift. To obtain higher fields of view, scanning moiré fringe strain mapping was introduced and we have shown in the previous chapter that using a novel moiré demodulation technique it is possible to obtain a tuneable spatial resolution and precision, and accuracy of 2 x 10^{-3}.These imaging techniques are fast and reliable, but are often plagued by artefacts in the slow scan direction. The diffraction techniques introduced in chapter 2 can overcome these difficulties and provide a precision up to 2.5 x 10^{-4} and an accuracy of 1 x 10^{-3} at best (as measured on a Ge reference sample (Appendix A2.2). The diffraction techniques in general require specialized cameras to acquire the high dynamic range of diffraction patterns in a reasonable amount of time and complex processing steps and dedicated software is required for strain analysis. Thus, the imaging techniques are fast and cost effective but there needs to be an approach to overcome or reduce the slow scan artefacts which are a major limitation. In addition, it is necessary to provide a wider field of view at the same time so that the technique becomes attractive to be adopted in a widespread manner.

Predominant scanning distortions arise from instabilities like spatial drift, electromagnetic interference or vibration and from the “flyback effect”, when the electron probe scanning system needs time to move from one end of the line to the starting of the next line in a conventional raster scan scheme. This results in image distortions which are particularly problematic when measuring the subtle effect of strain on the lattice image. Over the years, several image correction techniques have been proposed in literature which depend on multi-frame scanning and using rigid or non-rigid registration to average the multiple frames and estimate the deformation of the images [50,85]. The pixel dwell time used in each frame is rather short (≈ 0.5-1 µs) and the field of view is limited due to the required sampling of the crystal lattice and the limited amount of pixels in the image [86]. Exploiting priori assumptions, Jones and Nellist were able to correct for scan noise and drift in STEM images [87]. Sang and LeBeau have shown that near perfect STEM images can be reconstructed using the RevSTEM (Revolving scanning transmission electron microscopy) technique, where a series of rotated images of the same area are used to estimate the drift rate and direction without prior information [88]. These methods require multiple acquisitions of images resulting in a higher incoming electron dose (risk of beam damage), longer recording time and rely on the assumption that the drift is constant in time.

Alternative scanning strategies using spiral scans were also investigated by Sang. et.al. which eliminate the flyback effect common in conventional raster scanning. The spiral scans offer very fast acquisitions but suffers from non-uniform sampling of the image leading to blurring of image detail near the edges and a loss of contrast [89]. Ophus et.al. have proposed a linear and nonlinear drift and scanning artefact correction using two orthogonally scanned images [90]. This method is based on the near perfect information transfer in the fast scan direction but requires significant processing steps and sufficient low frequency information such as edges or alignment markers for atomic resolution images acquired along low-index crystallographic zone axes.

In this chapter, we introduce a new scanning strategy termed ‘block scanning’, where the probe scans the sample in a block by block fashion. Each block consists of a patch of atomic resolution image of the sample which can be used to evaluate the local strain in that region. This reduces the drift distortion, which is prominent in a conventional raster scan as each block can be assumed to be near drift free given the much shorter recording time of an individual block. The method allows flexible tuning of spatial resolution and the specimen can be sampled at sparse locations, therefore allowing a wider and freely adjustable field of view while maintaining atomic resolution sampling within the subimages. Assuming a 16 bit dynamic range in the scan engine’s DAC (digital to analog converter), and accompanying low noise performance in the scan coil drivers, potentially results in a maximum field of view of several µm, sufficient to cover the entire thin area of most TEM samples. This assumes also that dwell times are chosen such that settling time issues of the scan system are not resulting in extra distortions.

4.2. Block scanning strategy

In a raster scanning mode HAADF-STEM, the beam scans over the sample in a row by row fashion. This creates a fast scan direction for the rows and slow scan direction for the columns. Due to instabilities such as spatial drift, electromagnetic interference or vibration, the lattice spacing information gathered is typically much more reliable in the fast scan direction as opposed to the slow scan direction. A modified scanning strategy is employed here, where the beam scans individual subimages consisting of a low number of pixels, each requiring only a small fraction of the total exposure time (Figure 22). This modified scanning strategy significantly reduces the delay in the slow scan direction and hence we expect the local lattice measurements to be more robust against sample drift. Each individual subimage is expected to provide relatively reliable lattice information in both the fast and slow scan direction in comparison to the raster scan. As long as the subimages are treated independently from each other, slow drift phenomena (> 100 ms) have a less significant effect as will be demonstrated in the results section. Although the precise limits of the technique depend on the instantaneous drift rate, we show that the proposed block scanning indeed succeeds in reducing slow scan distortions in comparison to the conventional raster scan. Note that also the flyback artefacts are significantly reduced as the total distance the probe has to move is now reduced to the distance between individual subimages. There however, is a large jump from the last subimage in the row to the left subimage in the next row which distorts a few pixels in that subimage. Hence, we do not consider the first column of subimages for the analysis. This problem can be mitigated by taking a smaller jump to the subimage in the next row by reorganising the order of the scanned blocks.

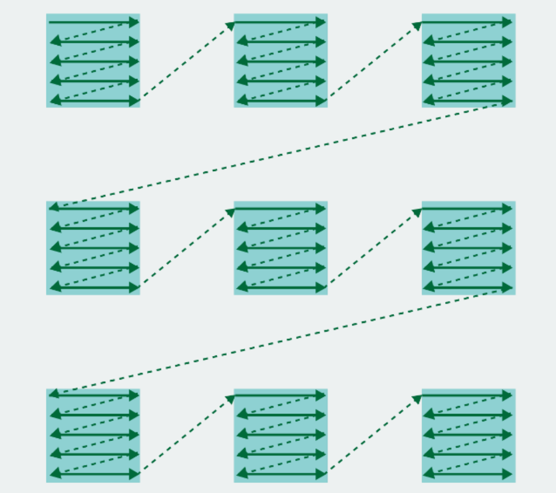

Figure 22 Schematic representation of the block scanning strategy. The solid lines are the path taken during the scanning. The probe performs raster scan locally inside each block. The dashed lines indicate the spatial jumps taken by the probe while scanning.

To implement the proposed idea in a transmission electron microscope, a custom scanning engine [81,82] is used to dynamically control the probe position. Full software control over the scanning grid is obtained on an aberration corrected Thermofischer Titan microscope operating at 300 kV. The subimage sampling can be chosen by fine tuning the scan step size (distance between the probe visiting positions or the pixel size) and the number of pixels. The field of view is determined by the number of subimages and the distance between them. In essence, the scan pattern is tuneable and the subimages can be placed next to each other in order to not skip any sample information in between the subimages. The block scanning strategy allows for an extended field-of-view up-to 200 - 250 nm as long as the Nyquist sampling criterion is satisfied inside each block. Figure 23 is an illustration of the block scanning technique on the cross section TEM sample of the 16 nm FinFET. The sample was oriented along the [110] zone axis. The subimage sampling is tuned so that each block consists of 3 ½ to 4 unit cells (1.5 x 2.2 nm^2, Figure 23b) spanning approximately a total area of 192 x 282 nm^2. There is a spacing of one block (1.5 nm in y and 2.2 nm in z) between each block. Each block consists of 32 x 32 pixels, with a pixel size in y ≈ 0.047 nm and z ≈ 0.069 nm (rectangular pixel). This rectangular scanning grid is used to satisfy the Nyquist criteria in each block in agreement with the rectangular lattice. Alternatively, we have also used a 64 x 64 pixel block, yielding a spatial resolution (block size) of 3 nm and a total field of view of 192 x 192 nm^2 with no spacing between the blocks, using square sampling, as the Nyquist criterion for this field of view was easier to satisfy.

The total number of pixels used was 4096 x 4096 in both cases resulting in 64 x 64 subimages. We will compare the performance of both sampling choices further on. We use a dwell time of 20-50 µs to make sure all settling time issues with probe positioning are stabilised and a good SNR is available. In principle, one unit cell is sufficient to allow measuring the vectorial distance between two neighboring atoms, which is all that is needed for strain measurement. Sampling multiple unit cells inside a block however comes with the advantage that there are many unit cells or repetitions on which e.g. scan distortions and local defects are averaged resulting in an increased precision. We show later in the results section that using on average more than 6 unit cells per block provides strain precision that outperforms the HRSTEM method in the slow scan direction.

The precision of the strain measurement in principle is weakly dependent on changes in the pixel aspect ratio. In the presence of the scan distortions and detector noise, it is beneficial to sample multiple unit cells inside the block to increase the robustness of the non-linear fitting (block processing), which will be discussed in the next section. As these artefacts are unavoidable, a rectangular scanning grid can be useful as it allows to collect a similar number of samples per unit cell in the orthogonal [110] and [001] directions.

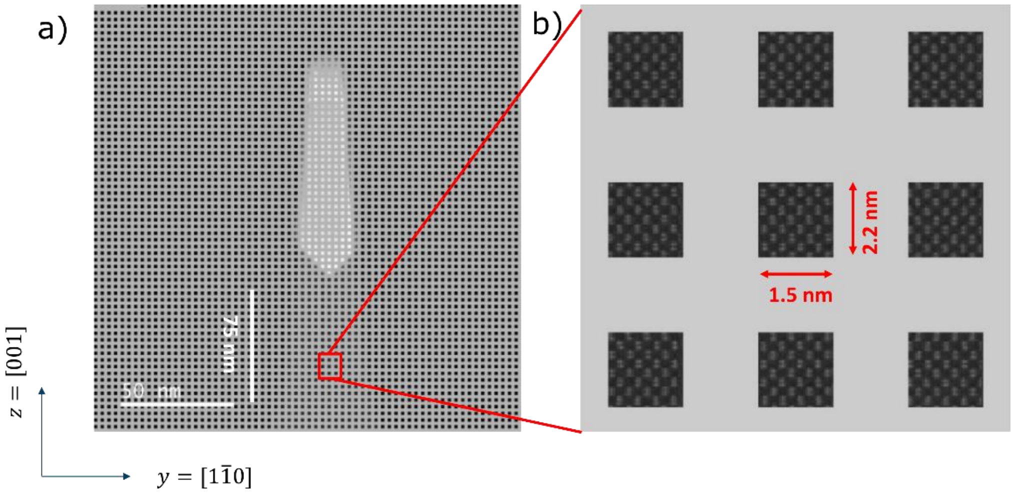

Figure 23 a) Experimental block scanning STEM image of a 16 nm FinFET in the long section b) showing individual blocks in the Si region and each block consists of 32x32 pixels and covers approximately $3^{1}/_{2}$ to 4 unit cells.

The goal now is straightforward to extract lattice parameters from each of the individual subimages. Since there is a limited number of pixels inside each block, conventional techniques like GPA cannot be applied because GPA relies on information in the Fourier transform (FT) of the block. With 64 x 64 or 32 x 32 pixels, the FT lacks the frequency resolution to estimate strain accurately and a more sophisticated approach is necessary to obtain high frequency resolution in the Fourier domain with a limited number of pixels or samples. Hence, a parametric approach is taken where a model-based fitting or regression is used to fit the image data in real space inside each block. Block scanning can be seen as an imaging equivalent of the NBED technique. However, contrary to the diffraction techniques, it could be prone to beam tilt induced distortion when scanning high fields of view.

4.3. Non-linear regression and strain calculation

Each block consists of a few atom columns (unit cells) and the atoms have a periodic lattice arrangement. This periodic lattice can be decomposed into a discrete sum of 2D sinusoids with only a few harmonics, analogous to a Fourier series decomposition of a periodic function. We construct a model F(x,y) for regression analysis by computing the Fourier transform (FT) of each block. This gives an indication of the expected sinusoidal components representing each block (Figure 24b) but suffers from the fact that the small image patches are not strictly periodic (even though the underlying crystal is) because of the incommensurate cut at the image boundaries.

$$F(x,y) = A_0 + \sum_{n=0}^{N} \sum_{m=0}^{M} A_{m,n} sin\big(2\pi\big(nf_x x + mf_y y\big) + \emptyset_{m,n}\big) \tag{52}$$

Where, A_0 is the background intensity, $A_{m,n}$ is the amplitude of the 2D sinusoids, f_x and f_y are the spatial frequencies in the cartesian coordinate system, $\emptyset_{m,n}$ is the phase of the sinusoids and M and N are the maximum number of harmonics in the model. The Levenberg-Marquardt nonlinear least-square minimization [91] algorithm is applied to extract the parameters of the 2D model and using this regression method to compute the value of strain inside each sub-image. Since the model is nonlinear in f_x, f_y and $\emptyset$, the least square minimization algorithm requires a good initial guess to avoid getting stuck in a local minimum. The amplitude and phase of the sinusoidal components are estimated initially from the discrete 2D FT at the specific location of each diffractogram spot. The background value is estimated from the mean intensity value in the subimage. An illustration of the initial guess and a subimage after fitting using the Levenberg-Marquardt algorithm is shown in Figure 24c and Figure 24d for a 64x64 pixel block.

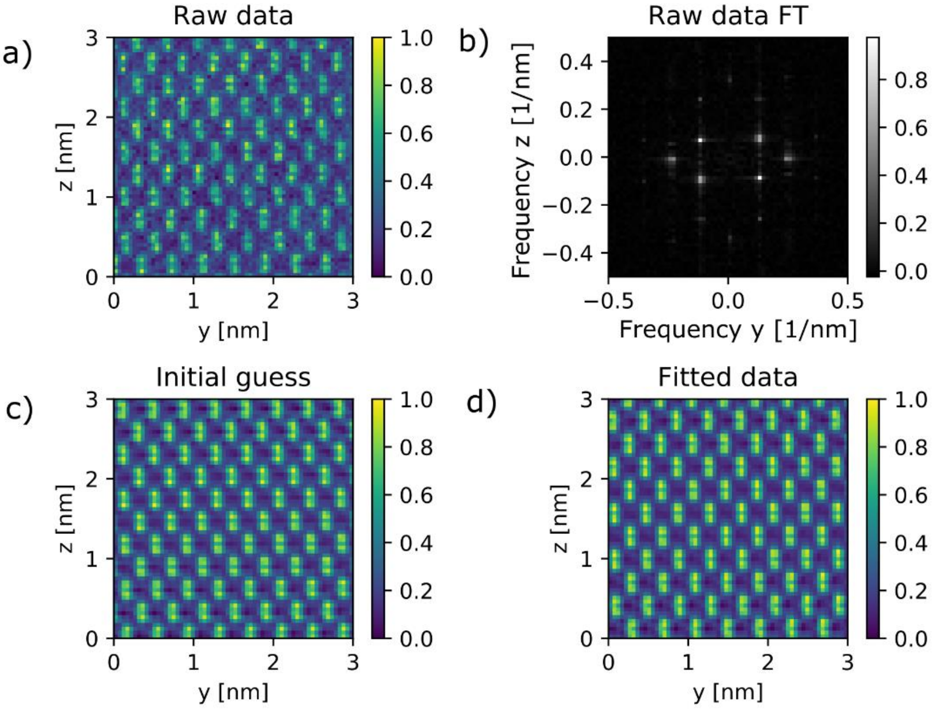

Figure 24 a) Raw data of a block and its corresponding FT b). The amplitude of the frequency spectrum is shown with the low frequency component or the background removed to highlight the higher order frequency components, since the higher order components are masked with the high intensity background c) Initial guess computed from the FT of the raw data and d) fitted block using Levenberg-Marquardt non-linear least squares minimization. The intensities of the data are normalised to have the same scale and better visualisation

The frequency vector $G = (f_x, f_y)$ of the 2D sinusoids is inversely proportional to the lattice spacing of the crystal and gives a direct indication of the lattice strain after comparison with the reference frequency vector G_0. The 2D distortion matrix D is given by:

$$D = (G^T G_0)^{-1} - \mathrm{I} \tag{53}$$

Where, I is the identity matrix and G^T is the transpose of G. The strain and rotation are calculated as

$$\varepsilon = \frac{1}{2}(D + D^T) \tag{54}$$

$$\omega = \frac{1}{2}(D - D^T) \tag{55}$$

4.4. Experimental results

A comparison of the proposed block scanning technique with the conventional raster scanning for a dwell time of 24 µs scanned over exactly the same area of a reference Si sample, which is assumed strain free is shown in Figure 25. At first, a comparison between GPA and the block processing(non-linear regression) was done to evaluate the performance of the block processing approach. Figure 25a and Figure 25b show the strain maps analysed for the raster scanned image with GPA and block processing approach. Block processing is applied on the raster scanned data by selecting 252 x 252 sub-images of 64x64 pixels, selected from the original 4096 x 4096 experimental image. Streaking artefacts in the horizontal direction are seen in the strain maps in the slow scan direction ε_{zz} due to misalignment between adjacent rows originating from sample drift. In both cases the spatial resolution is approximately 3 nm, determined by the selected subimage (block) size for the block processing and the appropriate choice of the mask in the Fourier space for GPA.

The resulting strain maps (Figure 25 a,b) look qualitatively similar and quantitatively, the precision obtained in the slow scan direction ε_{zz} using GPA and block processing is 11.6 x 10^{-3} and 10.6 x 10^{-3} respectively. The precision obtained in the slow scan direction is not reliable to extract device information. The precision in the fast scan direction is 2.8 x 10^{-3} for GPA and 2.9 x 10^{-3} for block processing. The fact that both processing methods lead to comparable results, demonstrates the suitability of the block processing algorithm. Figure 25c shows the strain map with block scanning and block processing. The standard deviation on the strain observed in the slow scan direction for the block scanning is 3.6 x 10^{-3} demonstrating a more than threefold improvement in the precision is possible using the proposed block scanning technique. In the fast scan direction, the precision value obtained was 2.2 x 10^{-3} slightly outperforming the conventional raster scan.

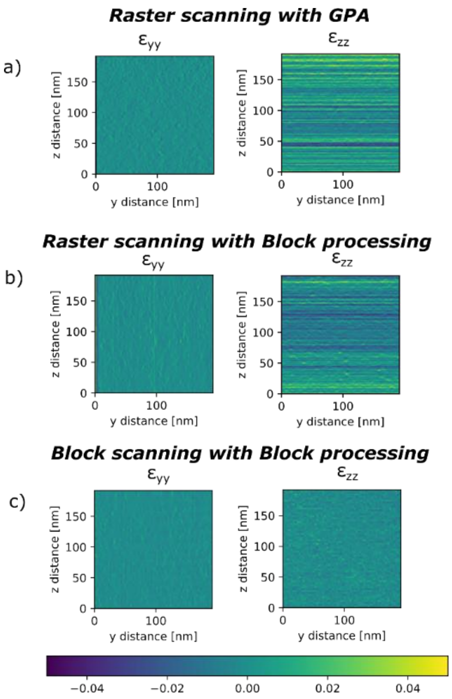

Raster scanning with GPA

Raster scanning with Block processing

Block scanning with Block processing

Figure 25 Comparison of strain performance of conventional raster scanning with the a) GPA analysis and the b) block processing approach. The raster scanned image is segmented into blocks and block processing (Non-linear fitting) is applied to each block. c) Block processing applied on the block scanning image. The strain maps shown are along the fast scan ε_{yy} and the slow scan ε_{zz} direction on an unstrained Si reference sample. *The data acquisition is performed with a pixel dwell time of 24 µs, 85 pA beam current at 300 kV .The block size is 64x64 pixels spanning approximately 3x3 nm^2. Note the qualitatively similar result between GPA (a) and block processing (b) for the raster scanned images and a significant reduction of drift induced artefacts in the block scanning case (c), especially for* ε_{zz}.

Now that we have established the potential for strain mapping, we apply the technique on the 16 nm Finfet and evaluate the results against Bessel beam diffraction experiments on the same sample. Experimental strain maps analysed with a 64 x 64 pixel block configuration on the 16 nm FinFET in the cross and the long section configurations are shown in Figure 26 with respect to the underlying Si substrate as reference. Spatial maps and line profiles are compared with the Bessel diffraction results.

The strain value in the Ge region (initially computed with Si as reference) is converted to bulk Ge as reference, because the actual strain with respect to the same Ge material is of importance. Table 3 shows the strain values in the Ge region calculated after conversion to the bulk Ge reference. Analysing the values reveals that the strain is almost relaxed in the x direction (across the fin), which can be understood due to the small width of the fin [11], where the lateral dimension of $Si_{0.3}Ge_{0.7}$ (~16 nm) is smaller than the thickness of the grown Ge layer (~25-30 nm). There is a compressive strain along the fin in the Ge region which can be understood from the lattice mismatch between the $Si_{0.3}Ge_{0.7}$ and the Ge channel. Due to the compression of the lattice in the y direction, there is a small tensile strain in the vertical direction in z, due to the Poisson effect.

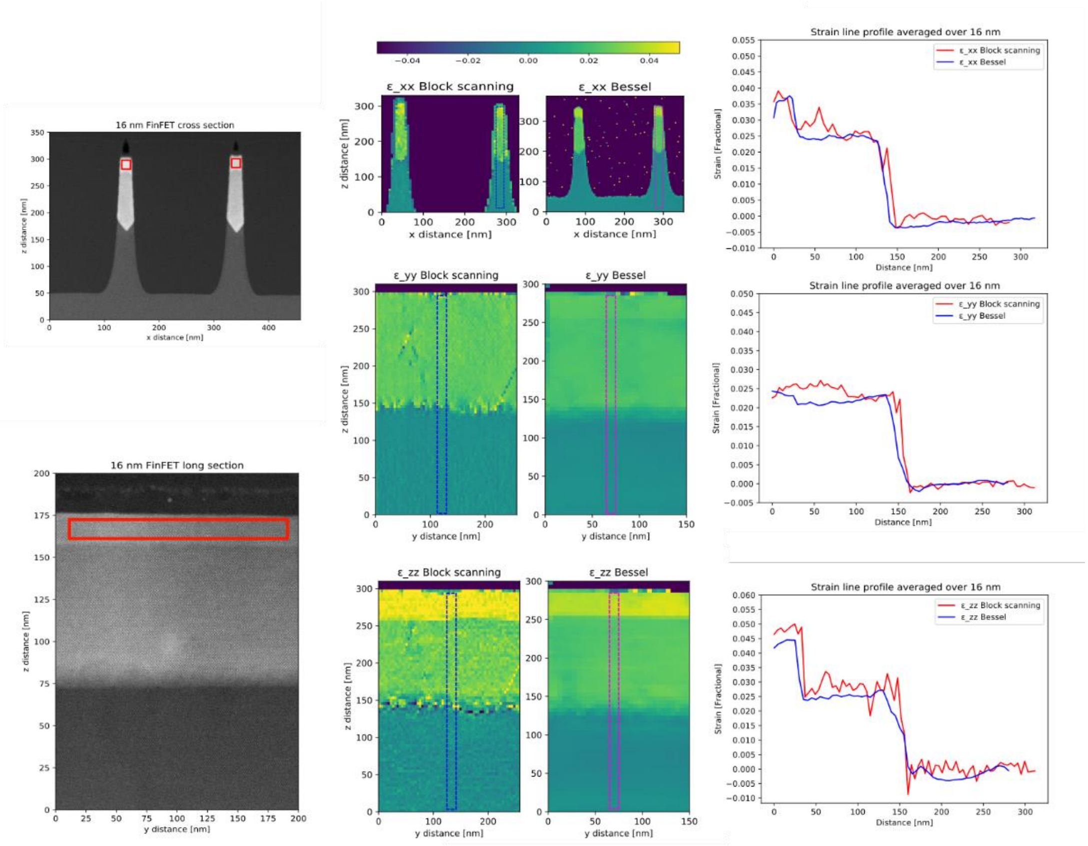

Figure 26 Strain/lattice mismatch maps on the 16 nm FinFET in the cross section and the long section and a comparison with the Bessel diffraction technique with respect to the Si substrate. The line profiles are averaged over 16 nm as indicated in the dashed blue box in the strain maps. The HAADF image on the left shows the cross section and the long section of the 16 nm FinFET and the Ge area is highlighted in red.

The block scanning technique probes on the local unit cell level and if any defects are captured in the subimages, results in the highlighting of the local defect as an artefact as observed in Figure 26. The Bessel diffraction method intrinsically averages over a larger probe size, making it less prone to e.g. local defects. Both the methods are different also in another subtle aspect: the different incoming probes and detection methods will lead to entirely different depth of focus effects which may become relevant in samples where strain is a function of depth in the sample. This can be observed e.g. in the TEM samples in the long section (Figure 3), where one can notice that the v-shaped interface between the Si and Si$_{0.3}$Ge$_{0.7}$ is buried. This results in probing the average strain of the Si and Si$_{0.3}$Ge$_{0.7}$ near the interface for the Bessel diffraction owing to the lower depth resolution of the Bessel beams as opposed to the HRSTEM probe used for the block scanning. The latter, having a much higher depth resolution and being focused on the top-surface of the sample, may not detect the strain of buried sections of the sample. This can be observed in the line profiles of ε_{yy} and ε_{zz} in Figure 26, where a gradual Si – Si$_{0.3}$Ge$_{0.7}$ interface is observed for the Bessel diffraction, while a sharp interface is observed for the block scanning. The former is related to the average strain over the sample thickness, while the latter appears to measure only the strain in the sample's top surface (as observed for the v-shape interface buried within 8 nm from the top surface) .

This is understandable, given that the top surface of the sample has a dominant contribution to the HAADF signal implying that the strain information throughout the thickness of the sample is not deciphered.

The strain precision per block was measured as the standard deviation over the Si reference and for the block scanning the precision is 1×10^{-3} in the fast scan direction and 3×10^{-3} in the slow scan direction. The precision is slightly lower in the slow scan direction due to drift and distortions that can still take place during the line scan inside a block, but the effects are reduced drastically in comparison to the conventional raster scan (with a three fold improvement as demonstrated in Figure 25). The precision decreases three-fold with the use of 32 x 32 pixel blocks due to the lesser number of pixels used to estimate the parameters of the model.

Table 3 Average strain values measured in the Ge region. The error values are the standard deviation of strain in the Ge region. The error values show higher standard deviation in ε_{yy} and ε_{zz} for Bessel indicating that the deviation could be due to sample non-homogenity or the amorphous SiO_2 surrounding the finFET (More details in finFET strain comparison in section 6.4)

Technique	ε_{xx}	ε_{yy}	ε_{zz}
Block scanning	$(-3 \pm 2) \times 10^{-3}$	$(-15 \pm 2) \times 10^{-3}$	$(6 \pm 3) \times 10^{-3}$
Bessel	$(-3 \pm 1) \times 10^{-3}$	$(-14 \pm 2) \times 10^{-3}$	$(4 \pm 3) \times 10^{-3}$

4.5. Sinusoidal harmonic model validation

To further validate the model based estimation of strain from block images, HAADF multislice simulations were performed to generate hypothetical noise free HAADF images that are devoid of scan distortions and sample drift (Figure 27a). These simulations allow us to determine the potential presence of bias in the regression process due to the use of a simplified harmonic model for the underlying image formation. The aberration values were chosen close to the experimental conditions with defocus = 2 nm, two fold astigmatism A1 = 966.8 pm and spherical aberration Cs = -274.8 nm. The parameters were estimated using the probe corrector software during the start of the experiment. Images of a layered strained structure of Si are simulated by artificially varying the lattice parameter with strain values varying from -0.05 up to 0.05 on top of an unstrained Si substrate. The size of individual blocks was set to 64 x 64 pixels (Figure 27a). The simulated data was then treated with the same optimisation algorithm as used for the experimental images.

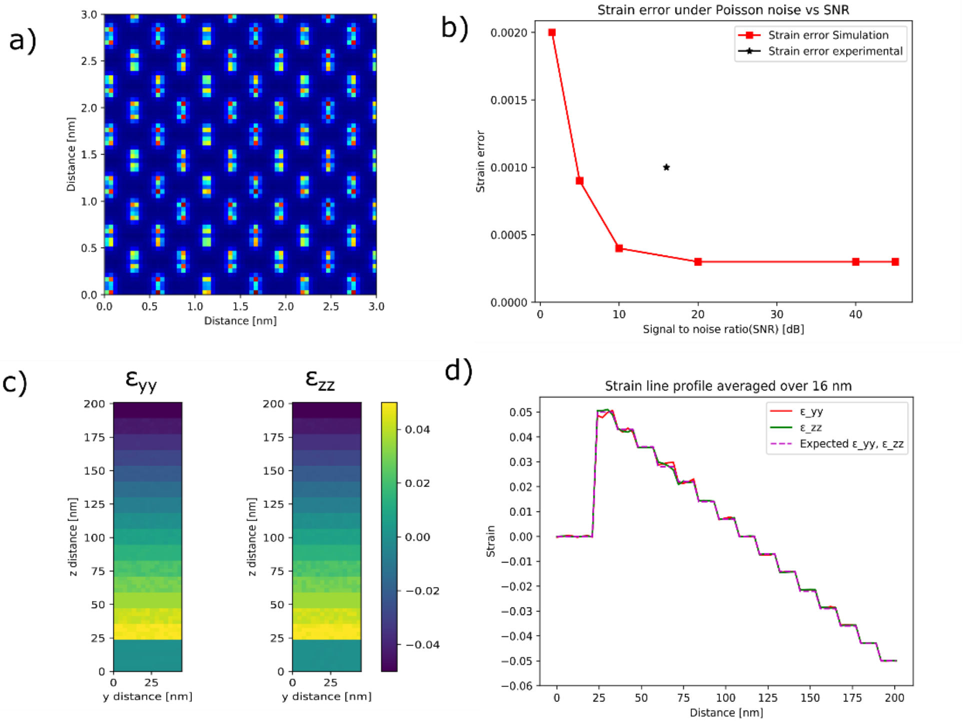

Figure 27 a) Simulated block of 64x64 size and 3x3 nm^2 area c) Strain map showing the simulated layered structures with strain profiles from -0.05 up to 0.05 on top of an unstrained structure d) Line profile obtained from the strain map averaged horizontally across 16 nm b) Strain error, which, is a combination of precision and bias, calculated as a function of SNR under the addition of Poisson noise

The best possible precision and accuracy as calculated on the simulated subimage data set of 64 x 64 pixels (spatial resolution/subimage size of 3 nm) are 2×10^{-4} and 4×10^{-4} respectively. These values are highly attractive for strain mapping in nanostructures. The small amount of bias leading to a finite accuracy is due to the simplified model that represents the HAADF image with a sum of a few sinusoids with their harmonics and might include numerical uncertainties. It is observed that there is a slight bias in the strain value depending on the position of the crystal lattice in the subimage. This bias decreases significantly when increasing the number of pixels in a subimage and varies also with the number of unit cells inside the block or indirectly to the periodicity of the sinusoids. This is confirmed by simulating two data sets: 1) 32 x 32 pixels block with 1.5 nm spatial resolution (block size) and a 2) 64 x 64 pixels block with 3 nm spatial resolution. The accuracy improves significantly from 2 x 10^{-3} in the former case to 4 x 10^{-4} in the latter clearly indicating the significance of spatial resolution i.e., the number of repetitions/periodicities of the unit cell inside the sub-image that determines the accuracy of parameter estimation of non-linear sinusoidal model. In a realistic scenario, increasing the number of pixels in a subimage would also lead to more drift inside the block and this would experimentally lead to more distortions in the slow scan direction. Hence, there is a trade-off between the number of pixels inside a block (and the spatial resolution) and the attainable precision and accuracy. In addition, Poisson noise was added to the simulated subimage to mimic the counting noise of the HAADF detector (Figure 27b). It can be noticed that the precision scales, as expected, as a square root function of the number of counts, with a plateau setting in from an SNR of about 20 dB. This indicates that the systematic errors are introducing a bias from this point on. The bias can be due to sampling, model inaccuracies and numerical implementation, and should not influence the result more than 4 x 10^{-4}. This bias effect we find is far lower than any of the experimental precision results obtained throughout this manuscript and conclude that for our purposes the harmonic model is more than sufficient to model the underlying image data.

During the experimental data acquisition, we choose a beam current of 85 pA at 300 kV during image acquisition. A convergent beam electron diffraction (CBED) pattern is simulated and the expected number of electrons N falling on the HAADF detector (with an inner collection angle of 44 mrad and outer angle of 190 mrad) is estimated for the given current and the acquisition time of 24 µs. The SNR is calculated as N following the Poisson statistics, which yields an SNR of 16 dB for the experimental data. At this level of SNR, we expect the precision to be dominated by the remaining bias issues and are no longer SNR limited. Moreover, in the practical realisation of the experiment, more sources of bias exist, such as sample drift and probe control inaccuracies that will further increase the effect of bias on the obtained strain values.

To finally evaluate the model on the experimental data, a NRMSE (normalised root-mean square error) between the fitted model and the experimental data of the 16 nm finFET long-section (Figure 3) is shown in Figure 28. NRMSE is a measure of similarity between 2 data sets or models with different intensity scales. It ranges between 0 to 1 with 0 being the most similarity between the data set and the model, and 1 representing the highest deviation between both sets. It is calculated as the division between the RMSE (root-mean-square error) and the range of the data set.

$$NRMSE = \frac{RMSE}{x_{max} - x_{min}} \tag{56}$$

$$RMSE = \sum\nolimits_{N} \frac{(x - x_{model})^2}{N} \tag{57}$$

Where x = data points, x_{model} = data points from the model, N = number of data points, x_{max} = maximum of the data, x_{min} = minimum of the data

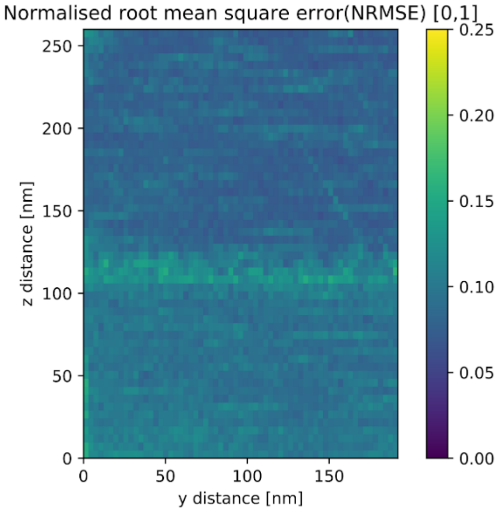

Figure 28 *Normalised Root Mean square error (NRMSE) of the 16 nm FinFET long section in the range [0,1], after fitting each block with the model. Some features exist near the interface, indicating that here, our assumption of uniform strain in the sample thickness direction is not valid. The mean and standard deviation of the NMRSE are 0.09 and 0.04 indicating a good fit with the model. There is no particular trend seen in the plot (apart from the interface) indicating that the residuals are indeed random and the model is a good representation of the data.*

We observe a higher residual near the Si - $Si_{0.3}Ge_{0.7}$ interface due to the reduced contrast in the subimages, related to the projection of regions where strain is not uniform across the thickness of the sample. Such non-uniformity breaks the alignment of the atoms along the direction, leading to lower 'high-resolution' contrast and apart from this region, the residual is featureless. Hence, to conclude the section, the model is evaluated against simuated and experimental data and the results indicate that the model is adequate for the underlying atomic resolution subimages.

4.6. Conclusion

The block scanning technique efficiently minimizes the drift and slow scan distortions that are typically hindering the use of HRSTEM imaging for strain measurement. Moreover, the method provides a larger and flexible field of view in comparison to conventional HRSTEM imaging while maintaining a reasonable recording time and total electron dose. An analytical harmonic model is constructed for each individual subimage starting from initial parameters obtained from its Fourier transform. Using model based non-linear fitting, the parameters of this model are estimated and reveal the local strain in each block independently. This technique is demonstrated on a 16 nm FinFET device, and the measured strain is compared with the Bessel diffraction setup. Although the precision obtained with the block scanning technique is comparable to HRSTEM and slightly below what is attainable with Bessel diffraction, the technique offers a much wider field of view in comparison to conventional HRSTEM and requires no specialised diffraction cameras which suffer from longer exposure times due to limitations in readout speed. The technique is also data efficient in comparison to diffraction techniques and is computationally straightforward to implement.

Chapter 5: High resolution tomography

The TEM techniques discussed in the previous chapters are based on strain analysis of projection images or diffraction patterns along specific crystallographic zone axes. To calculate strain along the three cartesian coordinates, in principle two orthogonally prepared samples are necessary i.e., along the cross section and the long section (Figure 3). Even though with this approach, we extract strain information along the x,y and z coordinates, it is not a true representation of 3D strain because of the inability to decipher the strain distribution along the projection direction. So far, there hasn't been a technique to measure strain in 3D for Si-Ge semiconductor devices. In this chapter, we approach this problem by attempting high resolution (atomic) tomography which is a technique capable of providing a three dimensional reconstruction of the sample/crystal under consideration, as such enabling the visualisation of the atomic arrangement through the crystal. This potentially provides us with a complete 3D strain analysis of the sample and this chapter will explore this potential. One of the main challenges for this technique is the sample preparation because unlike nanocrystals which are studied in literature[92,93], semiconductor devices require FIB prepared samples. Such samples are prone to ion-beam induced damage resulting in a thick amorphous sidewall (~25 nm), inhibiting imaging high-resolution atomic features. Hence, sample preparation methods to overcome this limitation are described in section 5.2.1. In the next section, we will present a high resolution tomography experimental protocol starting from image acquisition to alignment and 3D reconstruction. Once a 3D reconstruction is obtained, 3D GPA will be implemented to analyse strain directly in 3D and the measured strain values will be compared with diffraction-based techniques like NBED and Bessel diffraction. The proof-of-concept results obtained by high resolution tomography-based 3D strain analysis on Si-Ge test/blanket structure will be discussed along with the advantages and limitations.

5.1. Introduction to high resolution electron tomography

Modern aberration corrected TEM provides the capability to image individual atomic columns of the specimen with a spatial resolution well below 0.1 nm. In semiconductor metrology, the acquired TEM images are mostly projection images of the crystal specimen along one of the crystallographic zone axis. Hence, they lack the ability to visualise the individual atomic arrangement along the projection direction or the thickness of the sample. "Electron tomography" can overcome this problem by computing a 3D reconstruction of the specimen from various projection images acquired along different tilt angles. Electron tomography in combination with HAADF STEM, for which the image contrast depends on the composition (approximately Z^2 with Z being the atomic number) and thickness, satisfies the projection requirement [94]. The projection requirement states that each projection image of a tilt series for electron tomography should be a monotonic projection of a physical property of the sample under investigation [95,96]. On the other hand, TEM imaging does not necessarily satisfy the projection requirement for the crystalline samples due to diffraction contrast arising when the sample is orientated along a zone axis, which is not a monotonic variation as a function of thickness or atomic number [97]. Ever since the demonstration of electron tomography in combination with HAADF STEM by Midgley and Weyland [94], electron tomography has become a major characterisation method in material science [92,93,98–101] for example, characterisation of core-shell heteronanocrystals [102,103].

5.1.1. Basic theory and principle of electron tomography

In 1917, mathematician Johan Radon laid out the theory of projections [104]. According to the theory, the projection of an object function $f(x, y)$ can be described by a line integral along the projection direction.

$$F(t,\xi) = \int_L f(x,y)ds \tag{58}$$

where, ds is the differential element along the projection direction. The Radon transform converts a cartesian coordinate object function in (x, y) into Radon coordinates [104] (t, ξ), with t being the distance of the projection line from the origin and ξ is tilt angle with respect to x. A number of these projection images (Radon transformed images) can be back-projected using algorithms like FBP (Filtered-Back projection) [105], resulting in the reconstruction of the original 2D/3D object. In essence, the analytical reconstruction techniques like FBP require a continuum of slices of the Fourier space to ascertain the object information. However, in experimental tomography, a limited number of slices/ tilt angles are obtained for example, due to the limited tilt range of the sample holder and this leads to a “missing wedge” [88]. In practice, the 2D projection images are analogous to slices in the Fourier space and each slice is oriented perpendicular to the projection direction. Due to the limited number of projection directions, the Fourier space is not entirely sampled, resulting in the “missing wedge”. For example, for a tilt range of -70° to 70° results in a missing wedge of 40°. Missing wedge artefacts greatly influence the reconstruction quality, leading to resolution loss especially in the direction perpendicular to the tilt axis [94]. In the next section, we will introduce algebraic reconstruction techniques that provide an improved reconstruction by exploiting a model based approach and the optional ability to incorporate prior knowledge of the object or the data acquisition.

5.1.2. Algebraic reconstruction algorithm

Algebraic reconstruction techniques (ART) provide a more accurate reconstruction for the limited tilt series images (e.g. -70° to 70°) in comparison to analytical techniques like Filtered-Back projection (FBP) [105] and in a computationally efficient manner. ART relies on iterative reconstructions where the initial reconstruction starts with a computed back projection of the experimental images, similar to FBP. Next, the initial reconstruction is forward projected to simulate projection images. Ideally, the simulated projection images should be in agreement with the experimentally acquired projection images. However, in reality there is a discrepancy due to the limited number of projection angles and the noise in the acquired images. This discrepancy is also referred to as “projection distance” and is minimised iteratively until a minimum is reached [106]. ART can be discretized mathematically into a set of linear equations:

$$Ax = b \tag{59}$$

where, b is the set of projection images, A is a sparse matrix whose values A_{ij} represent the relative contribution of the voxel i to the j^{th} projection ray or the sinogram and x is the 1D array forming the unknown object. The easiest manner to determine x is to find the inverse of A. However, a typical tomography experiment consists of a limited number of projection images and the number of unknowns x outnumbers the number of known projections b by far. Thus, the system of linear equations in eq. 59 is underdetermined and the matrix A is ill-posed. Hence, instead of computing the inverse of the matrix A, the reconstruction is achieved by minimizing the norm of the projection distance, i.e. $\|Ax - b\|$ in an iterative manner.

ART sequentially updates the reconstruction by considering one projection image at a time [107,108]. A modified approach was proposed by Gilbert where, instead of sequentially updating the reconstruction, all the projection images are used to optimize the reconstruction at once. This modified approach is referred to as the SIRT (Simultaneous Iterative Reconstruction Technique) [109]. SIRT drastically improves the reconstruction in the presence of noisy projection images. For SIRT, the updated value of x_j (an element in x) in the k^{th} iteration is given by

$$x_j^k = x_j^{k-1} + \frac{\sum_i \left(\frac{A_{ij}(p_i - \sum_l A_{il}\, x_l^{k-1}}{\sum_l A_{il}} \right)}{\sum_i A_{ij}} \tag{60}$$

To date, SIRT remains the most popular reconstruction algorithms in the field of electron tomography in materials science and is also applied for 3D reconstructions throughout this thesis. Since algebraic reconstruction methods use a model based approach for the data and account for imperfections in the data, they provide better reconstruction in comparison to analytical methods, especially given the limited number of tilt or projection images. Even though ART and SIRT are computationally heavy in terms of processing time, the workload is partly compensated with the emergence of GPUs (graphical processing unit) and parallel computing, which have enabled efficient implementation of the necessary forward and back projections such that the computational load remains limited. The ASTRA toolbox [110–112] is one such open source libraries providing the necessary services. The ASTRA toolbox is a MATLAB and PYTHON toolbox of high performance GPU primitives for 3D and 2D tomography. It is GPU accelerated through CUDA (Compute Unified Device Architecture) and directly callable from MATLAB, enabling higher reconstruction speeds in comparison to the CPU counterparts.

5.2. Strain tomography of Si-Ge semiconductor material

So far the techniques investigating strain in semiconductor devices as discussed in previous chapters are measuring strain in 2D projection images and high resolution tomography potentially provides a novel approach to measure 3D strain in Si-Ge semiconductor materials. Even though high-resolution tomography has been a successful technique for 3D characterisation of metallic nanoparticles [92,93,103,113,114], it is a challenge for Si-Ge materials due to the FIB sample preparation and the lower atomic number of Si(Ge) (resulting in lower HAADF imaging contrast) in comparison to e.g Au or Ag. Therefore, we propose a number of steps for HR tomo experimentation on semiconductor materials like 1) A dedicated needle shaped sample preparation using FIB and a final low keV polishing in order to reduce the amorphous FIB side-wall damage (~25 nm) 2) Needle shaped symmetrically-thick samples (section 5.2.1) are mounted on the Fischione 2040 (Appendix 3) double tilt tomoholder. This is because the holder provides dual axis freedom (rotation and tilt) for alignment and tiliting along different cyrstallographic zone axes during tomographic tilt series acquisition 3) Molybdenum grids are used instead of conventional Cu TEM grids. This is because the clamping mechanism of the Fischione 2040 holder induces a slight bending of the grid when using conventional copper grids, resulting in precession motion instead of pure tilt during tomography tilt series acquisition. However, molybdenum grids proved to be much stiffer and resistant towards bending.

To investigate the ability to determine the 3D-strain distribution with electron tomography we used a blanket structure as a test sample (Appendix A2.1). A test/blanket structure is chosen for the experiment instead of the actual device (16 nm finFET), since a blanket structure is exhibited to be homogeneously strained in the in-plane direction and dimensions exceeding upto 100 µm on the wafer. The increased size of the blanket makes it easier to prepare symmetrical needle FIB structure (~45 nm in diameter) and thus, such sample is an ideal candidate for the proof of concept experiment and is discussed in detail in section 5.2.1.

Figure 29 illustrates the workflow for high resolution tomography to acquire 3D reconstruction from a transmission electron microscope. The different steps will be discussed in more detail below.

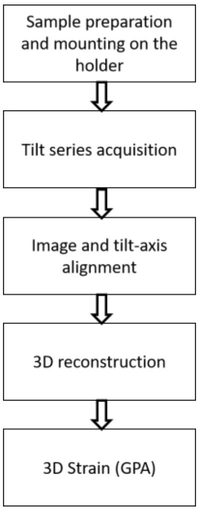

Figure 29 3D strain measurement work flow

5.2.1. TEM sample preparation

In situ lift out in a focussed ion beam/ scanning electron microscope (FIB/SEM) is a common method to prepare TEM samples from the bulk. In order to extract high resolution atomic features at various tilt angles, it is necessary to obtain relatively thin samples (< 50 nm). Needle shaped samples are prepared for the high resolution tomography experiment. Needle shaped samples are symmetric around the rotation axis and the thickness variation across different projection directions is ideally constant. This is in contrast to a conventional planar lamella or a square shaped lamella where the thickness increases rapidly as a function of tilt angle (impacting the high resolution features) and thus limiting the tilt range of the projection images resulting in increased missing-wedge [115]. Thus needle shaped samples enable higher tilt range in comparison to square or planar lamella where the tilt range is usually restricted to (< ±45°) and thus limiting the resolution degradation especially in the direction perpendicular to the tilt axis due to the missing-wedge.

Figure 30b and Figure 30c show the needle sample prepared from the blanket structure.

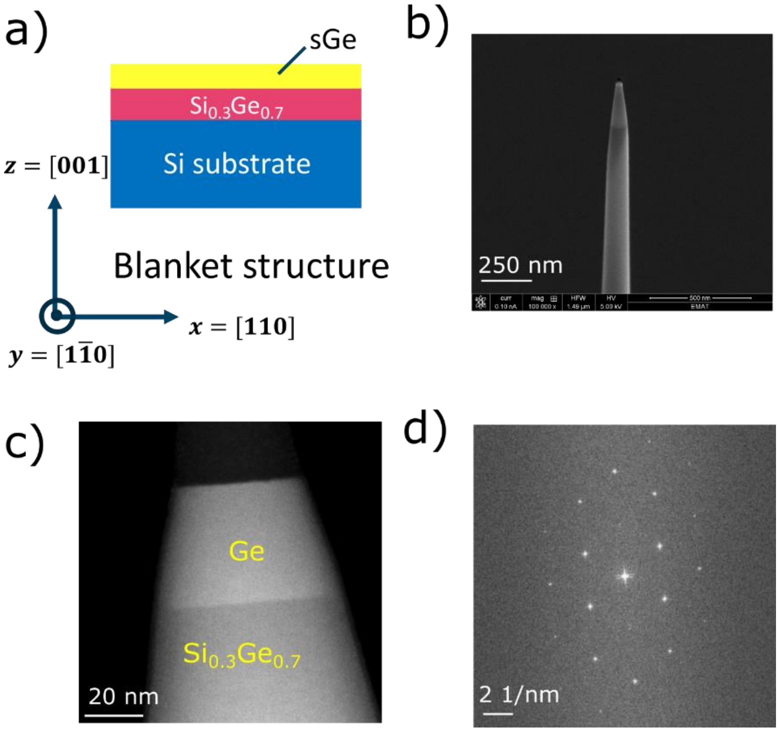

Figure 30 a) Overview of the blanket structure made up of layers of strained Ge (sGe), $Si_{0.3}Ge_{0.7}$ on Si substrate b) SEM image showing the overview of the needle sample c) TEM image near the tip taken along the [110] zone axis d) FFT of the needle sample image in c) indicating the presence of high resolution atomic features and the quality of the sample for high resolution imaging

FIB prepared needle samples are prone to ion beam induced damage creating a thick layer (~25 nm) of amorphous material surrounding the sample. This thick layer of amorphous damaged material is detrimental when trying to obtain high resolution features due to diffuse scattering from the amorphous region *[116]*. Hence, low keV polishing (accelerating voltage ~2 keV) at the end of the sample preparation was performed to reduce the amorphous damage layer to less than 5 nm *[117]*.

For this purpose, the ion beam is scanned in a ring shaped pattern, targeting the amorphous sidewalls of the needle. It is crucial to have a precise placement of the ring pattern on top of the needle for a symmetric reduction of the amorphous damage (Figure 31a). One relies on alignment markers or edges for such alignment for FIB instruments that lack spatial resolution especially at low keV acceleration voltage, and hence perfectly placing the ring pattern on top of the needle is challenging. This indirect approach for alignment could lack the precision for placement leading to non-symmetric removal of amorphous sidewall in some cases (Figure 31b).

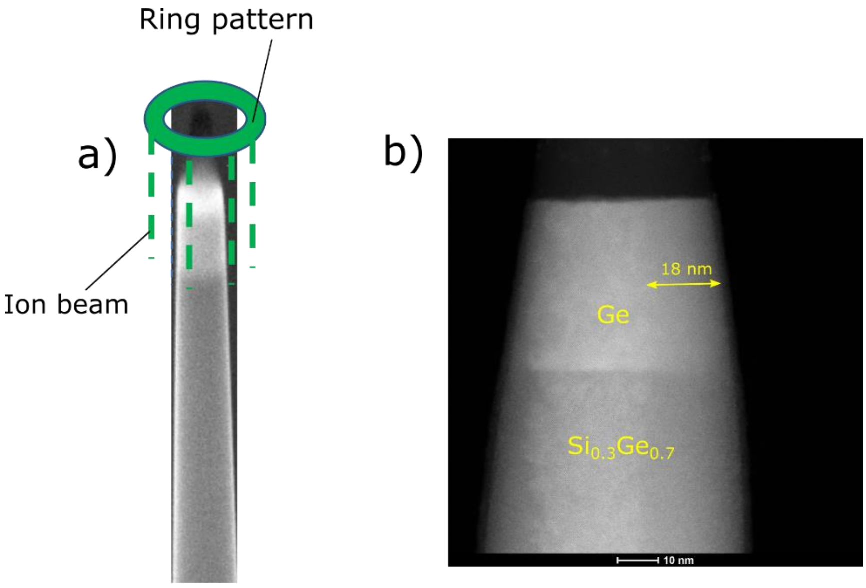

Figure 31 a) A low kV sidewall polishing is performed by scanning the ion beam in a ring pattern. The pattern needs to be placed precisely on top of the needle, otherwise it can result in non-symmetric removal of amorphous damage as shown in b) with the amorphous layer on the right side of the needle considerably thicker (~18 nm) than the on the left portion (~2 nm) and thus hampering the acquisition of high resolution images at various tilt angles.

5.2.2. Tilt series acquisition

HRSTEM images were taken at angles ranging from -70° to +70°. Although, it must be noted that needle shaped samples in principle, provide a complete 360° tilt range when using an on-axis tomography holder (Fischione 2050). However, the on-axis holder lacks the flexibility to align perfectly in zone axis, which is an essential requirement for high resolution imaging and tomography. Hence dual axis holder (Fischione 2040) is used for alignment purpose, however on the other hand the the tilt range in this holder is limited to ±70°. The acceleration voltage was set to 300 kV for maximum resolution. Since the total acquisition time for the tomography experiment can range from 1-2 hours (dose required for all tilt images and repositioning and refocussing the sample at every tilt angle), it is essential to work with lower beam currents and the overall dose to reduce beam damage. Hence, we selected a beam current of 35 pA (measured screen current).

Since HRSTEM imaging of the projection images are prone to scan distortions in the slow scan direction (chapter 4), series of fast acquisition images were taken which are later averaged and corrected for slow scan distortions and sample drift using rigid and non-rigid image registration methods [50]. Please note that the field of view is rather limited (~50 – 55 nm) due to the time required for large field of view imaging and the required number of pixels in the image. The pixel dwell time chosen for fast acquisitions was 0.4 µs and for a total of 4096 x 4096 pixel image, the resulting frame time was approximately 6.7 s.

5.2.3. Image and tilt axis alignment

Due to imperfections of the goniometer stage, relatively small nanoscale shifts of the specimen occur in the tilt series images. Hence, the recorded images need to be corrected for shifts and registered prior to the reconstruction. The most common procedure to estimate image shifts is by calculating the phase correlation between a reference image and a shifted image. Phase correlation between two images is calculated by taking the inverse Fourier transform of the normalised cross-spectrum [118]. It is in essence the same as cross correlation, but the cross correlation is computed on real space images while phase correlation is computed in the Fourier space resulting in a different computation path. The peak position of the phase correlation matrix is used to determine the relative shifts between the images (Figure 32c).

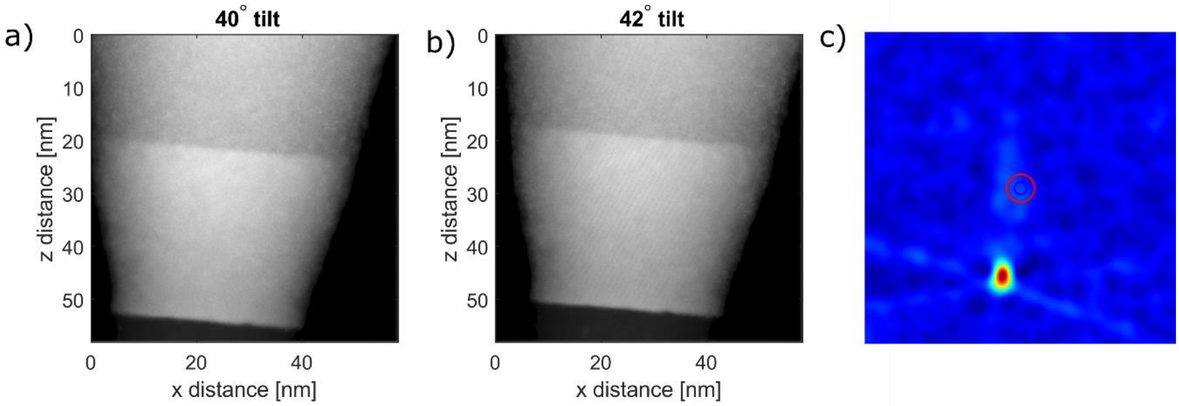

Figure 32 Tilt series images at a) 40° and b) 42°. Phase correlation between images a) and b) and the peak maximum indicates the relative shift between the two images. Ideally the peak should be centered for well aligned images.

Also for the tomographic reconstruction algorithm, the computational tilt axis needs to be aligned with the experimental one. Any possible misalignment could lead to streaking artefacts in the reconstruction resulting in lowering the reconstruction quality and further hampering the quantification.

5.3. Result

5.3.1. 3D reconstruction

Once all the tilt series images are aligned, they are used as input for the 3D reconstruction algorithm. In this thesis, we use the SIRT reconstruction algorithm. A combination of ASTRA toolbox with MATLAB scripting is used for alignment and reconstruction.

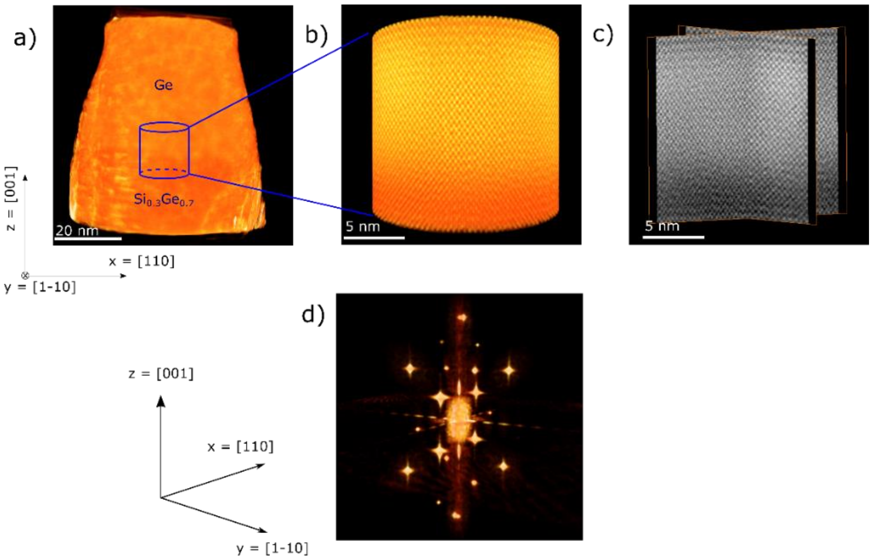

Figure 33 a) 3D reconstruction of the tip of the needle consisting of strained Ge and $Si_{0.3}Ge_{0.7}$ strain relaxed buffer (SRB) b) Enlarged area of the interface clearly illustrating the high resolution atomic features c) The 3D reconstruction gives access to the atomic arrangement inside the specimen, which is visualised through slices acquired through the reconstructed volume d) 3D Fourier transform of the reconstructed volume in b) where the individual reflections correspond to the lattice fringes in the reconstruction.

Figure 33a shows the tomographic reconstruction of the tip of the needle. The full structure is reconstructed at a maximum of 1024 x 1024 x 1024 pixel resolution. The size of the reconstruction depends directly on the RAM size and the GPU capability. The RAM size for the current analysis is 64 GB. As a first approximation, considering the space complexity of 3D GPA increasing linearly as a function of the 3D array size and for a full 4k resolution reconstruction, would require a RAM size of 4TB. Hence given the limited RAM size, here we attempt a 2k pixel resolution reconstruction and for this purpose a subregion near the Ge and $Si_{0.3}Ge_{0.7}$ interface (Figure 33b) is cropped along the z direction. Hence the field of view is downgraded while maintaining 2k pixel resolution and cropping along the z direction is allowed because it is parallel the rotation axis and perpendicular to all the projection directions. Since z is perpendicular to all the projection directions, cropping the projection images along this direction for a subsequent 3D reconstruction does not violate the projection requirement [119]. The 3D reconstruction provides information of the atomic arrangement inside the tomographic specimen (Figure 30b). and is used to calculate strain along the thickness or the projection direction, which is lacking in the 2D techniques investigated in the previous chapters.

5.3.2. 3D strain

Strain is calculated by extending the GPA analysis to three dimensions. The displacement field $\vec{u}$ along the three cartesian coordinates is

$$\begin{pmatrix} u_x \\ u_y \\ u_z \end{pmatrix} = -\frac{1}{2\pi} \begin{pmatrix} g_{1x} & g_{1y} & g_{1z} \\ g_{2x} & g_{2y} & g_{2z} \\ g_{3x} & g_{3y} & g_{3z} \end{pmatrix}^{-1} \begin{pmatrix} P_{g1} \\ P_{g2} \\ P_{g3} \end{pmatrix} \tag{61}$$

$(\overrightarrow{g_1}, \overrightarrow{g_2}, \overrightarrow{g_3})$ are the reciprocal vectors/reflections chosen in the Fourier space. The chosen reflections should not lie on a plane that is passing through the centre. Otherwise, it would make the matrix $G = \begin{pmatrix} g_{1x} & g_{1y} & g_{1z} \\ g_{2x} & g_{2y} & g_{2z} \\ g_{3x} & g_{3y} & g_{3z} \end{pmatrix}$ singular and its inversion to not exist. This condition is similar to choosing reflections that are non-collinear in the case of 2D GPA.

All the strain tensors can be calculated using the tomographic approach due to the three dimensional information of the crystal lattice. The strain tensors are calculated as:

$$\begin{bmatrix} e_{xx} & e_{xy} & e_{xz} \\ e_{yx} & e_{yy} & e_{yz} \\ e_{zz} & e_{zx} & e_{zz} \end{bmatrix} = -\frac{1}{2\pi} \begin{pmatrix} a_{1x} & a_{2x} & a_{3x} \\ a_{1y} & a_{2y} & a_{3y} \\ a_{1z} & a_{2z} & a_{3z} \end{pmatrix} \begin{pmatrix} \partial P_1/\partial x & \partial P_1/\partial y & \partial P_1/\partial z \\ \partial P_2/\partial x & \partial P_2/\partial y & \partial P_2/\partial z \\ \partial P_3/\partial x & \partial P_3/\partial y & \partial P_3/\partial z \end{pmatrix} \tag{62}$$

where, $(\overrightarrow{a_1}, \overrightarrow{a_2}, \overrightarrow{a_3})$ are the three lattice vectors in the real space which have a reciprocal relation to $(\overrightarrow{g_1}, \overrightarrow{g_2}, \overrightarrow{g_3})$. (P_1, P_2, P_3) are the geometric phases associated with the selected reflections in the Fourier space.

Figure 34, shows the strain map obtained by 3D GPA applied to the reconstructed cylindrical volume of the blanket structure in Figure 33b. The x, y and z directions are chosen such that they are parallel to $[110]$, $[1\bar{1}0]$ and $[001]$. The xy directions form the in-plane directions and z is along the axis of the cylinder or more specifically the growth direction.

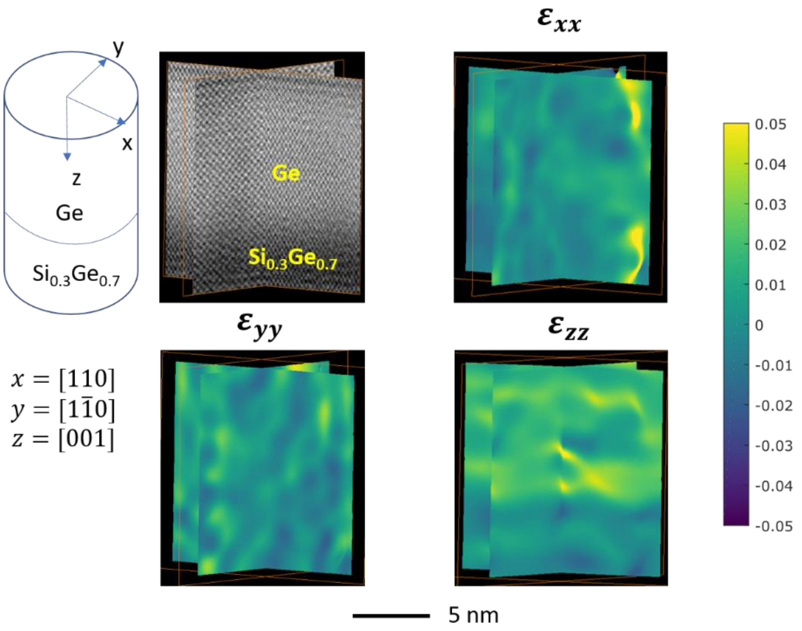

Figure 34 Normal strain along the x,y,z direction of the cylindrical reconstructed 3D volume near the Ge and $Si_{0.3}Ge_{0.7}$. Qualitatively we see the strain/lattice mismatch along the x and y inplane directions to be negligible. This means that the Ge layer is conforming with the lattice parameter of $Si_{0.3}Ge_{0.7}$ in the xy directions due to epitaxial confinement. A tensile strain is observed in the vertical z direction due to poisson effect.

we quantify the strain in the Ge channel with respect to bulk Ge and is tabulated in Table 4. The measured lattice mismatch between Ge and $Si_{0.3}Ge_{0.7}$ is used to calculate the strain in the Ge channel. The procedure is explained in detail in Appendix 5.

By analysing the strain values, we notice that the Ge is compressively strained in the in-plane directions, since the lattice parameter of Ge is larger than that of $Si_{0.3}Ge_{0.7}$ and due to epitaxial growth the Ge layer is expected to conform with respect to $Si_{0.3}Ge_{0.7}$ SRB. Due to the compression in the in-plane directions, tensile strain is observed in the vertical direction due to the Poisson effect.

Table 4 Strain comparison in the Ge layer of the blanket structure. The values quoted are the average strain values in the Ge region. The strain values for HR tomography is calculated after averaging the strain values in the 3D strain volume along the projection direction [110]. This step is to opted for comparison with the diffraction techniques that are operating on the diffraction patterns obtained along the [110] projection direction. The error values are the standard deviations in the measured strain values in the Ge region.

Technique	ε_{xx}	ε_{yy}	ε_{zz}
Nano-beam electron diffraction	$(-10.9 \pm 0.7) \times 10^{-3}$	$(-9 \pm 0.9) \times 10^{-3}$	$(3.3 \pm 0.6) \times 10^{-3}$
Bessel diffraction	$(-11 \pm 1) \times 10^{-3}$	$(-10 \pm 1) \times 10^{-3}$	$(3 \pm 1) \times 10^{-3}$
High-resolution tomography	$(-8 \pm 4) \times 10^{-3}$	$(-6 \pm 4) \times 10^{-3}$	$(5 \pm 4) \times 10^{-3}$

In order to directly compare with the existing diffraction techniques such as NBED and the Bessel diffraction that are operating on a projection scheme, strain measured from the high-resolution tomography is also calculated in projection. We opt this procedure by averaging the 3D strain from the reconstruction volume (Figure 34) along a particular projection axis or zone axis i.e., in this case the [110] zone axis. Please note that the strain variations observed in Figure 34 is significantly higher (~0.02 to 0.05) than the quoted standard deviation values in Table 4 for HR tomography. This is because the strain is averaged along the [110] projection in order to compare with the projection techniques (NBED/Bessel) and this can explain the discrepancy in standard deviation. Even though qualitatively the techniques match in terms of directions of strain, quantitatively, we observe a discrepancy between the measured average strain values.

The lower strain values in the ε_{xx} and ε_{yy} for HR tomography could possibly be related to the sample relaxation in the needle sample due to the reduced thickness of the sample ranging from 40 – 50 nm. The measurements for NBED and Bessel diffraction on the other hand, are performed on two perpendicular cross-section and long-section lamellae. The ε_{xx} and ε_{yy} are along the width of the lamellae (around 1-2 µm) and hence smaller relaxation effects are believed to occur. However, ε_{zz} in the case of NBED and Bessel diffraction is affected indirectly due to the relaxation through the thickness/ projection direction of the lamellae, which is impossible to measure for these techniques. On the other hand, the ε_{zz} for HR tomography is influenced by the sample relaxation in both the x and y directions and hence can explain the difference with respect to diffraction techniques. Therefore, a direct comparison would not be feasible without considering the differences in the thickness of the samples and the associated relaxation effects. This would require further relaxation analysis using Finite-element methods [120] and will not be discussed in this thesis. Moreover, future investigations should be performed in order quantify the experimental accuracy of the HR tomography technique through measurement on reference samples with known values of lattice mismatch for example, bulk Ge grown on a Si substrate. The strained samples on the other hand undergo relaxation and can influence the measurement of true bulk strain, but measuring accuracy on the unstrained system Ge on top of Si provides a ground truth for evaluating performance of the technique independent of the relaxation effect.

5.4. Conclusion

In this chapter, we explain the principles and the workflow for data acquisition and reconstruction for high-resolution tomography. We establish the proof concept of acquiring 3D reconstruction on the Si-Ge semiconductor samples and the subsequent 3D strain analysis, thus allowing the measurement of all the strain tensors from a single sample leading to visualization of strain through the thickness/projection direction of the sample. There is discrepancy of the quantitative measured strain values from high-resolution tomography with respect to diffraction techniques, even though they agree qualitatively in terms of the strain directions. Potential mechansims for these discrepancies are associated with strain relaxation in symmetrically thinned (~45 nm) needle shaped TEM samples. In general, high-resolution tomography is a promising technique to measure and characterise 3D strain in samples that are already small and do not require FIB preparation for example Au/Ag nanocrystals. In those samples, the strain state is the actual strain state of interest, including the relaxation effect. The cropping approach followed here due to limited RAM size for test/blanket structures may be problematic when analysing real devices where cropping is not an option, and hence one requires a higher RAM size (~512 GB for 2k resolution) or advanced approaches like big-data analytics [121]. With the future advancements in the mechanism of sample holders, providing higher degrees of freedom including all three aspects: 1) dual axis tilt with 2) in-plane rotation along with 3) the possibility to acquire a full 360° tilt range proves to be very robust against missing-wedge. These advancements can unlock the full potential of the technique and although strain relaxation is currently the inhibiting factor for routine strain measurements in semiconductor industry, using thicker FIB needle (~200 nm) samples can be one of the solutions to reduce the relaxation effect. However, in this case high resolution atomic features are also degraded at various tilt angles. On the other hand, 3D diffraction tomography can be performed using thicker samples and combining with 4D STEM (involving nano-probe mode like NBED) and reconstructing nanoscale 3D diffraction pattern at every voxel is an interesting arena to explore in the future.

Contributions:

My contributions for this chapter are experimentatal design and experimentation, extending the implementation of GPA to three dimensions and strain analysis. The needle shaped TEM samples were prepared by Stijn Van den broeck, EMAT. The 3D reconstructions are made using MATLAB software package developed by Dr. Ivan Pedro Lobato Hoyos. The chapter also benefitted from experimental design contributions from Prof.Dr. Thomas Altantzis and Dr. Thais Milagres de Oliveira, and review from Prof.Dr. Sara Bals, Prof.Dr. Johan Verbeeck and Prof.Dr. Wilfried Vandervorst.

Chapter 6: Raman strain measurement

This chapter contains large excerpts from the accepted paper for publication: V. Prabhakara, T. Nuytten, H. Bender, W. Vandervorst, S. bals and J. Verbeeck, “Linearized radially polarised light for improved precision in strain measurements using micro-Raman spectroscopy” [Optics Express https://doi.org/10.1364/OE.434726]

[First author contributions include design of radially polarised light setup and experimentation, strain analysis, numerical simulation and writing the manuscript, T.N. has contributed to the strain analysis, design of radially polarised light setup and manuscript review. The rest of the authors have contributed to the evaluation and review of the manuscript]

Raman spectroscopy is a non-invasive measurement technique with high sensitivity to mechanical stress and does not require any special sample preparation procedures in comparison to characterization involving TEM techniques as discussed in the previous chapters. Thus, it is attractive for inline strain measurement in the semiconductor industry. At present, Raman strain measurements are routinely carried out on semiconductor devices as it is cost-effective, fast and non-destructive. In this chapter, we begin by providing the theoretical basis for Raman stress – strain measurement. In the next section, we explore the different polarisation geometries of the laser light in the Raman setup and show how this degree of freedom provides flexibility in the selectivity of the method. For this purpose we investigate linear, radial and the combination resulting in linearised radial polarization as these may provide different electric field distributions crucial for exciting the longitudinal optic (LO) and transverse optic (TO) phonons which are crucial for strain analysis. In the next section, we will discuss the experimental results of strain measurement as applied on a test structure and 16 nm finFET arrays. We also highlight the benefits of the linearised radially polarised light in terms of improved precision in comparison to the conventional linear polarised incoming light.

6.1. Raman stress – strain measurement

Raman spectroscopy is a non-destructive tool to characterize a variety of material parameters like for instance mechanical stress in crystalline materials. Raman scattering is an inelastic process where the incident photons (1 in 10 million) scatter at a different energy/frequency in comparison to the incident photon. The difference in the energy levels is called the Raman shift and depends on the vibrational energy levels unique to the material under study. Moreover, Raman spectroscopy also provides an indirect way to measure strain in semiconductor materials. Raman strain measurement relies on identifying the shift in the observed phonon peaks (of strained and unstrained materials) which can be associated with the stress present in the material as the amount of shift is directly dependent on the phonon deformation potentials [122,123].

The polarisation dependence of light for Raman spectroscopy is described below. The Raman scattering efficiency I is proportional to the incident light polarisation and the outgoing light polarisation and is given by [124,125]

$$I = C \sum_j \left| e_{out}^T \boldsymbol{R_j} e_{in} \right|^2 \tag{63}$$

where,C is a constant and **R**$_j$ is the Raman tensor for the j^{th} phonon, e_{out} and e_{in} are the outgoing and incoming polarisation vectors. The subscript T corresponds to the transposed vector. The Raman tensors are obtained from group theoretical considerations which are used to calculate the polarization selection rules [126]. In zinc blende-type or diamond-type point group semiconductors (silicon, germanium), the Raman tensors in the cartesian coordinate system x = [100], y = [010] and z = [001] are given by

$$\boldsymbol{R_x} = \begin{bmatrix} 0 & 0 & 0 \\ 0 & 0 & d \\ 0 & d & 0 \end{bmatrix}, \boldsymbol{R_y} = \begin{bmatrix} 0 & 0 & d \\ 0 & 0 & 0 \\ d & 0 & 0 \end{bmatrix}, \boldsymbol{R_z} = \begin{bmatrix} 0 & d & 0 \\ d & 0 & 0 \\ 0 & 0 & 0 \end{bmatrix} \tag{64}$$

Where d indicates the non-zero Raman polarizability elements and can be different for LO and TO phonons, i.e. $d_{TO} \neq d_{LO}$ [127]. For the backscattering configuration with z being the light propagation direction, the longitudinal optical (LO) phonons vibrate in the z direction and the transverse optic (TO) phonons vibrate in the x and y directions [127]. Hence, there is one LO and two TO phonons in the Si and Ge crystals resulting in a total of three active Raman peaks at k = 0 (central point of the Brillouin zone). The three phonon modes are degenerate in the bulk crystal due to the crystal symmetry but the introduction of strain alters the symmetry and lifts this degeneracy [73]. Stress measurements using Raman spectroscopy are performed by measuring the shift of the center of these phonon peaks in comparison to their location in the unstrained material. The relation between the shift in the phonon peaks $\varDelta\omega_{LO-TO}$ relative to the position in the degenerate bulk and the normal stresses $\sigma_{x,y}$ is given by [35]

$$\varDelta\omega_{LO} = \frac{1}{2\omega_0}\left(p\boldsymbol{S_{12}} + q(\boldsymbol{S_{11}} + \boldsymbol{S_{12}})\right)\left(\sigma_x + \sigma_y\right) \tag{65}$$

$$\begin{aligned}\Delta\omega_{TO_1} = \frac{1}{2\omega_0}\Bigg[&\left(\frac{1}{2}(\boldsymbol{S_{11}} + \boldsymbol{S_{12}})(p+q) + q\boldsymbol{S_{12}} + \frac{r}{2}\boldsymbol{S_{44}}\right)\sigma_x \\ &+ \left(\frac{1}{2}(\boldsymbol{S_{11}} + \boldsymbol{S_{12}})(p+q) + q\boldsymbol{S_{12}} - \frac{r}{2}\boldsymbol{S_{44}}\right)\sigma_y\Bigg]\end{aligned} \tag{66}$$

$$\begin{aligned}\Delta\omega_{TO_2} = \frac{1}{2\omega_0}\Bigg[&\left(\frac{1}{2}(\boldsymbol{S_{11}} + \boldsymbol{S_{12}})(p+q) + q\boldsymbol{S_{12}} - \frac{r}{2}\boldsymbol{S_{44}}\right)\sigma_x \\ &+ \left(\frac{1}{2}(\boldsymbol{S_{11}} + \boldsymbol{S_{12}})(p+q) + q\boldsymbol{S_{12}} + \frac{r}{2}\boldsymbol{S_{44}}\right)\sigma_y\Bigg]\end{aligned} \tag{67}$$

Where, **S$_{ij}$** are the components of the compliance matrix, p,q and r are the phonon deformation potentials, and ω_0 is the stress-free value for the Raman shift. The measured stress values are used to calculate the strain using Hooke's law of elasticity, within the linear elastic regime (as applicable for Si and Ge in typical semiconductor applications) [41].

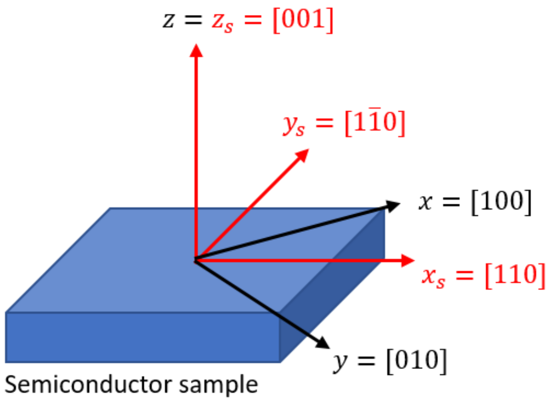

Figure 35 Schematic illustration of the orientation of a typical semiconductor sample i.e. oriented along the x_s, y_s and z_s with respect to the cartesian coordinate system (xyz).

The semiconductor devices in our study are oriented in the $x_s = [110]$, $y_s = [1\bar{1}0]$ and $z_s = [001]$ crystal coordinate system (Figure 35) and it is of interest to consider the crystal coordinate system instead of the Cartesian, as it then becomes straightforward to interpret the calculated stress values directly in the relevant crystal coordinate system. From eq.63-64, we can derive the polarisation requirements for the incoming and the outgoing light in exciting particular phonon modes (Table 5). Since the Raman scattering experiment is done in the backscattering configuration, we consider $z_s = [001]$ as the light propagation direction. x_s, y_s, z_s are represented as x, y and z for simplicity. The experimental configuration is denoted in the Porto notation (excitation direction (excitation polarization analyzer direction) Raman scattered light direction). For example, the notation $z(xy)\bar{z}$ denotes that z and $\bar{z}$ are the directions of propagation of the exciting (incoming) and Raman scattered (outgoing) light, and x and y are the polarization directions of the exciting and Raman scattered light respectively.

Table 5 Raman phonon selectivity for different experimental configurations considering x = 110, y = -110 and z = [001]

Experimental configuration (Porto notation)	LO	TO$_1$	TO$_2$
$z(xx)\bar{z}$	d^2	0	0
$z(yy)\bar{z}$	d^2	0	0
$z(zx)\bar{z}$	0	0	d^2
$z(zy)\bar{z}$	0	d^2	0
$z(zz)\bar{z}$	0	0	0

$z(xy)\bar{z}$	0	0	0
$z(yx)\bar{z}$	0	0	0

The identification of TO and LO phonons is crucial for measuring the stresses as given by eqs. 65–67 and it is important to assess the phonon selectivity for the experimental backscattering configuration. Considering the phonon selectivity for different experimental configurations (Table 5), the light polarization is transverse and restricted to the x and the y axis and hence in the backscattering configuration, one can excite only LO phonons. The introduction of high numerical aperture (NA) objective lenses and oil immersion lenses provides a high convergence angle and increases the z component of the electric field near the focal plane and thus enables the excitation of the TO phonons that are traditionally forbidden for the backscattering configuration [74]. Now, considering the backscattering experimental mode with the oil immersion lens (high numerical aperture(NA) of 1.4) and linearly x-polarised light (polarised in x direction), the incoming light will have primarily the x- and some y- and z-polarised components due to the depolarisation effect [128,129]. So, to excite the TO phonons (TO mode), the analyzer is set to the y-direction (perpendicular to the incoming light polarization) and with a high NA aperture, we encounter $z(xy)\bar{z}$, $z(zy)\bar{z}$ and $z(yy)\bar{z}$ scenarios. The $z(xy)\bar{z}$ configuration is Raman inactive, while $z(zy)\bar{z}$ excites the TO_1 phonon. The small y component present in highly convergent incident laser light results in $z(yy)\bar{z}$ and in combination with non-perfect analyzer optics gives rise to a noticeable excitation of the LO phonon. Thus, in practice, when we experimentally attempt to measure the TO mode, we excite both the TO_1 and LO phonons. In the LO mode configuration, the analyser is set parallel to the x-direction i.e. parallel to the polarisation of the incoming light source. In this scenario, we encounter $z(xx)\bar{z}$, $z(yx)\bar{z}$ and $z(zx)\bar{z}$ given the high NA oil immersion lens. The $z(yx)\bar{z}$ configuration is Raman inactive. The TO_2 which is excited by $z(zx)\bar{z}$ is concealed by the dominant LO component from $z(xx)\bar{z}$ due to a highly intense x-component of incoming light (further details are provided in the electric field simulation section 6.3). Hence, with backscattering Raman spectroscopy, we can in principle excite one LO phonon and one TO phonon allowing the measurement of biaxial in-plane stresses in the Si and Ge semiconductor materials as will be discussed below. However, as we will see, this setup suffers from low selectivity as LO and TO contributions can not be fully separated from each other.

6.2. The deconvolution problem

Figure 36 illustrates the experimental Raman spectra taken on a blanket structure (Appendix A2.1) consisting of a thick $Si_{0.3}Ge_{0.7}$ layer grown on a Si substrate (Figure 36 inset). Notice that the TO and LO components of the Ge peak in the TO mode overlap each other strongly leading to the broad Ge peak. Though one can use the prior knowledge from the LO mode spectrum (that predominantly consists of the

LO phonon) to estimate the peak shape of the LO-contribution, separating LO/TO unambiguously remains very difficult. The required process to disentangle these peaks would become more reliable if one could vary the intensity of the TO component more (relative to the LO component) in the overlapping spectrum.

To achieve this, we explore the use of radially polarised light. Radially polarised light has a strong and centrally focused longitudinal component of light compared to linearly polarised light. This boosts the intensity of the TO peaks in the Raman spectra, relative to the LO peak, which would allow us to separate LO and TO in a more reliable way thus providing insight into the detailed biaxial stress distributions. The radial polarisation in this experiment is achieved by using an S-waveplate (manufactured by Wophotonics, Lithuania) which directly converts the incoming linearly polarised light to radially polarised light and is positioned in between the attenuator and the objective lens (Appendix A1.2).

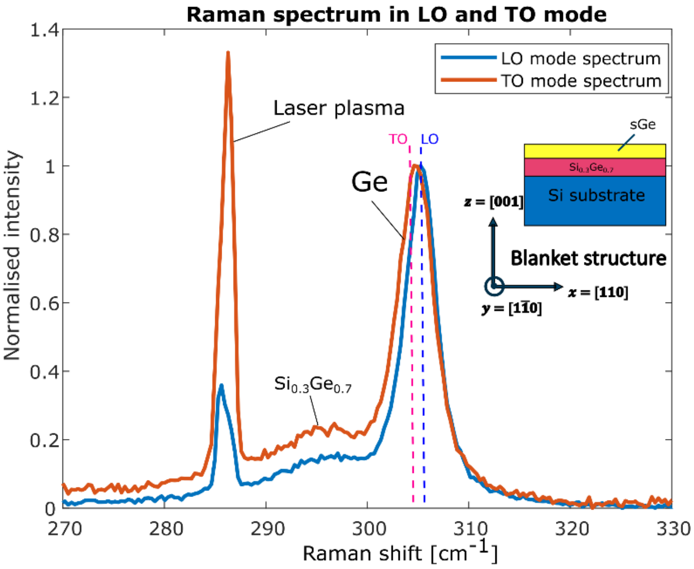

Figure 36 Experimental Raman spectra on the SiGe blanket structure consisting of the strained Ge region. The spectra are normalized in intensity with respect to the Ge peak. Note the broad Ge peak in the TO mode clearly indicating the presence of both TO and LO peaks. The dotted lines indicate the expected theoretical peak *positions of TO and LO in the strained Ge showing the difficulty to resolve them as separate peaks in the experimental setup.*

In the next section, we will compare the effect of using the different Raman excitation source geometries (i.e. linearly, radially and linearised radially polarised light) through numerical simulations with the purpose to investigate their potential effect on enhanced selectivity for the detection of TO phonons.

6.3. Numerical simulation of the electric field components

6.3.1. Linearly and radially polarised light

Radially polarised light has a strong and centrally focussed longitudinal component of light compared to linearly polarised light and has been a topic of interest in the last few decades [130–135]. The strong centrally focused longitudinal component of light boosts the intensity of the TO peaks in the Raman spectra in the TO mode, which are usually accompanied by the LO peak. The electric field distribution (field strength) for the radially polarised light is given by [136]:

$$Ix(\rho, z) = -\frac{iA}{\pi}\int_0^{2\pi}\int_0^{\alpha} cos^{1/2}\theta\ sin\theta\ cos\theta\ cos(\varphi) I_o(\theta) e^{ik(zcos\theta+\rho sin\theta cos(\varphi-\varphi_s)} d\varphi d\theta \quad (68)$$

$$Iy(\rho, z) = -\frac{iA}{\pi}\int_0^{2\pi}\int_0^{\alpha} cos^{1/2}\theta\ sin\theta\ cos\theta\ sin(\varphi) I_o(\theta) e^{ik(zcos\theta+\rho sin\theta cos(\varphi-\varphi_s)} d\varphi d\theta \quad (69)$$

$$Ir(\rho, z) = -\frac{iA}{\pi}\int_0^{2\pi}\int_0^{\alpha} cos^{1/2}\theta\ sin\theta\ cos\theta\ cos(\varphi - \varphi_s) I_o(\theta) e^{ik(zcos\theta+\rho sin\theta cos(\varphi-\varphi_s)} d\varphi d\theta \quad (70)$$

$$Iz(\rho, z) = -\frac{iA}{\pi}\int_0^{2\pi}\int_0^{\alpha} cos^{1/2}\theta\ sin^2\theta I_o(\theta)\ e^{ik(zcos\theta+\rho sin\theta cos(\varphi-\varphi_s)} d\varphi d\theta \quad (71)$$

where, A is a constant that is dependent on the incoming laser beam intensity. Ix, y are the electric field transverse components, *Ir* and *Iz* are the radial ($r = \sqrt{x^2 + y^2}$) and longitudinal components, ρ, φ_s and z are the radial, azimuthal and vertical cylindrical coordinates with respect to the origin in the focal plane; x,y, and z are the Cartesian coordinates in the focal plane, θ is the angle a sub-ray makes with the optical axis and θ is integrated from 0 to the convergence angle α(acceptance angle), φ is the azimuth angle subtended by the sub-ray onto the focal plane and is integrated from 0 to 2π (Figure 37).

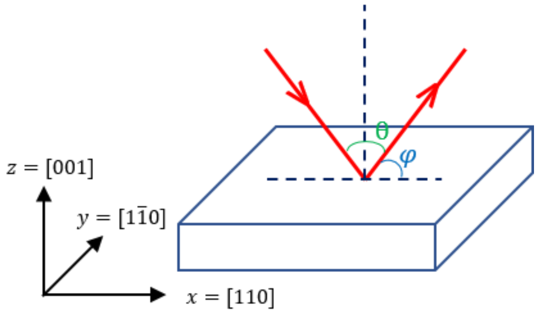

Figure 37 Schematic illustration of the geometry of light interaction on the focal plane

$I_o(\theta)$ is the Bessel-Gauss apodization function as described in [137,138]:

$$I_0(\theta) \ = exp\left[-\beta^2\left(\frac{sin\theta}{sin\alpha}\right)^2 J_1\left(2\beta\frac{sin\theta}{sin\alpha}\right)\right] \tag{72}$$

Where β is the ratio of pupil radius and beam waist. Likewise, the electric field distribution for the linearly polarised light in the cartesian coordinate system has been extensively discussed in [139]. The intensity distribution of electric field components for the linearly polarised light considering the same notations as for the radially polarised light is given by

$$\begin{gathered} Ix = \ -iA[I_0 + I_2cos(2\varphi)] \\ Iy = \ -iAI_2sin(2\varphi) \\ Iz = \ -2AI_1cos(\varphi) \end{gathered} \tag{73}$$

The quantities In, with n = 0,1,2 are integrals of nth order Bessel function J_n of the first kind

$$I_0(\rho,z) = \int_0^\alpha cos^{1/2}\theta\ sin\theta(1+cos\theta)J_o(k\rho sin\theta)\ e^{ikzcos\theta}d\theta \tag{74}$$

$$I_1(\rho,z) = \int_0^\alpha cos^{1/2}\theta\ sin^2\theta J_1(k\rho sin\theta)\ e^{ikzcos\theta}d\theta \tag{75}$$

$$I_2(\rho,z) = \int_0^\alpha cos^{1/2}\theta\ sin\theta(1-cos\theta)J_2(k\rho sin\theta)\ e^{ikzcos\theta}d\theta \tag{76}$$

To gain insight into the electric field distributions for the specific case of our experiments, we performed numerical simulations using the parameters of our experimental setup i.e. the laser excitation wavelength of 633 nm, a convergence angle (equal to acceptance angle for the backscattered configuration) of 70°, a beam waist of 0.68 mm, a working distance of 0.13 mm, a numerical aperture of 1.4 (using an oil objective), a focal length of 0.129 mm and a pupil radius of 0.18 mm. The results of these calculations are summarised in Figure 38.

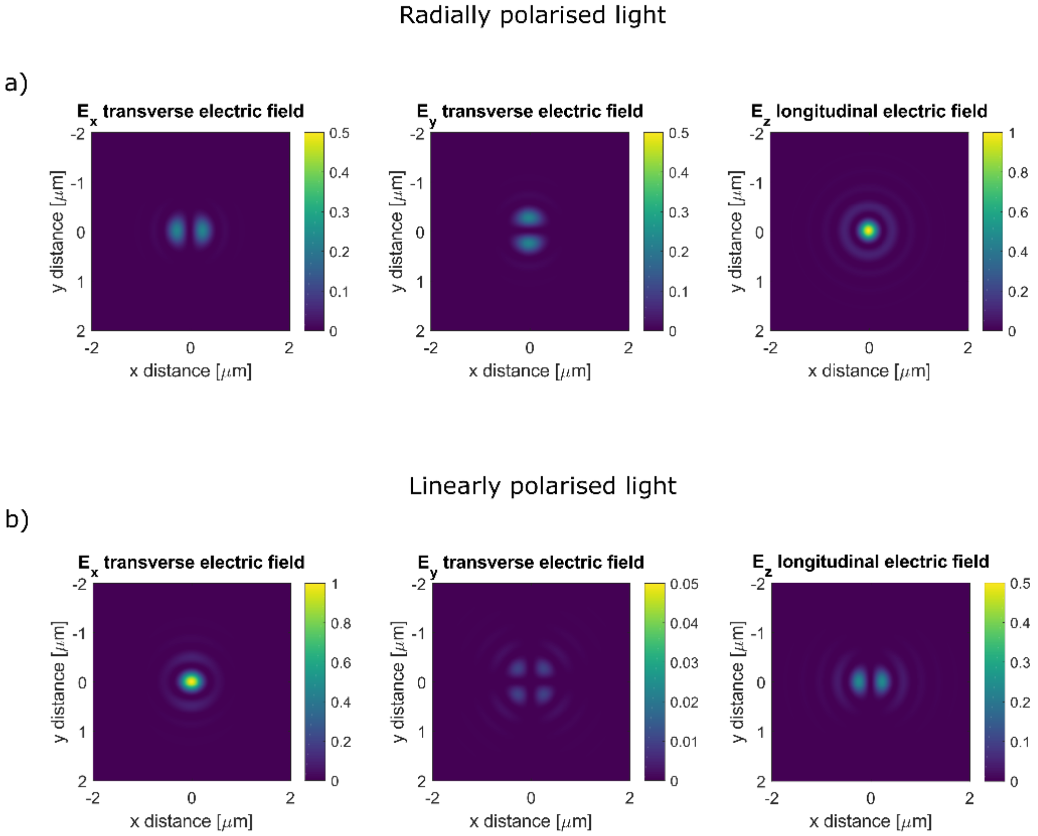

Figure 38 Normalized (with respect to incoming beam intensity) electric field intensity distribution of a) Radially and b) Linearly polarised light at the focal plane.

The units for the electric field are in Volt/m, but the absolute values depend on the laser power. Hence the normalised intensity with respect to the incoming beam intensity is shown for the purpose of electric field distribution visualisation, where the constant A in equations describing the electric field distribution in x, y, z is the normalisation factor with respect to the incoming beam intensity. Compared to the electric field distribution of the linearly polarised light, we can conclude that the radially polarised light has a strong centrally focused longitudinal component of light and the transverse x and y components form the two side lobes (Figure 38 a). Vice versa, the linearly polarised light has a strong centrally focused component in the direction of polarisation x and the y, z components are distributed away from the center (Figure 38 b). Similarly, the relative intensities of the electric field components are tabulated in Table 6. The intensity in general is calculated as the sum of the amplitude square of the electric field. The relative intensity of a component is calculated as the intensity of that particular component divided by the total intensity. It can clearly be seen from the table that for radially polarised light, the Ez component is twice as high in comparison to linearly polarised light. Since it is this component that is responsible for the excitation of the TO phonon in TO mode acquisition $[z(zy)\bar{z}]$, our calculations show that for our experimental setup, we can expect a higher TO phonon intensity in the TO mode.

Table 6 Relative intensity contributions of electric field components for linearly and radially polarised light at the focal plane

Polarization	E_x	E_y	E_z
Linear in x	0.67	0.02	0.31
Radial	0.195	0.195	0.61

Finally, the normalized intensity distribution of the Ex, Ey and Ez components is calculated as a function of the radial distance from the centre, by radial integration and normalisation to the total intensity in the distribution. This gives the normalised intensity distribution as a function of the diametric distance (Figure 39). The spatial resolution is calculated as the diameter of the disc that contains 68.5% of the total intensity (or one standard deviation from the center). The results are summarised in Table 7 and from here it can be concluded that the radially polarised light provides a higher spatial resolution for both the longitudinal and transverse components and hence provides a tighter focus of the laser beam in the focal plane.

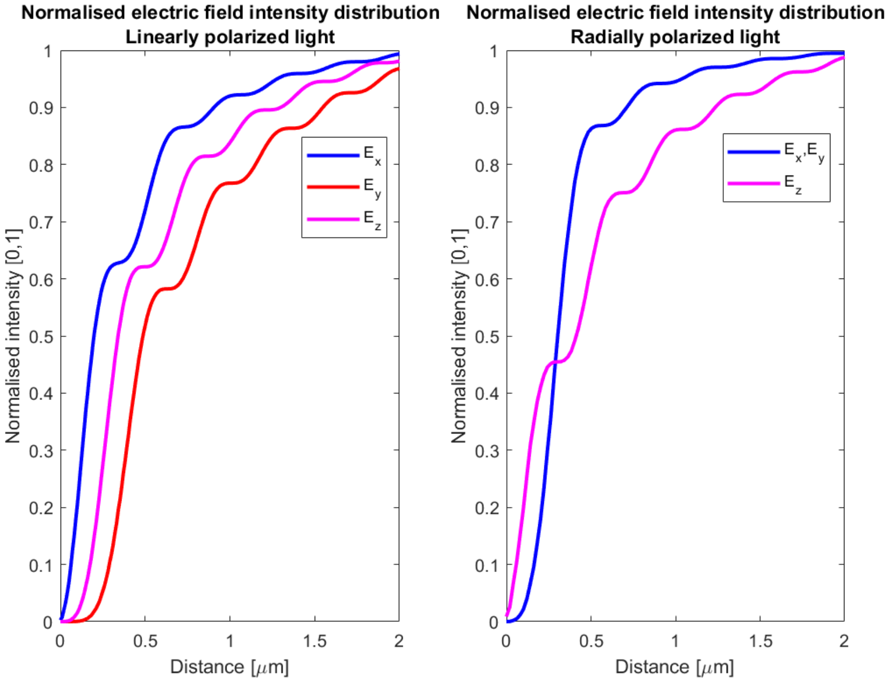

Figure 39 Normalised intensity distribution of electric field components on the focal plane. The spatial resolution is the diametric distance or the diameter of the disc within which 68.5% of the total intensity lies.

Table 7 Comparison of obtainable spatial resolution for linearly and radially polarised light. The spatial resolution is calculated as the diametric distance or the diameter of the disc which contains 68.5% of the total intensity

Polarization	Spatial resolution [nm]		
	E_x	E_y	E_z
Linear in x	455	818	728
Radial	364	364	545

We also calculate the relative intensities of the components as a function of the defocus distance (Figure 40). We notice a local enhancement of the longitudinal component of light close to the focal point (defocus = 0 µm) as expected for a high NA objective lens. The enhancement of the longitudinal component is very high in the case of radially polarised light in comparison to the linearly polarised light in line with the previous calculations. The Ex and Ey profiles remain identical for the radial setup.

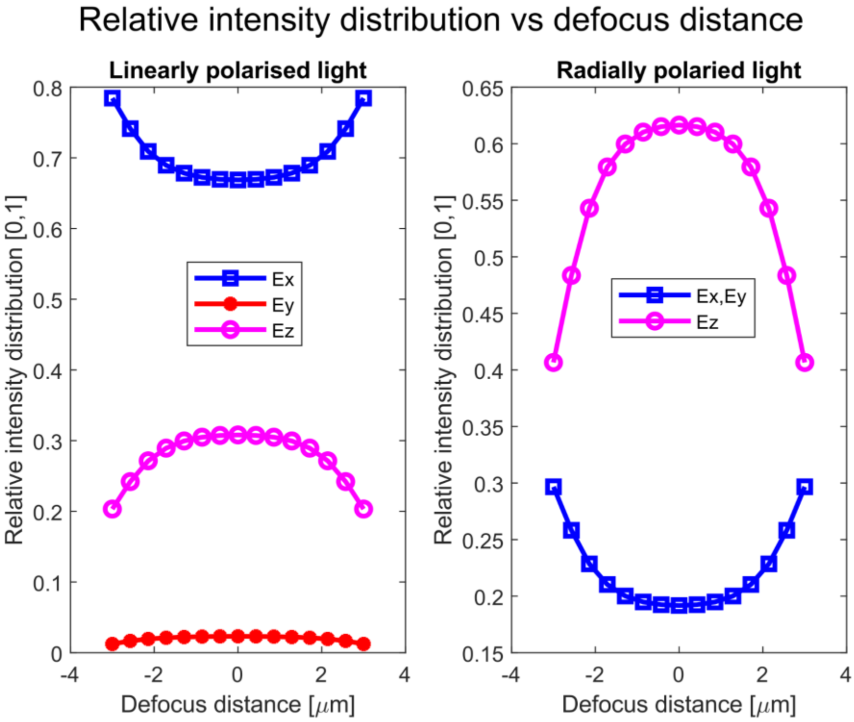

Figure 40 Relative intensity distribution of electric field components as a function of defocus [µm] (defocus zero being the exact focal distance) for linearly (in x) and radially polarised light.

Hence from Figure 40, it can be concluded that radially polarised light provides a strong longitudinal component of light E_z in the focal plane (defocus = 0) in comparison to the linearly polarised light. The E_z remains high within a tolerable range of ±1.5 µm from the focal plane and decreases drastically away from the focal plane. Since E_z is responsible for exciting the TO component, we can expect a higher TO phonon intensity in the TO mode within the defocus range of ±1.5 µm.

6.3.2. Linearised radially polarised light

Despite the reduction in the transverse components for the radially polarised light (as per the calculations in section 6.3.1), experimentally the TO phonon intensity appeared a lot weaker than the LO phonon in the TO mode (Figure 45 b) resulting in a higher ambiguity in the identification of the TO peak and highly unreliable stress measurements. The reason is speculated to be due to $d_{TO} \neq d_{LO}$. For the $z(zy)\bar{z}$ configuration that results in the TO_1 excitation (Table 5), the Ey component of the incoming radially polarised light needs to be suppressed further in order to reduce the undesired LO phonon signal in the TO mode. In that regard, we have used a linearised radially polarised setup [78] by placing a linear polariser after the radial polariser to further suppress the intensity of the Ey component of light (perpendicular to the transmission axis of the linear polariser) in the conventional radially polarised light at the focal plane. This helps to filter out or reduce the undesired component of light that is leading to LO phonon excitation while targeting the TO mode. We also calculate numerically the relative intensity distribution of the electric field components of the linearised radially polarised light to evaluate the degree of reduction in the Ey (with x being the linear-polariser transmission axis) and also the effect on the spatial resolution from this modified setup.

The transmittance T of a linear polariser is given as:

$$T(\varphi) = (T_1 - T_2)cos^2\varphi + T_2 \tag{77}$$

where, φ is the angle between the polarization of light and the transmission axis of the linear polariser, T_1 is the maximum transmittance value when the incoming light is parallel to the linear polariser transmission axis and T_2 is the minimum transmittance when the incoming light is perpendicular to the linear polariser transmission axis. Using eq.77 in eqs.68-71 results in the electric field distribution equations for the linearised radially polarised light:

$$Ix(\rho, z) = -\frac{iA}{\pi}\int_0^{2\pi}\int_0^{\alpha} T(\varphi)cos^{\frac{1}{2}}\theta\ sin\theta\ cos\theta\ \cos(\varphi) I_o(\theta)e^{ik(zcos\theta+\rho sin\theta cos(\varphi-\varphi_s))}d\varphi d\theta \tag{78}$$

$$Iy(\rho, z) = -\frac{iA}{\pi}\int_0^{2\pi}\int_0^{\alpha} T(\varphi)cos^{1/2}\theta\ sin\theta\ cos\theta\ sin(\varphi) I_o(\theta)e^{ik(zcos\theta+\rho sin\theta cos(\varphi-\varphi_s))}d\varphi d\theta \tag{79}$$

$$Ir(\rho,z) = -\frac{iA}{\pi}\int_0^{2\pi}\int_0^{\alpha} T(\varphi)cos^{1/2}\theta\ sin\theta\ cos\theta\ cos(\varphi - \varphi_s)I_o(\theta)e^{ik(zcos\theta+\rho sin\theta cos(\varphi-\varphi_s)}d\varphi d\theta \tag{80}$$

$$Iz(\rho,z) = -\frac{iA}{\pi}\int_0^{2\pi}\int_0^{\alpha} T(\varphi)cos^{1/2}\theta\ sin^2\theta I_o(\theta)\ e^{ik(zcos\theta+\rho sin\theta cos(\varphi-\varphi_s)}d\varphi d\theta \tag{81}$$

To understand the benefits linearisation brings to the conventional radially polarised light setup we look at the electric field distributions from both the radially polarised and the linearised radially polarised light setup. Figure 41 shows the normalised electric field distribution of the radial component E$_r$ ($E_r = \sqrt{E_x^2 + E_y^2}$) at the focal plane for both the radially polarised light and the linearised radially polarised light (with transmission axis of the linear polariser parallel to x - axis). The simulation parameters for the linear polariser include $T_1 = 0.83$ and extinction ratio $\rho_P = \frac{T_1}{T_2} = 800$ (in accordance with the specification for visible wire-grid polarisers). Analysing Figure 41 shows that the radial component of the radially polarised light is radially symmetric and possesses a doughnut-shaped distribution. Linearised radially polarised light on the other hand has a skewed distribution where a higher intensity is concentrated in the direction of the transmission axis of the linear polariser (x-axis). We will show later in this section how this configuration affects the relative electric field distributions favoring the reduction in the Ey component.

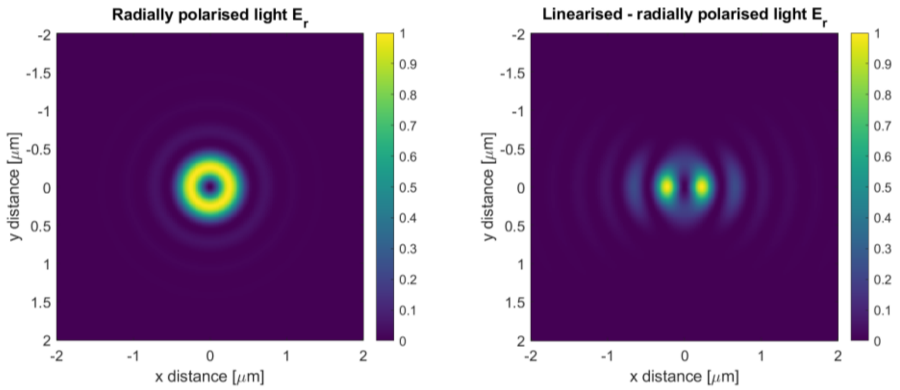

Figure 41 Normalized intensity distribution of the radial electric field E$_r$ for a) radially polarised light and b) linearised radially polarised light. The linear polariser transmission axis is parallel to the x axis.

Now, the electric field distributions of the x,y,z cartesian coordinates are shown in Figure 41. Here again, we observe a centrally focused longitudinal component in comparison to the transverse components. The transverse components form the side lobes with field intensities concentrated away from the center.

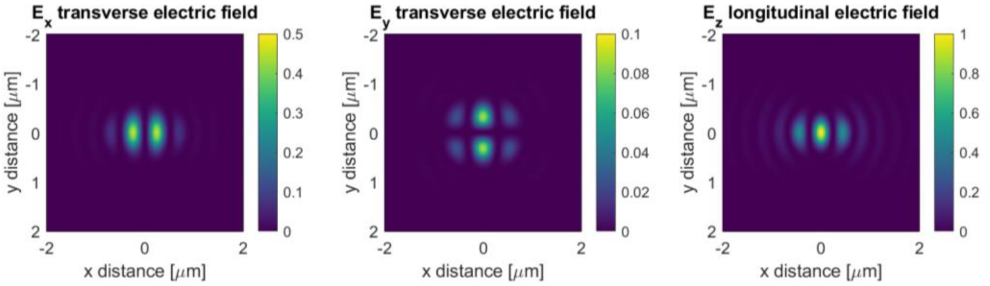

Figure 42 Normalised electric field distribution of the linearised radially polarised light at the focal plane.

The interest lies in the relative intensity contributions of the three electric field components (Table 8) Ex, Ey and Ez. The Ey component is greatly suppressed in comparison to the Ey component for radially polarised light (refer Table 6). This is because of the introduction of the linear polariser whose transmission axis is parallel to the x-axis. The longitudinal component is still higher and comparable to the radially polarised light setup. The relative intensity in Ex is higher in linearised radially polarised light due to a higher transmission in the x-direction.

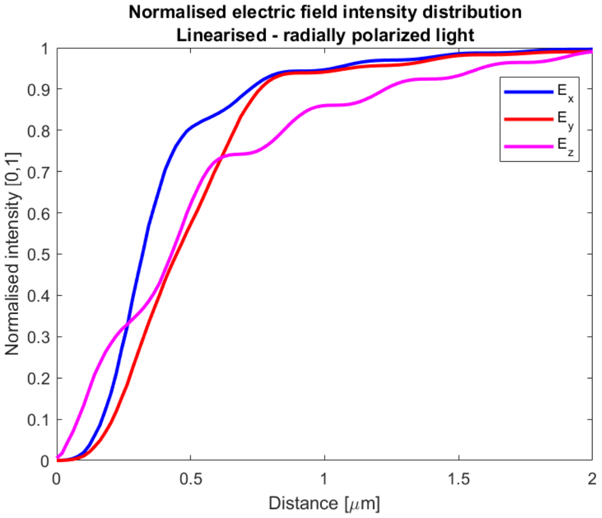

Figure 43 Normalised intensity distribution of electric field components of the linearised radially polarised light. The spatial resolution is the diametric distance within which 68.5% of the total intensity lies.

Table 8 Relative intensity and obtainable spatial resolution for linearised radially polarised light. The spatial resolution is calculated as the diametric distance which contains 68.5% of the total intensity.

Parameter	E_x	E_y	E_z
Relative intensity	0.33	0.06	0.61
Spatial resolution [nm]	394	576	545

The benefit of the linearised radially polarised light over the radially polarised light is the reduction in the Ey which is mainly responsible for the increased LO contribution in the TO mode ($z(zy)\bar{z}$). The Ex contribution, although higher than in the radially polarised light, is still half of the Ex contribution in the linearly polarised setup. This should lead to a reduction effect in the TO mode due to the transmission axis of the analyzer placed in the y - direction which has a very high extinction coefficient ($\rho_P > 800$). Thus, a higher TO/LO ratio is expected for the linearised radially polarised light for our experimental setup. The spatial resolution of the linearised radially polarised light is comparable to the radially polarised setup in the Ex and Ez and a higher spatial spread of the Ey component is seen with the introduction of the linear polariser whose transmission axis is set parallel to x-axis.

The relative intensity as a function of the defocus distance (Figure 44) for the linearised radially polarised light follows a similar trend as the radially polarised light for Ex and Ez, with a local enhancement of the longitudinal component Ez close to the focal plane (defocus = 0) with a tolerable defocus range ±1.5 µm. Ex is relatively higher in the linearised radially polarised light due to the transmission axis of the linear polariser being aligned parallel to the x-direction and consequently Ey is greatly suppressed in comparison to the radially polarised light and with this suppression we can expect a higher TO/LO ratio for the linearised radially polarised setup. In the next section, we will discuss the experimental results after applying all the three polarisation geometries (linear, radial and linearised radial) on the blanket/test structure and compare the stress measurements on the blanket and the 16 nm finFETs. The calculated strain from the Raman stress measurements are compared with the TEM diffraction based strain measurements.

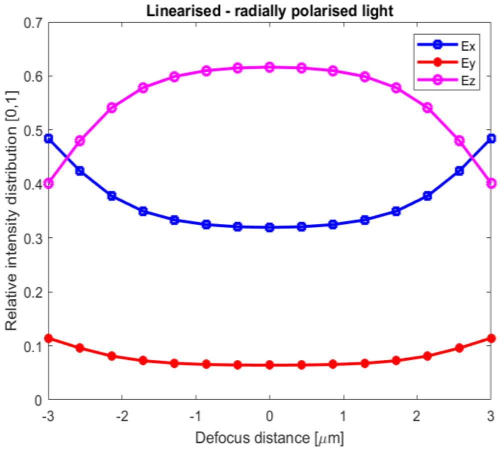

Figure 44 Relative intensity distribution of electric field components as a function of the defocus distance [µm] (defocus zero being the exact focal distance) for linearised radially polarised light.

6.4. Experimental results and discussion

The Raman spectrum obtained in the TO configuration on a blanket structure is shown in Figure 45. we show the spectra obtained using linearly polarised, radially polarised and linearised radially polarised light in Figure 45a, Figure 45b and Figure 45c where it is clear that $z(zy)\bar{z}$ favours the TO$_1$ mode excitation (Table 5).

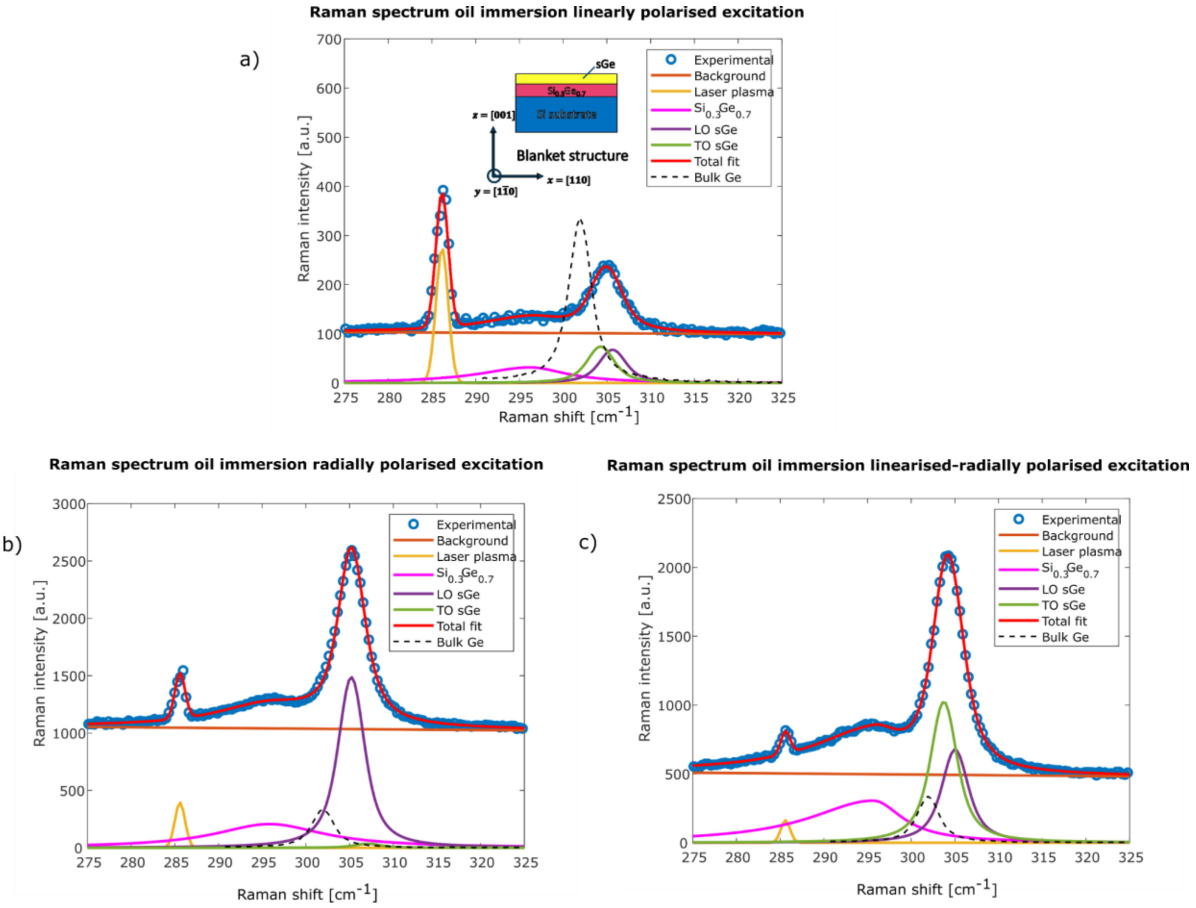

Figure 45 Raman spectrum of the Si-Ge blanket structure in the TO mode a) linearly polarised light , radially polarised light and c) linearised radially polarised light. Notice the strong LO component observed experimentally for the radially polarised light and the strong suppression brought after linearisation as observed from the linearised radially polarised light. Note the shift in the peak position with respect to the expected position for unstrained bulk Ge and the higher peak intensity of the sGe TO peak for the linearised radially polarised light. We observe lower intensity of plasma peak in the case of radially polarised light setup in comparison to the linearly polarised light setup. We suspect the reason could be associated with the higher intensity of longitudinal component of incoming light at the focal plane in comparison to the linearly polarised incoming light and thus resulting in a higher Raman scattered light intensity in comparison to the plasma peak.

Due to the depolarisation effect and non-perfect optics, the LO peak will still be detectable and needs to be separated from the TO peak. For the $z(zy)\bar{z}$ configuration that favours the TO$_1$ excitation (Table 5), the LO component observed experimentally for the radially polarised light (Figure 45b) is very strong and impacting severely on identification of the TO peak and thus the reliability of the stress measurements. A strong suppression of the LO is brought after linearisation due to reduction in the Ey component as observed for the linearised radially polarised light (Figure 45c). We can clearly observe the difference in the expected peak positions for bulk, unstrained Ge (dashed line in Figure 45a,b and c) versus the position for the strained Ge (sGe).

Voigt profiles are used to fit the TO and LO peaks in Ge. The $Si_{0.3}Ge_{0.7}$ peak is fitted (Levenberg-Marquardt least square) using an asymmetric function [140] (Appendix 4) which was found to give a better fit in comparison to a single Gaussian or a set of Gaussian and Lorentzian functions. Note that although the peak parameters for this peak are not used in our strain analysis it does lead to an optimal fitting for the other modes. The Rayleigh scattered plasma peaks from the He-Ne laser are used as reference peaks to account for any instrumental drifts in the overall peak positions and these are fitted using Gaussian profiles.

The experimental procedure for measuring the stress is as follows: First the LO mode spectrum is acquired in the $z(xx)\bar{z}$ configuration, and the parameters of the LO peak (as fitted with a Voigt profile) of sGe are obtained. Similarly, the peak parameters of the asymmetric function fit for $Si_{0.3}Ge_{0.7}$ are obtained. These parameters are fixed while fitting the TO spectrum that is recorded in TO mode (implying use of a different combination of polarisers and analysers in the experiment). This reduces the number of free parameters for the non-linear fitting or optimization algorithm and increases the accuracy of the fitting routine. The same parameters for the $Si_{0.3}Ge_{0.7}$ SRB (strain relaxed buffer) are used in both the TO and LO spectrum due to the fact that strain is relaxed in the SRB meaning that the TO and LO peaks are degenerate [see eqs. 65-67]. We also fix the TO peak width to be the same as LO peak width. The peak/ line widths of the phonons are affected by the defects and/or impurities (doping) resulting in the asymmetric behaviour (as observed for the $Si_{0.3}Ge_{0.7}$) [141]. However, the stress introduced into the near defect-free semiconductor Ge channel would result in negligible variations to the line widths while predominantly influencing the shift in the peak position, justifying the usage of the same peak/line widths for TO and LO peaks in Ge [142]. The peak position is a free parameter necessary for the stress calculation and is the variable in the optimization. Finally, eqs. 65-66 are used to solve for the two in-plane stresses $\sigma_x$and σ_y. The TO/LO ratio (the TO/LO ratio has been calculated by individually measuring the areas of the TO and LO peaks) as calculated from multiple measurements for the linearly polarised light setup was 1.1 ± 0.2 while for the linearised radially polarised setup it was 1.6 ± 0.3. The error values quoted are the standard deviations of the ratios over 10 measurements at multiple locations near the center of the blanket structure and can vary depending on the SNR in the data. Hence an initial calibration of the laser intensity was made on a bulk Ge sample so that a good SNR is obtained while accounting for negligible thermal shifts in the phonon peaks. The data quality (or SNR) is assessed by calculating the uncertainty in the estimated peak position from Levenberg-Marquardt optimization for the bulk Ge Raman spectrum fitted with a Voigt profile.

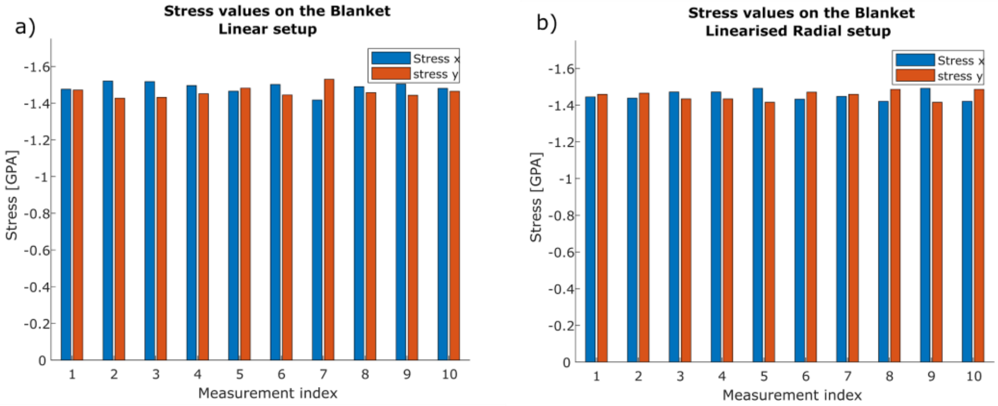

Figure 46 Stress measured on the blanket structure on different locations near the center of the blanket structure using a) linearly polarised light setup and the b) linearised radially polarised light setup. Note the clear indication of biaxial nature of stress in these structures. Measurement index indicates the measurements done on the same positions for both the setups while scanning an area near the center of the blanket structure

The Ge TO peaks show a higher peak intensity for the linearised radially polarised setup (Figure 45c) in comparison to the linearly polarised setup due to the increase in the relative intensity of the longitudinal Ez component as summarised in the numerical simulation section. Figure 46 illustrates the stress measured on the blanket structure using linearly polarised (Figure 46a) and linearised radially polarised (Figure 46b) light. The measurements are done on the same positions for both the setups while scanning an area near the center of the blanket structure. The average stress in the x and y directions are summarised in Table 9.

Table 9 Stress values measured using linearly polarised and linearised radially polarised incoming light setup on the Ge layer of the blanket structure.

Polarization	Stress σ_x[GPa]	Stress σ_y[GPa]
Linear in x	-1.47 ± 0.05	-1.48 ± 0.05
Linearised radial	-1.45 ± 0.03	-1.45 ± 0.03

The error values on the stress measurements quoted here from both the linearly polarised and the linearised radially polarised setups are the standard deviations of the stress measurements in Figure 46. Please note that the statistics for these Raman measurements are different from the statistics of the TEM measurements because the TEM measurements are essentially done on a singe TEM sample consisting of a single fin while Raman measurements are done on an ensemble of fins. These Raman measurements, as expected, indicate biaxial in-plane compressive stress of equal magnitude in both planar directions in the blanket structure. The linearised radially polarised setup shows better precision (calculated as standard deviation in the stress values) in the stress calculation in comparison to the linearly polarised setup due to the increase in the longitudinal component of the incoming light which is expected to reduce the uncertainty in detecting the TO peak. However, in order to quantify experimental stress/strain accuracy for both the Raman setups, measurements are to be performed on a sample with known stress values or by inducing known uniaxial/biaxial stresses on a bulk sample through application of calibrated external forces[124,143,144].

To confirm these results, TEM strain measurements using diffraction-based techniques like nano-beam diffraction [28,29,61,140] and Bessel diffraction [33] (section 2.1.2) are performed, which are known to provide very good accuracy and precision for nano-scale strain measurements. The measurements are done on two perpendicular cross-section TEM lamellae prepared along the x and y directions. The lattice mismatch is calculated with respect to a reference Si substrate in the xz and yz planes (Figure 47), where the results are later used to calculate strain in the Ge region with respect to bulk unstrained Ge (Table 10). The TEM diffraction experiments are performed using a Thermo Fisher Titan^3 aberration-corrected microscope operating at 300 kV. The convergence angle used for NBED was ~0.2 mrad and ~6 mrad for Bessel diffraction. The precision measured as the standard deviation of strain over the reference Si area on the two perpendicular lamellae under the same illumination conditions is 7 x 10^{-4} for NBED and 9 x 10^{-4} for Bessel.

Now we can compare the overall strain as measured with Raman and TEM in Table 10. The strain values reported from the Raman measurements are calculated from the measured stress values using the theory of elasticity and Hooke's law [42,145] with the known values of the compliance matrix for Ge [146]. Analysing the normal strain values in the three perpendicular directions from TEM and Raman (Table 10) we find a close correspondence between the biaxial compressive normal strain in the x and y directions. However, the observed average tensile strain in the z direction (ε_{zz}) from TEM is lower than the calculated value from the Raman data.

The difference could be explained by the strain relaxation inherent to the thin TEM lamella preparation (< 200 nm thickness). The relaxation is predominantly along the thickness direction versus the width of the lamella, as the latter is much larger (~1 to 2 µm), and it is clear that this relaxation will influence the tensile strain in the z direction. This predominant relaxation through the thickness of the lamella is believed to lead only to tensile strain relaxation in the z direction and hence, it is not possible to measure directly as in the case of projection techniques like NBED and Bessel difraction. Hence, two perpendicular cross section lamellae are needed (section 1.2) to evaluate normal strains along the three crystal coordinates x = $[110]$, y = $[-110]$ and z = $[001]$. With this comparison it can be concluded that the strain relaxation along the width of the TEM lamella (~ 1 -2 µm) is less pronounced in comparison to relaxation through the thickness of the TEM lamella (~150 - 200 nm) and the normal strain measured along the width is an indicative of the true bulk strain value. However, the exact modelling of the relaxation effect requires more complicated analysis using finite element method (FEM) simulations of the device structure [84] and will not be discussed in this thesis. Some studies in literature have shown that even for samples as thick as 300 nm, the strain relaxation at the free surface of the TEM lamella is prominent and cannot be neglected and the stress/strain relaxation increases drastically as the thickness decreases [147,148].

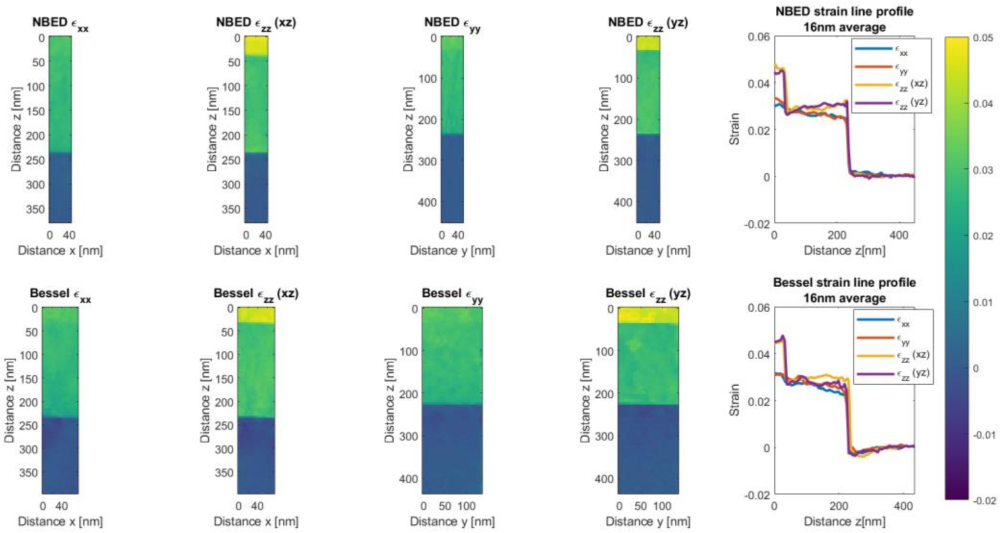

Figure 47 Strain maps on the blanket structure from NBED and Bessel diffraction. The strain maps shown are from two perpendicular cross section lamellae in the xz and yz planes on the blanket structure. The line profiles drawn are averaged horizontally over a distance of 16 nm.

Table 10 Strain values in the three perpendicular directions in strained Ge region with respect to bulk Ge as reference. The values obtained from Raman are calculated from the measured stress values using Hooke's law and stress-strain relations in the elastic regime. The ε_{zz}values from the TEM measurements are an average of the individual measurements in the xz and yz planes from the two perpendicular cross section lamellas. The uncertainty values are a measure of standard deviation from the observed strain values in the data.

Technique	ε_{xx}	ε_{yy}	ε_{zz}
Bessel diffraction	(-11 ± 1) x 10^{-3}	(-10 ± 1) x 10^{-3}	(3 ± 1) x 10^{-3}
Nano-beam diffraction (NBED)	(-10.9 ± 0.7) x 10^{-3}	(-9 ± 0.9) x 10^{-3}	(3.3 ± 0.6) x 10^{-3}
Raman linearly polarised setup	(-10.2 ± 0.3) x 10^{-3}	(-10.1 ± 0.3) x 10^{-3}	(7.5 ± 0.2) x 10^{-3}
Raman linearised radially polarised setup	(-10.2 ± 0.2) x 10^{-3}	(-10.5 ± 0.2) x 10^{-3}	(7.6 ± 0.1) x 10^{-3}

We also compare the two variants of Raman spectroscopy utilized, namely using the oil immersion lens with linearly polarised incoming light and the linearised radially polarised incoming light as applied for measurement on 16 nm-wide finFET structures (Figure 48). For the purpose of comparison of the two variants, the TO/LO ratio has been calculated by individually measuring the areas of the TO and LO peaks. The ratios are calculated over multiple measurements and the linearly polarised light yields a TO/LO ratio of 0.6 ± 0.2 while linearised radially polarised light yields 1.2 ± 0.3. This again clearly illustrates that the linearised radially polarised light provides a higher TO/LO ratio in comparison to linearly polarised light and translates directly to the improved precision in the stress measurements as discussed below.

The stress measurements were performed on the 16 nm finFET structure as shown in Figure 49. Here, the stress σ_y measured along the length of the finFET channel is higher in comparison to σ_x, reflecting the fact that these structures are designed to exhibit uniaxial stress along the channel direction. The average stress measured using linearly and linearised radially polarised light setup is summarised in Table 11.

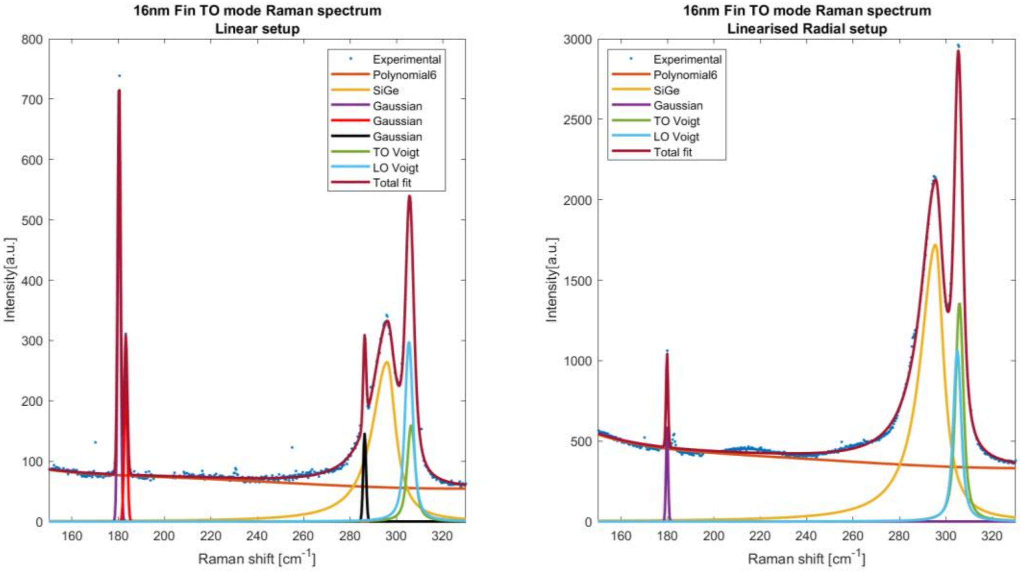

Figure 48 Raman spectra obtained on a 16nm fin using oil immersion lens from a linearly polarised and a linearised radially polarised setup. The plasma lines are associated with the Rayleigh scattering of laser light and are positioned respectively at 180.2 cm^{-1}, 286.2 cm^{-1} and so on and are fitted using the Gaussian profile *[149]*

Table 11 Stress values measured using linearly polarised and linearised radially polarised incoming light setup on the 16 nm fin Ge channel. The error values on the stress measurements quoted here are the standard deviations obtained from multiple measurements.

Polarization	Stress σ_x[GPa]	Stress σ_y[GPa]
Linear in x	-0.45 ± 0.05	-2.29 ± 0.05
Linearised radial	-0.48 ± 0.02	-2.26 ± 0.02

Note that while the absolute values for the stress measured using both techniques agree well, there is a clear difference in standard deviation between the two, already testifying to the advantage of using a radial polariser in the setup. The measured standard deviations in the stress values are attributed to the different TO/LO ratios and in this regard, the linearised radially polarised setup clearly outperforms the linearly polarised setup. The same curve fitting procedure was used for the fins as in the case of blanket structures, but it was observed that the Si$_{0.3}$Ge$_{0.7}$ peak in TO-mode does not match with that in LO-mode for the fin structures. This suggests that the Si$_{0.3}$Ge$_{0.7}$ is not completely relaxed as a strain relaxed buffer (SRB), and some residual stress is present in this layer too. TEM measurements are also taken with the two perpendicular cross section samples as shown in Figure 50. Here, we refer to the TEM sample cut along the xz plane of the finFET as the “cross-section lamella” and the sample cut along the yz plane as the “long-section lamella”. The ε_{yy} and ε_{zz} line profile plots are not equal in the Si$_{0.3}$Ge$_{0.7}$ region as identified by both NBED and Bessel diffraction, which gives additional evidence for the assertion that the Si$_{0.3}$Ge$_{0.7}$ region is not completely stress and strain free. The lattice mismatch measured between Si and fully relaxed Si$_{0.3}$Ge$_{0.7}$ is $\varepsilon_{SiGe-Si} = 0.0297$ and analysing the line profiles for ε_{yy} and ε_{zz} , it can be noticed that ε_{yy} is lower than $\varepsilon_{SiGe-Si}$ indicating that SiGe region is compressively strained resulting in $\varepsilon_{zz} > \varepsilon_{SiGe-Si}$,tensile strain due to Poisson effect.

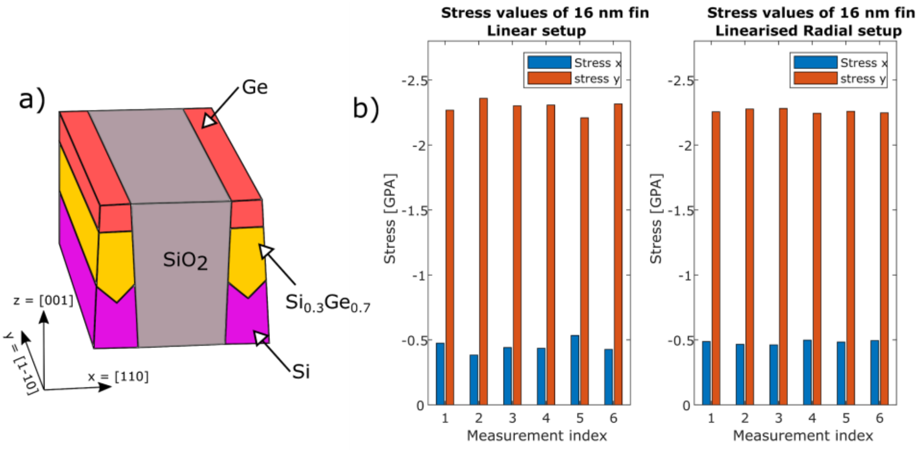

Figure 49 a) Schematic showing the building block of the finFET array where the finFETs are 16nm wide and are distanced apart by a constant pitch of 200 nm. The building blocks are spatially repeated next to each other to form an array of 16nm finFET nanodevices. In Raman measurements, two to three building blocks are probed depending on the spatial resolution or the electric field distribution of light. b) Stress measured at different locations on the length of the structure using oil immersion lens and linearly polarised setup and the linearised radially polarised setup. Note the clear indication of uniaxial stress in these structures.

The residual stress/strain could be developed during to the shallow trench isolation (STI) process after thermal oxidation (~1000°C) [150]. Although the results from the previously investigated TEM techniques (chapter 3 and 4) show some evidence for residual strain in Si$_{0.3}$Ge$_{0.7}$ with the ε_{yy} and ε_{zz} line profiles for the 16 nm fin, the differences remain within the accuracy limits of the techniques and are therefore difficult to ascertain. The reason for the small difference between ε_{yy} and ε_{zz} could be speculated to the Si reference region used for calculating the lattice mismatch i.e., the Si reference region considered for the calculation is surrounded by STI for the previously investigated TEM techniques. This would mean that the Si reference considered for the calculations is speculated to be already in a residual strain state as opposed to the calculations presented in Figure 50, where the Si reference (for lattice mismatch calculation) is away from the STI and free from the thermal stress effect. Finally, we report the measured strain values from TEM techniques and the calculated strain values from Raman for the Ge channel in the fin in Table 12. We observe that the strain is almost relaxed in ε_{xx} due to the reduced width of the fin, a compressive strain ε_{yy} along the length of the fin and a tensile strain ε_{zz} along the vertical or the growth direction [001] is observed due to the Poisson effect. Note that the ε_{zz} values seen from TEM measurements are close to the calculated values from Raman, suggesting a reduced impact of relaxation effects. The apparently smaller relaxation effect for 16 nm fins in comparison to blankets can be understood by the fact that strain is already almost relaxed in ε_{xx}. For the TEM sample along the long section of fin used to measure ε_{zz} in our experiment (Figure 50), i.e. along the yz plane, the relaxation due to sample thinning would have a lower contribution in x (through the thickness) since ε_{xx} is almost relaxed prior to sample preparation.

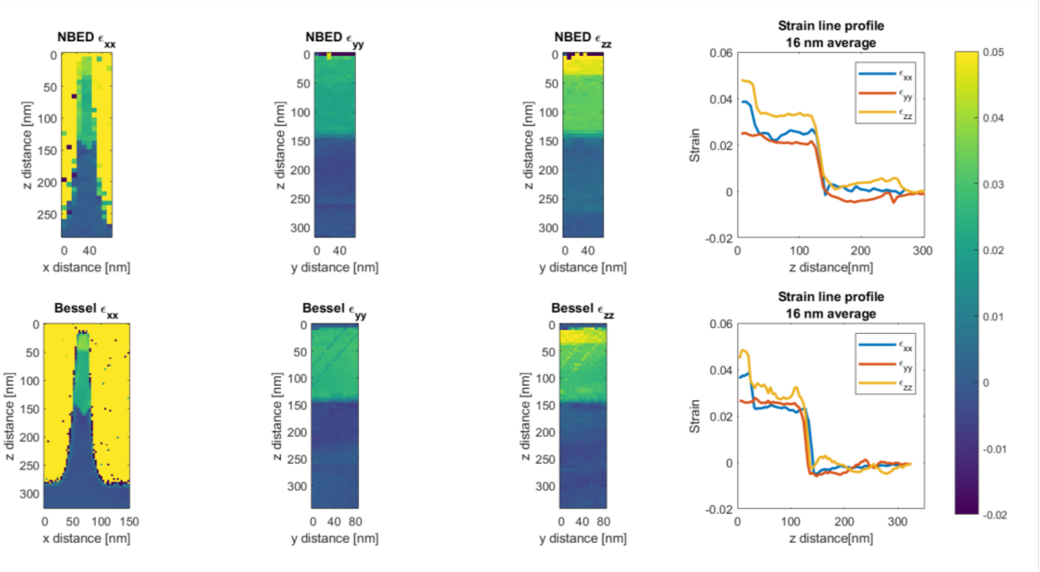

Figure 50 Strain measurement on a 16nm fin. The ε_{xx}, $\varepsilon_{yy}$and ε_{zz} maps are drawn from two perpendicular cross section TEM lamellae. The line profiles are drawn vertically over the maps and are averaged horizontally over 16 nm.

The precision of the TEM techniques was also analysed for the measurements on the finFET (standard deviation on the reference Si region under identical acquisition conditions away from the STI region) and was found to be 9 x 10^{-4} for both NBED and Bessel techniques. The ε_{yy} and ε_{zz} strain maps show a higher standard deviation in comparison to the precision analysed for the same measurement. This could be accounted for by the amorphous SiO_2 surrounding the FinFET. For the long section TEM sample in the yz plane (used to measure ε_{yy} and ε_{zz}), the amorphous SiO_2 overlays with the crystal structure along the path of the travelling electrons (or through the thickness of the lamella) during measurement, while this situation is avoided for a cross section TEM lamella (xz plane). This results in an electron beam passing through both amorphous SiO_2 and the crystal structure for a long section TEM lamella resulting in more diffuse scattering from the amorphous region [151] and thus can explain the higher standard deviation in

ε_{yy} and ε_{zz} strain maps. The strain values from the TEM measurements agree within the accuracy limits of the techniques (Table 10 and Table 12) which, as measured on a bulk Ge sample (Appendix A2.2) with known lattice parameters, is equal to 1-2 x 10^{-3}. The Raman measurements average over a much larger area (approximately 1 μm^2) than the TEM measurements and hence have lower standard deviations over their measurements. In summary, TEM measurements provide a more nanoscopic view into the strain distributions on the sample but require sample preparation and are more susceptible to strain relaxation along the thinner side of the lamella.

Table 12 Strain values from the three perpendicular directions in the strained Ge region for the fin structure. The values obtained from the Raman are calculated from the measured stress values using Hooke's law and stress-strain relations in the elastic regime. The uncertainty values are a measure of standard deviation from the observed strain values in the data.

Technique	ε_{xx}	ε_{yy}	ε_{zz}
Bessel diffraction	(-4.1 ± 0.8) x 10^{-3}	(-14 ± 2) x 10^{-3}	(6 ± 3) x 10^{-3}
Nano-beam diffraction (NBED)	(-3.5 ± 0.9) x 10^{-3}	(-16 ± 1) x 10^{-3}	(6 ± 2) x 10^{-3}
Raman linearly polarised setup	(-2.8 ± 0.4) x 10^{-3}	(-16.5 ± 0.4) x 10^{-3}	(7.1 ± 0.2) x 10^{-3}
Raman linearised radially polarised setup	(-3.0 ± 0.2) x 10^{-3}	(-16.4 ± 0.2) x 10^{-3}	(7.1 ± 0.1) x 10^{-3}

6.5. Conclusion

We investigated the use of Raman spectroscopy for the measurement of strain in semiconductor nano-devices, in particular when using two different types of incoming light polarisations, namely the linearly polarised light and linearised radially polarised light. Linearised radially polarised light is shown to provide a higher TO/LO ratio which improves the sensitivity in determining the TO peak, which in turn leads to more precise stress measurements. The Raman measurements are compared with TEM diffraction techniques and a good agreement in the strain values is seen within the accuracy limits of the TEM techniques except for the strain in the z-direction where the relaxation within the TEM lamella leads to lower strain values. The Raman technique provides a fast and efficient way for measuring stress-strain while requiring no additional sample preparation steps. As the strain measurements in Raman are averaged over many fins, a more statistically relevant averaged value is obtained whereas, the TEM techniques provide a more nanoscopic view of the strain distribution within a device with spatial resolutions down to 2 nm as illustrated with the analysis of a 16 nm finFET. The introduction of a linearised radially polarised setup is straightforward as it only requires installing an s-waveplate and a linear polariser directly in the incoming laser path of a traditional micro-Raman setup operating with a linearly polarised laser source. We demonstrate through this work that linearised radially polarised light provides an optimised Raman measurement both in terms of spatial resolution and in stress/strain precision.

Strain comparison

In this section, we compare the strain measurements from TEM techniques and the Raman spectroscopy technique. The comparison has been done on the blanket/test structure and the 16 nm finFET nanodevice. Figure 51a shows the strain comparison made on the blanket structure. The average strain value in the Ge region is plotted in the bar chart and the error bars correspond to the standard deviation of the measured strain. Two orthogonal cross section TEM samples (Figure 51 c and d) are prepared to measure strain along the three normal directions i.e. ε_{xx}, ε_{yy} and ε_{zz}. ε_{zz} is calculated from both the samples and an average of ε_{zz} is calculated from both the samples due to the expected in-plane (xy plane) strain homogeneity from the test sample. For high-resolution tomography, a single needle-shaped sample is used to extract three dimensional strain information.

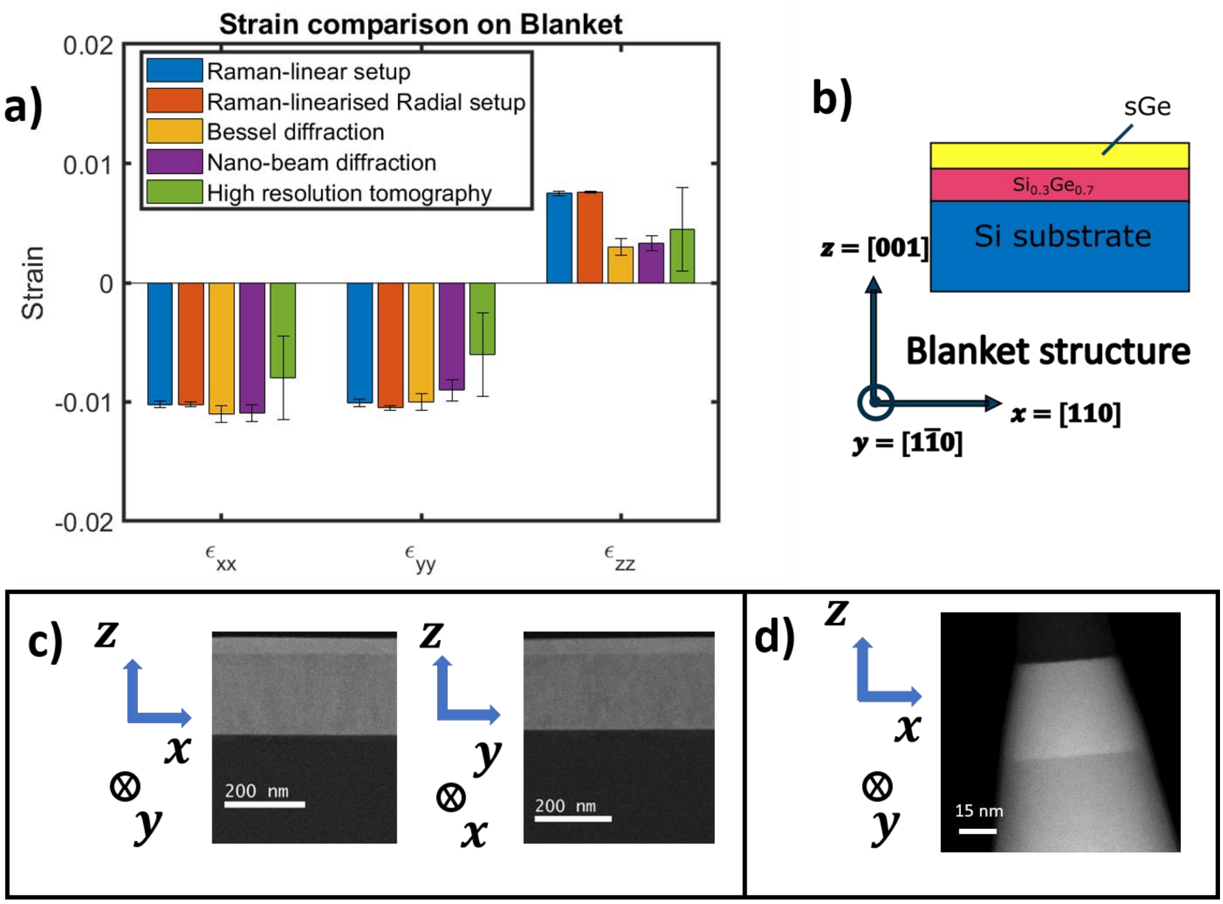

Figure 51 a) Strain comparison from TEM and Raman spectroscopy techniques. The bar chart indicates the average strain value in the Ge region and the error bars are the standard deviation of strain in the Ge region b) Schematic of the blanket/test structure on which the strain comparison is made c) Two orthogonal TEM lamellae for diffraction based techniques NBED and Bessel diffraction d) Needle shaped sample for high-resolution tomography strain analysis.

Analysing the strain values, we can conclude a biaxial compressive in-plane strain in the x and y directions, as expected for the blanket structure. There is disagreement in ε_{zz} for the Raman techniques and the TEM diffraction techniques. This can be related to the strain relaxation along the thickness direction of the TEM sample which results in tensile strain relaxation along the z direction. However, the strain values match within the error bars in x and y, indicating reduced relaxation along the width of the lamella which is ~1-2 µm.

Higher error bars are observed for high-resolution tomography, and since we test the proof of concept in our current investigation, further analysis is necessary for improving precision for 3D strain analysis. However, observing the average strain values one can notice disagreement in ε_{xx} and ε_{yy} in comparison to TEM diffraction based techniques. The cause for disagreement can be linked to the strain relaxation across all directions for a needle shaped sample which is symmetrically thin with diameter ~45 nm. Therefore, from the comparison on the blanket/test structure we can conclude that TEM samples can be prone to strain relaxation especially across the thinner directions of the sample. However, relaxation effects are greatly reduced across the width of the TEM lamellae (Figure 51c).

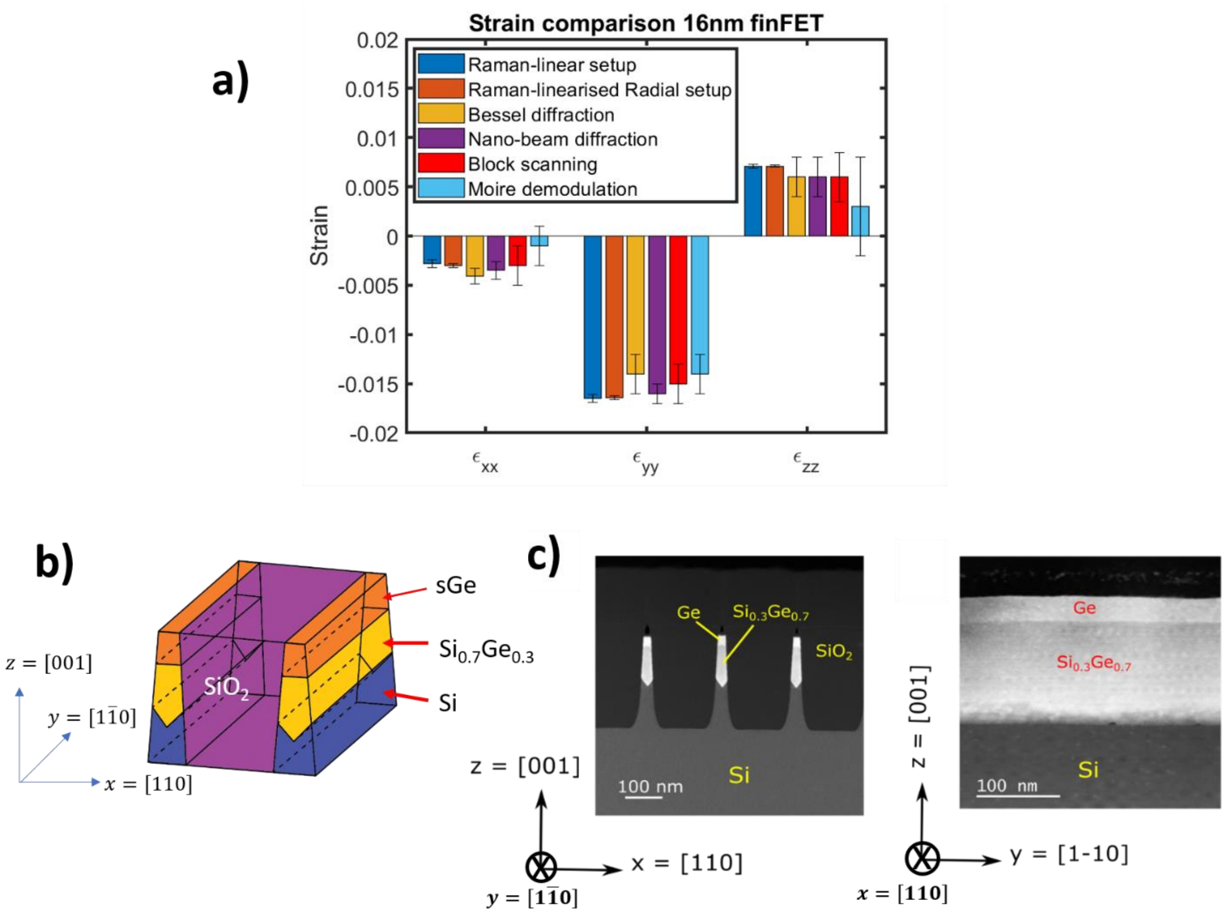

Figure 52 a) Strain comparison on the 16 nm fin from TEM and Raman techniques b) schematic of the 16 nm fin c) Two orthogonal TEM samples used for TEM analysis (xz plane is termed "cross-section" and yz plane is termed "long-section" sample).

We also compare strain measurements from TEM and Raman techniques on the 16 nm fins as shown in Figure 52a. Again, two orthogonally prepared TEM lamellae (xz plane is termed "cross-section" and yz is termed “long-section” sample) Figure 52c is used to measure strain in ε_{xx}, ε_{yy} and ε_{zz}. By, analysing the strain values in Figure 52a, we can observe that strain is relaxed in the x direction and this can be understood from the decrease in the device dimension along the x direction. A compressive uni-axial strain along the length of the fin ε_{yy} is observed as expected for the 16 nm finFET. The compressive strain in the y-direction results in an elongation along the z-direction (free surface) due to the Poission effect. Additionally, we can notice that the strain values in ε_{zz} match within the error bars for both the TEM and Raman techniques. In this case, the long-section sample (yz plane) is used to analyse strain ε_{yy} and ε_{zz}. For the long-section sample, the strain along the thickness direction (x-direction) is almost relaxed prior to sample preparation. Hence, the TEM sample preparation induced relaxation along the x-direction would have minimal effect for strain relaxation in ε_{zz}, explaining the close match between the TEM and Raman techniques. One can notice a higher error bar in ε_{zz} for the moiré -demodulation technique, which is associated with the slow-scan artefacts as discussed in section 3.5. The average value in ε_{zz} is also deviating from the other TEM techniques due to lower precision combined with limited number of data points on which it is averaging.

Summary and general conclusions

In this thesis, we investigate strain measurement techniques on semiconductor nanodevices. Strain measurement techniques are vital for the semiconductor industry due to the advantages of incorporating strain into transistor channels that greatly boosts the mobility of the charge carriers and hence the transistor performance. The techniques need to be fast, inline, and able to provide spatial resolution at the nanoscale. Inline techniques like Raman spectroscopy and X-ray diffraction are routinely used for semiconductor strain measurements since they are fast, precise and provide extended field of view strain mapping in the micrometer to millimeter range. However, these techniques lack the nanoscale spatial resolution for strain mapping on individual nanodevices for the latest nodes of semiconductor devices. TEM-based techniques provide the best spatial resolution for nanoscale strain analysis with the capability for extended spatial resolution up to a single or a few unit cells.

The investigation was started by evaluating some of the existing TEM based techniques and Raman spectroscopy and presented them in **chapter 2**. The TEM techniques need special thin samples (≤ 150 nm) for strain analysis and are prone to strain relaxation across the thinner region. The TEM techniques are broadly classified into imaging-based and diffraction-based techniques. The diffraction techniques (including DFEH) provide very good precision ($2 \times 10^{-4} – 6 \times 10^{-4}$), accuracy ($1 \times 10^{-3} – 2 \times 10^{-3}$), spatial resolution (2 – 5nm) and field of view (0.2 – 1 µm). However, these techniques are relatively expensive in terms of data size requirement and relatively slow (data acquisition and analysis time). Even though the imaging techniques are advantageous in terms of cost effectiveness and speed (with potential real time processing capabilities), there are a number of limitations associated with the TEM imaging techniques. For example, HRSTEM is limited by the field of view (< 50 nm) and STEM moiré by the strain spatial resolution (in the order of 10s of nm) which results in a compromise between strain sensitivity and spatial resolution. Additionally, imaging techniques working in the STEM mode are prone to slow scan artefacts due to sample drift, electromagnetic interference or vibration and from the "flyback effect". After identifying some of these aforementioned limitations of the imaging techniques and given their potential for fast and cost effective analysis, we propose new methodologies and analysis protocols for overcoming these limitations.

In **chapter 3,** a significant improvement in the STEM moiré setup is presented by adding a novel quadrature demodulation scheme that decouples the field of view choice from the moiré sampling requirements while offering a far more flexible solution. The newly proposed methodology has enabled selective enhancement of spatial frequencies (positive/negative part) while strongly suppressing the rest of the components in the FT. This enables the GPA mask to potentially extend up to the entire Fourier space of the image and substantially improve the spatial resolution (upto a single unit cell). However, in reality increasing the mask size would also lead to an increase in noise in the strain map. Hence, an inverse relation between spatial resolution and precision keeps representing a serious limitation for high spatial resolution measurements with adeqaute precision. For example, the precision obtained (fast-scan direction) was 1 x 10^{-3} for a spatial resolution of 3 nm, degrading to 3.5 x 10^{-3}, while targeting a spatial resolution of 1 nm. The accuracy of the technique was measured at 2 x 10^{-3} and the field of view 250 – 300 nm. Scan artefacts are observed in the slow scan direction due to sample drift that can happen during the acquisition. The technique also boosts the sensitivity enabling to more precisely probe the strain values.

Slow scan artefacts are predominant in STEM scanning mode and lead to reduced precision. The image corrections methods for HRSTEM typically operate on a series of fast scanned (0.4 – 0.6 µs dwell time) images with lower field of view (< 50 nm). Many other correction routines typically require multiple acquisitions and hence are time consuming (require higher electron dose). In order, to obtain reliable and precise strain information in the slow scan direction, a new scanning strategy called “Block-scanning” is proposed in **chapter 4**. The precision obtained for a 3 nm spatial resolution is 1 x 10^{-3} in the fast scan direction and 3 x 10^{-3} in the slow scan direction. Even though the precision obtained in the slow scan direction is slightly lower than the fast scan direction, the technique is superior to the conventional raster scan as up to three-fold reduction in slow-scan artefacts is demonstrated. The accuracy is measured to be ~2 x 10^{-3} and the technique also provides a wider and flexible field of view (~200 nm) provided that atomic resolution is maintained at every sub-image/block.

The state-of-the art and newly-proposed TEM techniques are measuring strain on a projection direction along the [110] zone axis assuming that strain is uniform through the thickness of the TEM sample/ lamella. Hence one requires two perpendicular cross-section lamellae for measuring strain in three perpendicular directions. This means that these two samples also experience different relaxations depending on their thickness and demands overall extra sample preparation time due to the need for two samples. Here again, one lacks the ability to decipher strain through the thickness of the samples as it is not a true 3D measurement. In order to measure the true 3D strain distribution of the semiconductor nanodevice, high-resolution tomography is explored. The experimental procedure and results are presented in **chapter 5**. We show the proof of concept for 3D strain measurement on a SiGe blanket/test structure. The strain is measured on a test/blanket structure and even though 3D visualiation and quantification of strain has been achieved, the measurements suggest notable strain relaxation due to thin needle-shaped sample (< 50 nm) preparation. This makes strain tomography for semiconductor samples problematic as the requirement for sample thickness leads to extensive relaxation and renders the result unrepresentative for the actual strain state of the original embedded device. Potentially for much smaller transistors this could be less of a problem when strain in the surrounding matrix is already relaxed (for example, ε_{xx} is almost relaxed in the case of a 16 nm FinFET). We see no obvious solution for this dilemma. A totally different use case would be that of individual nanoparticles that also show strain relaxation, only this time the relaxation is what naturally occurs in these particles and is what we actually want to characterise.

In **chapter 6**, the Raman strain measurement technique has been presented. We explore linearised radially polarised light as the incoming light to achieve higher TO/LO phonon intensity ratio which mitigates the deconvolution problem and has been demonstrated to yield better precision in comparison to the conventional linearly polarised setup. The improvements can be understood based on numerical simulations of the relative electric field intensities which demonstrate that higher TO/LO ratio is obtained in this configuration. The results are compared against the TEM based diffraction techniques like NBED and Bessel diffraction. The results from TEM and Raman match in ε_{xx} and ε_{yy} within the accuracy limits of the TEM techniques (1-2 x 10^{-3}). The discrepancy in ε_{zz} is assigned to the strain relaxation through the thickness of the TEM sample that indirectly affects the strain relaxation along the growth direction or ε_{zz}. Although FEM simulation of the relaxation could accompany the TEM results, a unique answer will be hard to obtain taking into account the uncertainty on the material properties of all the materials in a complex device

From a metrological standpoint, samples with different thicknesses produced from the same wafer might result in varying results depending on the thickness variation among the samples. The differences would be minimal for normal strains along the width of the lamellae i.e. ε_{xx} and ε_{yy} and this observation is made after comparing TEM and Raman on the test/blanket structure where ε_{xx} and ε_{yy} match within the accuracy limits of the TEM techniques. However, a systematic study for reproducilibilty involving characterisation of strain on multiple sets of samples with varying thicknesses would be necessary to fully uncover some of the observations made from this study.

The precision obtained from Raman techniques are better than TEM techniques as demonstrated on the 16 nm finFETs and the blanket structure. Raman averages over multiple devices and is an asset as it improves the statistical significance of the results as long as the inter device variation is kept small, which is the goal of the semiconductor industry. The TEM techniques on the other hand provide a more nanoscopic view of the strain distribution within a device with spatial resolutions down to 2 nm or less. Even though the TEM techniques suffer from sample preparation induced strain relaxation, they are currently the only techniques capable of strain spatial resolution (even less than 1 nm) for closer inspection and strain/defect analysis at the nanoscale. On the other hand, an inline technique like Raman spectroscopy serves for faster analysis and can be routinely used for production-scale quality control and assurance.

Finally, the highlights of the improvements or contributions made from this thesis to the attributes of the state-of-the art strain measurement techniques are tabulated below in Table 13. In Table 14, the performance metrics of the new techniques proposed in this thesis are tabulated. The precision and accuracy are calculated for the given spatial resolution. As demonstrated throughout the thesis, the precision degrades with an increase in spatial resolution and these parameters are interdependent.

Table 13 Comparison of the parameters of the state-of-the art techniques (Before) and the improvements made through this thesis (After).

Technique	Parameters	Before	After	Remarks
STEM moiré	Spatial resolution	~ In the order of 10s of nm	≤ 2 nm	Through the application of a novel moiré demodulation scheme
HRSTEM	Strain Precison (Slow scan direction)	~ 9 x 10^{-3}	~ 3 x 10^{-3}	Through the application of Block-scanning
	Field of view	≤ 50 nm	~ 200 nm	
High resolution tomography	3D strain	-	Calculation of 3D strain tensor and strain visualization though the sample	Proof of concept for calculation of all the strain tensors from a single sample or measurement. (Strain relaxation is problematic for semiconductor application)
Raman spectroscopy	Strain Precision	3 x 10^{-4}	2 x 10^{-4}	Through the usage of linearised radially polarised light.
	Stress precision	0.05 GPa	0.02 GPa	

Table 14 Precision and accuracy performance metric for the given spatial resolution for the newly investigated techniques in this thesis. The experimental accuracy for HR tomography and Raman are not investigated due to the lack of reference sample systems and needs to be considered for future investigations. ***Warning****: the accuracy values quoted here are measured on a strain relaxed Ge on top of Si. However, when measuring strained TEM samples, strain relaxation due to sample preparation has to be taken into account. Thus, the accuracy values quoted here are the best attainable values from these techniques.*

Technique	Precision	Accuracy	Spatial resolution
Moiré demodulation	3×10^{-3}	2×10^{-3}	1.5 nm
Block scanning	1×10^{-3}	2×10^{-3}	3 nm
High-resolution tomography	[I] 4×10^{-3}	-	2 nm
Raman spectroscopy (Linearised radially polarised setup)	2×10^{-4}	-	Multiple fins (5-10), 0.5 – 1 µm

---

[I] Calculated along $[1\bar{1}0]$ projection direction.

Samenvatting en algemene conclusies

In dit proefschrift onderzoeken we deformatie meettechnieken in halfgeleider nano apparaten. Deformatie meettechnieken zijn vitaal voor de halfgeleider industrie omwille van de voordelen die deformatie geven in transistor kanalen. De deformatie stimuleert de mobiliteit van ladingsdragers wat ervoor zorgt dat de performantie van de transistoren ook verbeterd. De technieken moeten snel, inline gebeuren en nano schaal spatiale resolutie hebben. Inline technieken zoals Raman spectroscopie en x-ray diffractie worden routinematig gebruikt voor halfgeleider deformatiemetingen omdat deze techniek snel, precies en een gezichtsveld variërend van micro tot millimeter hebben. Het nadeel van deze technieken is dat hun spatiale resolutie onvoldoende is voor deformatiemetingen op individuelen nano apparaten. TEM gebaseerde technieken hebben wel de spatiale resolutie voor nanoschaal deformatie analyse met het vermogen om spatiale resolutie te hebben van een enkele of meerdere eenheidscellen.

Het onderzoek startte door het evalueren van enkele bestaande TEM gebaseerde technieken en Raman spectroscopie. Deze resultaten worden getoond in hoofdstuk 2. De TEM technieken gebruiken speciale dunne monsters (<150 nm) voor deformatie analyse en zijn dus vatbaar voor deformatie relaxatie over de dunne regio. De TEM technieken kunnen voornamelijk in twee verschillende methodes opgedeeld worden: beeldvorming en diffractie. The diffractie technieken (inclusief DFEH) hebben een zeer goede precisie (2x10-4 - 6x10-4), nauwkeurigheid (1 x 10-3 – 2 x 10-3), spatiale resolutie (2-5 nm) en gezichtsveld (0.2-1 um). Deze technieken zijn wel relatief duur in termen van data grootte en de data acquisitie en analyse tijd is relatief lang. Daartegenover zijn deze technieken voordelig in termen van kosten efficiency en snelheid (met potentieel tot live data verwerken) maar er zijn ook een paar nadelen. Zoals HRSTEM is gelimiteerd in de grootte van het gezichtsveld (<50 nm) en voor STEM moiré moet er een compromis gemaakt worden tussen spatiale resolutie en deformatie gevoeligheid. Verder hebben beeldvorming technieken werkende in STEM modus invloed van scan artefacten omwille van monster drift, elektromagnetische interferentie, vibraties en door het terugvliegen van de elektronenbundel tijdens het scannen. Na het identificeren van de limitaties van deze technieken en hun potentieel tot snelle en kosteneffectieve analyse, stellen we nieuwe methodologieën en analyses voor om deze limitaties te overwinnen.

In hoofdstuk 3 is een significante verbetering van de STEM moiré opstelling besproken. Deze opstelling voegt een nieuwe kwadratuur demodulatie techniek toe die het gezichtsveld ontkoppeld met de moiré bemonstering. Dit zorgt voor een meer flexibele oplossing. The voorgestelde methodologie zorgt ervoor dat er een selectieve verbetering optreed van bepaalde spatiale frequenties (positief/negatief deel) terwijl andere Fourier componenten sterk gereduceerd worden. Dit zorgt ervoor dat het GPA masker potentieel tot de gehele Fourier ruimte genomen kan worden wat de spatiale resolutie verbeterd tot en met een enkele eenheidscel. Hoewel door het masker zo groot te nemen, zal er meer ruis optreden in de deformatie map. Er blijft dus een omgekeerde relatie tussen resolutie en precisie wat voor een serieuze limitatie zorgt voor hoge spatiale resolutie metingen met voldoende precisie. Bijvoorbeeld, de precisie verkregen (snelle scan richting) was 1 x 10-3 voor een spatiale resolutie van 3 nm, dit wordt 3.5 x 10-3 voor een resolutie van 1 nm. De nauwkeurigheid van de techniek was 2 x 10-3 en het gezichtsveld 250 – 300 nm. Scan artefacten omwille van monster drift was waargenomen tijdens de metingen. Deze techniek versterkt ook de gevoeligheid wat voor meer precieze deformatie metingen zorgt.

Trage scan artefacten zijn dominant in de STEM scan modus en zorgen voor een verlaagde precisie. Correctie methodes om deze artefacten te verwijderen voor HRSTEM hebben meerdere snel gescande (0.4-0.6 µs) beelden nodig met een klein gezichtsveld (<50nm). De meeste correctie methodes hebben meerdere beelden nodig en zijn dus tijdrovend en hebben een hogere dosis nodig. Om deze problemen te overkomen en toch een precieze deformatiemeting te hebben van de trage scan richting, een nieuwe scan strategie was bepaald waarin blok scannen was voorgesteld. Dit wordt besproken in hoofdstuk 4. The precisie van deze methode was 1 x 10-3 in de snelle scan richting en 3 x 10-3 in de trage scan richting met een spatiale resolutie van 3 nm. Hoewel de precisie in de trage richting nog altijd lager is dan voor de snelle scan richting, deze methode is superieur aan de conventionele methodes waar de precisie drie keer slechter is. De nauwkeurigheid van de methode is ~2 x 10-3 en de techniek heeft een groter gezichtsveld (200 nm) maar hiervoor moet er wel in iedere gescande blok atomaire resolutie beschikbaar zijn.

De voorgestelde TEM technieken meten deformatie in een geprojecteerde richting langs de [110] zone as waar dan verondersteld wordt dat de deformatie uniform is door de dikte van het TEM monster. Men heeft dus twee metingen nodig van een andere zone as om de deformatie te meten in drie richtingen. Dit betekent dat twee monsters ook een andere relaxatie vertonen wat afhangt van de dikte en dat er ook meer tijd gespendeerd wordt aan de preparatie van de monsters. Zelfs met twee metingen heeft men niet de volledige driedimensionale meting. Om de echte driedimensionale deformatie van een nano apparaat te meten is dus de methode van hoge resolutie tomografie onderzocht. De experimentele procedure en resultaten zijn besproken in hoofdstuk 5. Hierin tonen we de proof-of-concept voor driedimensionale deformatiemetingen op een SiGe test structuur. De gemeten deformatie stelt dat er opmerkelijke deformatie relaxatie optreedt in het dunne naald monster. Dit zorgt ervoor dat deformatie tomografie voor halfgeleider monsters problematisch is omdat door het dunne monster te veel relaxatie optreedt en dit maakt de resultaten niet representatief voor de echte deformatie van het originele apparaat. De tomografie werkt mogelijks voor kleinere transistors waar deformatie gerelaxeerd is door de omliggende matrix. Bijvoorbeeld ε_{xx} is bijna volledig gerelaxeerd voor een 16 nm finfet. Tot op het heden hebben we nog geen enkele manier gevonden om dit probleem op te lossen. Een totaal ander gebruikssituatie is voor nanodeeltjes waar ook deformatie relaxatie optreedt. Dit gebeurt op een natuurlijke wijze en is hetgeen wat we willen karakteriseren.

In hoofdstuk 6 wordt de Raman deformatie techniek beschreven. Hierin wordt de lineaire radiaal gepolariseerd licht gekozen als invallend licht wat ervoor zorgt dat de intensiteit ratio van de TO/LO fononen wordt vergroot wat het deconvolutie probleem vergemakkelijkt. Verder heeft deze methode ook een betere precisie vergeleken met conventionele lineaire gepolariseerd licht. De resultaten worden vergeleken met diffractie TEM technieken zoals NBED en Bessel diffractie. De resultaten van TEM en Raman komen overeen in het nauwkeurigheidsinterval voor ε_{xx} en ε_{yy} . Het verschil in ε_{zz} komt door de deformatie relaxatie omwille van de dikte van het TEM monster dat invloed heeft op de groeirichting ε_{zz}. FEM simulaties van de relaxatie zijn moeilijk om uit te voeren omdat complete kennis van de materiaal eigenschappen nodig is om dit te beschrijven.

Vanuit een metrologisch standpunt kunnen monsters van dezelfde wafer met een andere dikte, andere resultaten voortbrengen. Het verschil is minimaal voor normale deformatie langs de breedte van het monster dus ε_{xx} en ε_{yy}. Dit was geconfirmeerd door de deformatie van de Raman met de TEM technieken te vergelijken waar beide methodes dezelfde waardes van ε_{xx} en ε_{yy} bekomen binnen de nauwkeurigheden van beide methodes. Om dit te verifiëren moet deze meting gedaan worden voor monsters met verschillende diktes.

De precisie verkregen van de Raman technieken zijn beter dan TEM zoals gedemonstreerd voor de 16 nm Finfet. Raman neemt het gemiddelde over meerdere apparaten wat een voordeel oplevert voor de statistische significantie van de resultaten zolang dat de variatie van de apparaten miniem blijft. De TEM technieken geven een betere spatiale resolutie tot 2 nm of minder. Hoewel TEM problemen heeft met de monster preparatie, wat deformatie relaxatie induceert, blijven deze technieken de enige methodes om deze resolutie te bereiken wat nodig is om defecten en deformatie te onderzoeken op atomaire schaal. Aan de andere kant, Raman spectroscopie is sneller en kan makkelijker gebruikt worden in productie processen voor controle.

De hoogtepunten van de verbeteringen of bijdrage gemaakt in deze thesis van de deformatie meettechnieken zijn getabuleerd in Tabel 13. In Tabel 14 is de performantie van de nieuwe technieken getabuleerd. De precisie en nauwkeurigheid zijn berekend voor een gegeven spatiale resolutie. Zoals gedemonstreerd in deze thesis, neemt de precisie af als de spatiale resolutie verbeterd.

Tabel 15 Vergelijking van parameters van voor en na de verbeteringen besproken in deze thesis

Techniek	Parameters	Voor	Na	Opmerkingen
STEM moiré	Spatiale resolutie	~ In de grootte orde van 10s voor nm	≤ 2 nm	Door de applicatie van een nieuwe moiré demodulatie techniek
HRSTEM	Deformatie precisie (trage scan richting)	~ 9 x 10^{-3}	~ 3 x 10^{-3}	Door de applicatie van het blok scannen
	Field of view	≤ 50 nm	~ 200 nm	
Hoge resolutie tomografie	3D strain	-	Berekening van de 3D deformatie tensor en deformatie visualisatie door het monster	Proof-of-concept voor de berekening van de deformatie tensor van een monster of meting. (Deformatie relaxatie is een probleem voor halfgeleider applicaties)
Raman spectroscopie	Deformatie precisie	3 x 10^{-4}	2 x 10^{-4}	Door gebruik van lineair radiaal gepolariseerd licht.
	Stress precisie	0.05 GPa	0.02 GPa	

Tabel 16 Precisie, nauwkeurigheid en spatiale resolutie voor de nieuwe onderzochte technieken in deze thesis. De experimentele nauwkeurigheid voor HR tomografie en Raman zijn niet onderzocht omdat er geen referentie monster beschikbaar was. Dit werk kan gedaan worden in de toekomst.

Techniek	Precisie	Nauwkeurigheid	Spatiale resolutie
Moiré demodulatie	3 x 10^{-3}	2 x 10^{-3}	1.5 nm
Blok scannen	1 x 10^{-3}	2 x 10^{-3}	3 nm
Hoge resolutie tomografie	[m]4 x 10^{-3}	-	2 nm
Raman spectroscopie (Lineaire radiale polariserende opstelling)	2 x 10^{-4}	-	Meerdere fins (5-10), 0.5 – 1 µm

---

[m] Berekent langs $[1\bar{1}0]$ projectie.

Outlook

The thesis explores and proposes new methodologies and techniques for TEM and Raman spectroscopy for enhanced performance for strain measurement applications at the nanoscale. The techniques employing customised scan strategies like “Block-scanning” and “moiré demodulation” can be incorporated into the existing STEM microscope by any microscope vendor by changing only the scan unit in terms of hardware and the software to control it [81,82].

The analysis for moiré demodulation is very fast and has the potential to be made real-time. The current implementation of block-scanning processing with Python [152] takes approximately twice the time compared to commercially available NBED software like Epsilon [153], hence there is room to further improve the processing speed by implementing parallel computing or switching to system level programming languages like C++. Apart from strain measurement purposes, the block-scanning technique also has the potential to investigate defects (by imaging the entire region with the block scanning fashion and not skipping any regions in between the sub-images, to avoid the risk of skipping over interesting defect areas), interface analysis and crystallographic mapping at the local scale using sophisticated image processing algorithms on the high resolution features inside each block, which have high endurance against slow scan artefacts and sample drift.

For the high resolution tomography, the TEM holders can be improved by extending the degrees of freedom by including alpha-beta tilt along with rotation. This would make the alignment procedure more precise for every experiment as the TEM grids are currently prone to a small degree of bending induced by the clamping mechanism in the holder. The ability for 360° tilt range for the tomography sample through improved/modified TEM holders can prove to be more robust against any missing-wedge-induced reduction of high-resolution contrast in the 3D reconstruction. On the other hand, 3D diffraction tomography can be performed using thicker samples and combining with 4D STEM (involving nano-probe mode like NBED) and reconstructing nanoscale 3D diffraction pattern at every voxel is an interesting area to explore.

Although TEM techniques provide the best strain spatial resolution for 2D and 3D strain mapping, they suffer from sample preparation-induced strain relaxation. Thus, the measurements can vary from the true state of strain in the bulk sample especially along the thinner side of the TEM sample. Hence, the need for nanoscale strain mapping techniques that are non-invasive is very crucial. Electron back-scattered diffraction (EBSD) is one of the promising non-invasive techniques to measure the strain with a lateral spatial resolution of upto 1 nm in the latest SEMs [154]. The penetration depth depends on the beam energy and ideally for semiconductor nanodevices in our study, penetration depths of less than 30 nm is necessary to measure the lattice parameter of the Ge channel region. However, reducing the beam energy to lower the penetration depth will also impact the spatial resolution and difficult to achieve the targeted spatial resolution of 1 nm. Thus, it is challenging to achieve targets of both spatial resolution and penetration depth at the same time and hence novel approaches are required to tackle this problem.

Tip-enhanced Raman spectroscopy is another non-invasive technique that has the capability for enhancing the spatial resolution beyond the diffraction limit of light. The technique provides spatial resolution upto one order higher [155,156] than the conventional far field Raman spectroscopy as investigated in this thesis. However, implementation of the polarised Raman spectroscopy would be rather challenging for semiconductor applications where the plasmonic coupling between the tip and the material becomes crucial. In general, measuring the tri-axial stresses using the traditional back-scattering configuration is also a challenge so far due to the difficulty in exciting the weakly scattered TO_2 phonon which is usually accompanied by a very strong LO phonon. Hence, further exploration is necessary in terms of expanding the capabilities for triaxial stress measurements using Raman spectroscopy in the backscattering setup or off-axis polarisation setup through novel approaches or methodologies.

Acknowledgements

First of all, I would like to thank my promotors Prof. Dr. Sara Bals, Prof. Dr. Johan Verbeeck and Prof. Dr. Wilfried Vandervorst for their immense support and guidance throughout the thesis. Their expertise was invaluable in formulating research questions. Without their constant feedback on the research methodologies and insightful scientific discussions, this thesis would not have been possible.

I would also like to thank my colleagues in imec Dr. Thomas Nuytten, Dr. Hugo Bender, Dr. Paola Favia and Dr. Olivier Richard for sharing their technical know-how and stimulating discussions which greatly enriched my research. I thank Hugo for car-rides from imec to Antwerp and nice discussions on the way.

I would also like to acknowledge the experimental and technical guidance I received from my collegues in EMAT, Dr. Armand Beche, Prof. Dr. Thomas Altantzis and Dr. Giulio Guzzinatti, which was instrumental for my work. I thank Stijn Van den broeck for his meticulous efforts in preparing the FIB needle shaped samples for tomography.

Many thanks to the jury members Prof. Dr. Pierre Van Mechelen, Prof. Dr. Paul Scheunders, Dr. Martin Hytch and Dr. Thomas Nuytten for their encouraging feedback and useful comments which led to overall improvement of the thesis. I also like to thank our collaborators in CNRS, France for providing the scan unit hardware for customised scanning.

I would like to greatly acknowledge the support from Dr. Nathalie Claes, Dr. Kellie Jenkinson and Dr. Ajinkya Anil Kadu whose guidance was valuable in shaping my thesis presentation. Special thanks to Daen Jannis for translating the summary part to Dutch. I also like to thank my collegues and friends Abner, Adrian, Daen, Ivan, Andrey, Thais, Da, Saeid, Daniel, Alex, Wiebke, Vahid, Zoheb, Ankit, Balakumar, Sanjeev, Ashwin, Naveen and so on for their support and happy distractions outside of research to refresh my mind.

Last but not least, I would like to thank my father and my brother for their continuous emotional support throughout the process. I also like to dedicate my honours to my mother, who is unfortunately not with me anymore. I also like to thank my wife Nagashree, who has always been part of this journey and for her immense care and support.

Appendix

Appendix 1 Experimental methods

A1.1 Instruments used for strain analysis

In this section, we attempt to give an overview of the two basic instruments used in this thesis for strain analysis: 1) Transmission electron microscope (TEM) and 2) Confocal micro-Raman spectroscope. Next we will describe the working principle of the instrument and their different modes.

A1.1.1 Transmission electron microscope

A transmission electron microscope (TEM) is one of the electron microscopy tool capable of providing spatial resolution down to the atomic scale. Modern aberration correction TEMs have enabled to visualise individual atomic columns of crystalline materials and have become indispensable for nanoscale research and development. TEM requires special thin samples (<50 nm approximately) called lamellae which are prepared using focussed ion beam (FIB) technology. In general, a beam of electrons passes through a TEM sample and an image is formed after interaction of the electron beam with the sample. The TEM used for the analysis is the Thermosfischer Titan^3 microscope operating at 300 kV high tension or acceleration voltage.

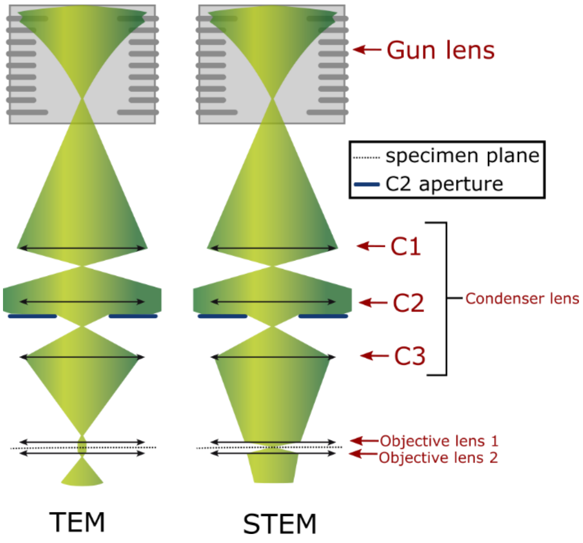

Figure 53 Schematic of TEM opertation in two modes: 1) TEM and 2) STEM

The illumination system of a transmission electron microscope (Figure 53) consists of multiple components namely the gun lens, condenser lenses C1, C2 and C3, minicondenser lens (MC) and objective lenses (obj1 and obj2). There are two primary modes of imaging: 1) parallel illumination for transmission electron imaging (TEM) and 2) probe illumination for scanning transmission electron microscopy imaging (STEM). The functionality of the different illumination lenses is important to understand these imaging modes in TEM and special modalities required for strain measurement techniques like Nanobeam electron diffraction (NBED).

A 1.1.1.1 Gun Lens:

The electron sources commonly used in electron microscopes are based on a thermionic source or field emission or a combination of those. Field emission sources provide more monochromatic electron beam in comparison to thermionic sources. The gun lenses are placed near the electron source and they are used to change the position of the first cross over or the image of the source. Increasing the strength of the gun lens changes the position of the crossover and demagnifies the image of the source and in turn reduces the beam current [157].

A 1.1.1.2 Condenser Lenses C1, C2 and C3:

The crossover between C1 and C2 can also be varied and is called the spot number. This is also used to vary the beam current. Higher spot numbers reduce the beam current and vice versa. A near parallel illumination is preferred in the TEM mode where the sample is illuminated over a wide area. The interaction of the electron beam with the sample is captured by the camera placed below the specimen for the TEM. The sample acts as a thin phase object and the phase changes in the transmitted electron beam gives phase contrast imaging in TEM. The position of the crossover between C2 and C3 can be changed and this changes the diameter of the beam and through this the illuminated area on the sample. C2 and C3 work together to maintain a parallel illumination on the TEM and is taken care of by the software.

The position of the cross over between C2 and C3 is adjusted to change the convergence of the probe in the case of STEM. This in turn affects the magnification. Here, again C2 and C3 act together to maintain the focus of the probe on the sample.

A 1.1.1.3 Objective lens and mini-condenser lens:

The specimen is placed in between the two objective lenses called the upper objective and the lower objective lenses. The upper objective lens is essential in STEM to create a convergent probe; however, it causes difficulties in TEM especially illuminating smaller and larger areas. This is compensated by adding a mini-condenser lens in front of the upper objective lens. The mini-condenser lens increases the illuminated area up to five times in the TEM mode when the mini-condenser lens is on as opposed to when it is off. Similarly, the convergence angles are five times smaller in the probe mode (focussed probe is larger) when the mini-condenser lens is active. The mode of operation in which the mini-condenser lens is 'on' is called the 'microprobe' and when it is 'off' it is called the 'nanoprobe'. Hence, during the normal operation, TEM operates in the microprobe and STEM in the nanoprobe. There are special modes of operation where STEM operates in microprobe with lower convergence angles and near parallel illumination useful for techniques like NBED (section 2.1.2.1).

A1.1.2 Image acquisition in TEM and STEM:

The image of the specimen is projected onto a fluorescent screen or a CCD camera using a system of projection lenses [158]. In TEM, the diffraction pattern is formed on the back focal plane of the lower objective lens. The objective aperture used in this plane permits selected diffracted electron beams to pass through while limiting the others. Bright field imaging is performed by imaging the non-diffracted central beam while dark field imaging is done by blocking the central beam or selecting the high angle diffracted beams.

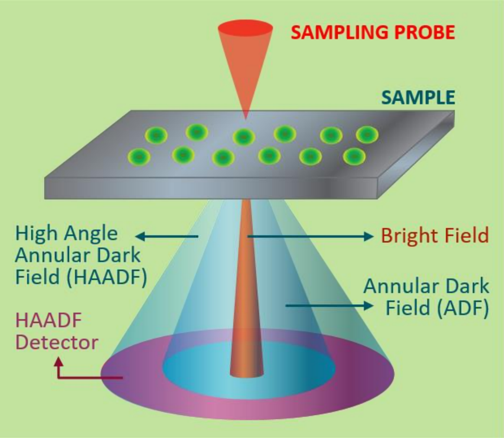

Figure 54 Dark field and bright field imaging detection in STEM

In STEM, an annular detector is placed below the specimen that captures the scattered electrons. The unscattered electrons are captured by a detector placed in the centre as shown in Figure 54. The annular detectors facilitate the Dark field imaging in STEM. The high angle annular dark field (HAADF) detector images incoherently scattered electrons and the contrast is directly proportional to the atomic number z^n (with n very close to 2) of the elements and hence is also called z-contrast imaging [159]. The technique is highly sensitive to the variation in the atomic number and is also suitable for imaging slightly thicker samples (~ 200 nm) in comparison to TEM imaging (~50 nm) [160]. The high angle scattered electrons are Rutherford scattered and undergo elastic scattering. The scattering is linked predominantly to electron-nucleus interaction and are mostly incoherent.

A1.2 Micro-Raman spectroscopy

Raman spectroscopy is a very powerful tool to characterize a variety of material parameters like for instance mechanical stress in crystalline materials. It is used primarily to study the vibrational energy levels in a crystal using laser light as an excitation source. Raman spectroscopy in combination with confocal optical microscope has enabled increased spatial resolution upto a micrometer [161]. The micro-Raman spectroscopy for our experiments are conducted using Labram HR from HORIBA.

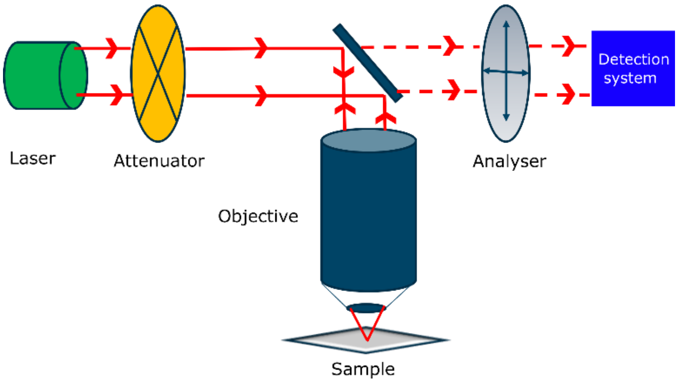

Figure 55 Basic schematic of the micro-Raman setup

Figure 55 shows the basic schematic of the micro-Raman spectroscopy. A linearly polarised He-Ne laser light is used with a wavelength of ~633 nm. An attenuator is used to limit the intensity of the incoming laser, in order to mitigate the shift in wavenumber of detected phonons from the sample due to temperature variations induced by the laser [162]. The laser is focussed on the specimen using a high numerical-aperture (NA) objective lens. The Raman scattered light is collected by the same objective lens that is operating in the backscattering configuration. An analyser is used in the outgoing path to collect particular polarisation of the Raman scattered light. Since, Raman spectroscopy is dependent on the polarisation of incoming and outgoing light, the analyser selects particular phonon modes of interest. The detection system consists of a monochromator (usually a diffraction grating) that disperses the collected radiation onto a CCD camera detector, which allows detection of a large spectral range [163].

Appendix 2 Samples

A2.1 Blanket/test structure

The blanket/test structure consists of a thick $Si_{0.3}Ge_{0.7}$ layer (~200 nm) grown on a Si substrate (Figure 56). The $Si_{0.3}Ge_{0.7}$ layer is expected to be completely relaxed and acts as a strain relaxed buffer (SRB). A theoretical study by Dah-Min and David Hwang [11] on the relaxation of epitaxially grown materials shows that above a "critical thickness" the epitaxially strained material relaxes by the formation of misfits and dislocations near the interface. For the specific case of $Si_{0.3}Ge_{0.7}$ on top of Si with misfits ~3% the critical thickness is ~30-60 nm; and for the blanket sample with $Si_{0.3}Ge_{0.7}$ layer ~200nm, one can expect a complete relaxation of the layer. A thin layer of Ge (~27 nm) is epitaxially grown on top of the SRB and is expected to be compressively biaxially strained due to the lattice mismatch between $Si_{0.3}Ge_{0.7}$ and Ge.

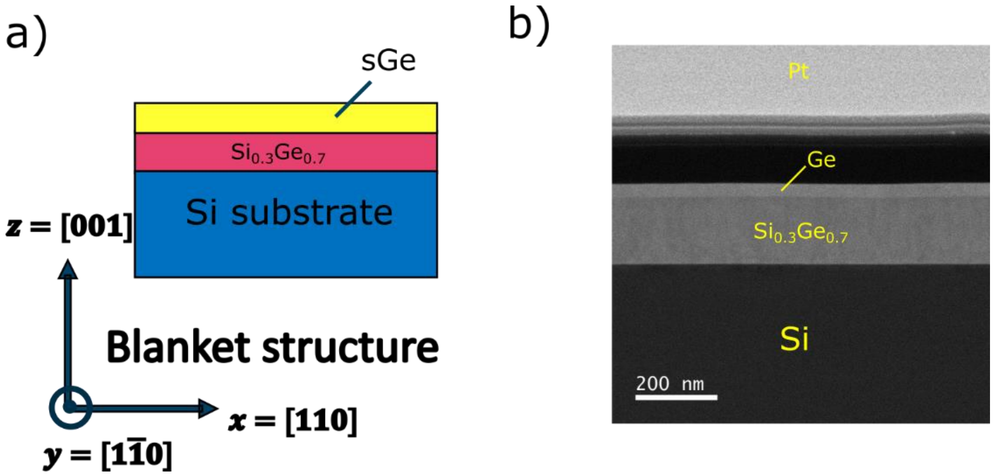

Figure 56 a) Schematic of the blanket/test structure b) cross sectional TEM sample showing the different layers of the blanket structure

A2.2 Ge on Si TEM sample

Figure 57 shows the TEM lamella of Ge on top of Si substrate. The Ge layer is ~500 nm in thickness. The critical thickness for strain relaxation of the Ge layer epitaxially grown on Si (~4 % lattice mismatch) is ~10-50 nm [11]. Due to the very high thickness of the Ge layer, we can expect complete relaxation of the layer with the formation of misfit dislocations near the interface. This relaxed or unstrained sample system is used to assess the accuracy of various TEM techniques throughout the thesis.

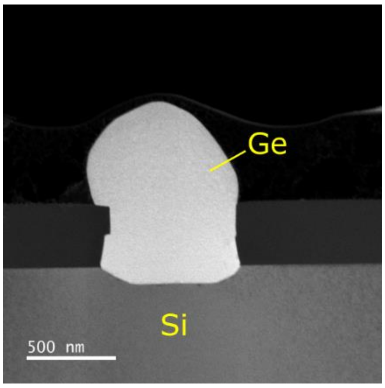

Figure 57 TEM lamella of Ge on top of Si substrate

Appendix 3 Tomography sample holder

Tomography needle shaped sample is attached to a TEM grid and mounted on a Fischione 2040 holder (Figure 58).

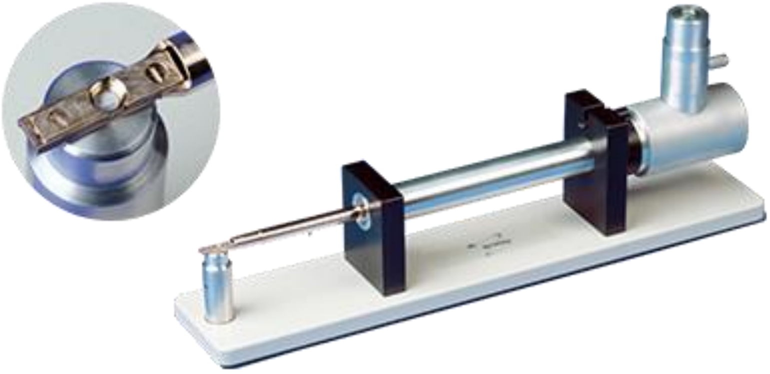

Figure 58 Fischione 2040 dual axis tomography holder © Fischione Instruments

The dual axis tomography holder provides a tilt range of ± 70°. This is beneficial to reduce the effects of missing wedge in the reconstruction. It also features an inplane rotation, up to 360°. This dual axis mechanism allows for precise orientation of the sample along the zone axis which is essential for high/atomic resolution tomography. A flexiClamp spring type clamping mechanism secures the specimen/grid onto the specimen cup while also maximising the specimen visibility at higher tilt angles. Unfortunately, the clamping mechanism induces a slight bending of the grid when using conventional copper grids, which can induce precession motion instead of pure tilt during tomography series acquisition. Hence, molybdenum grids are used for our experiment which proved to be much stiffer and resistant towards bending.

Appendix 4 Asymmetric function for SiGe Raman spectrum fitting

The asymmetric function I as a function of the peak position ω in [cm^{-1}] is given by

$$I(\omega) = \frac{1}{2}\frac{[1\ -\ sign\ (\omega - \omega_0)\ I_0]}{\left(\frac{\omega - \omega_0}{W_1}\right)^2\ +\ 1} + \frac{1}{2}\frac{[1\ -\ sign\ (\omega - \omega_0)\ I_0]}{\left(\frac{\omega_0 - \omega}{W_2}\right)^2\ +\ 1}$$

Where, I_0 is the peak intensity, W_1 and W_2 are the HWHM (half-width at hald maximum) at the low frequency and high frequency side, ω_0 is the peak position and $sign$ is the signum function of a real number.

Appendix 5 Conversion from lattice mismatch to strain

The TEM strain measurements operate by measuring the lattice mismatch between a strained material and a reference material (usually Si substrate for semiconductors). So the lattice mismatch between strained material (mat) and any reference material (sub) is given by:

$$\varepsilon_{mat-sub} = \frac{a_{mat} - a_{sub}}{a_{sub}} \tag{82}$$

Where, a_{xx} is the lattice parameter of the material xx.

Now, the strain with respect to the bulk unstrained material is given by:

$$\varepsilon_{mat-bulk} = \frac{a_{mat} - a_{bulk}}{a_{bulk}} \tag{83}$$

From eqs. 82-83, we can deduce the conversion, i.e.,

$$\varepsilon_{mat-bulk} = \frac{a_{sub}}{a_{bulk}}(1 + \varepsilon_{mat-sub}) - 1 \tag{84}$$

Hence, eq.84 gives conversion from the measured lattice mismatch from TEM $\varepsilon_{mat-sub}$ to strain with respect to the bulk unstrained material. The lattice parameter of the materials under consideration can vary depending on the directions in the crystal coordinate system. For example, $a_{Si[110]} = 0.384\ nm$ and $a_{Si[100]} = 0.543\ nm$.

Appendix 6 Moiré technique experimental sampling frequency determination

Determining the experimental sampling frequency is crucial for the accuracte determination of the amplification-factor and thus the overall strain measurement. The determination is straightforward and is explained in detail below.

The digital frequency ($Spatial\ frequency\ of\ the\ crystal/Sampling\ frequency$) for the moiré technique is given by eq.34, i.e.,

$$g_{ref,m} = \frac{g_{ref}}{f_m} - n \tag{85}$$

Where, $g_{ref} = \frac{1}{a_{ref}}$ is the spatial frequency of the reference material (usually Si substrate), f_m is the experimental sampling frequency and n is the moiré window from which the frequency is being translated. Now, a_{ref} and n are known and the task now remains to calculate $g_{ref,m}$, and $g_{ref,m}$ can be calculated from the FT of the experimental moiré image which further enables the direct determination of the experimental sampling frequency f_m.

The example below, shows the calculation of $g_{ref,m}$ from a hypothetical FT consisting of a single frequency/reflection centered at (g_u, g_v).

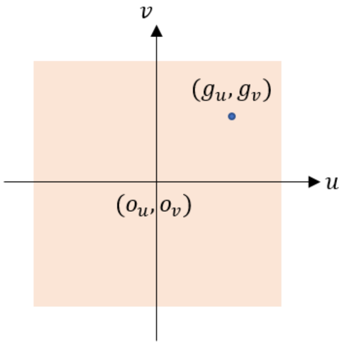

Figure 59 A hypothetical FT

$g_{ref,m}$ is now calculated as:

$$g_{ref,m}(u, v) = \left(\frac{g_u - o_u}{N}, \frac{g_v - o_v}{N}\right) \tag{86}$$

where, N is the number of pixels in the image. Using eq.86, it is now straight-forward to calculate the experimental f_m and subsequently calculate the experimental amplification-factor $\alpha = \frac{1}{1-\frac{nf_m}{g_{ref}}}$.

Scientific contributions

Journal articles

1) V. Prabhakara, D. Jannis, A. Béché, H. Bender, J. Verbeeck, Strain measurement in semiconductor FinFET devices using a novel moiré demodulation technique, Semicond. Sci. Technol. 35 (2020) 34002. https://doi.org/10.1088/1361-6641/ab5da2.

2) V. Prabhakara, D. Jannis, G. Guzzinati, A. Béché, H. Bender, J. Verbeeck, HAADF-STEM block-scanning strategy for local measurement of strain at the nanoscale, Ultramicroscopy. 219 (2020) 113099. https://doi.org/10.1016/j.ultramic.2020.113099.

3) V. Prabhakara, T. Nuytten, H. Bender, W. Vandervorst, S. bals and J. Verbeeck, “Linearized radially polarised light for improved precision in strain measurements using micro-Raman spectroscopy” [Optics Express https://doi.org/10.1364/OE.434726]

Oral presentations

1) “Advanced moiré strain measurement technique using smart scanning strategies”, The 21st International Conference on Microscopy of Semiconducting Materials (MSM-XXI)" organized in Cambridge, UK (April 2019)

2) “TEM strain analysis in semiconductor Nanodevices”, EMAT Friday lecture, Antwerp (June 2018)

3) “Strain measurement techniques in Si-Ge semiconductor devices”, IMEC strategic day (November 2019)

4) “TEM strain measurement techniques in Si-Ge semiconductor materials”, EMAT Friday lecture, Antwerp (June 2021)

Poster presentations

1) “Strain measurement techniques in SiGe semiconductor nanodevices” - 2nd Summer School on Defects in Semiconductors ,University of Ghent, Belgium, Sep 2018.

2) “Strain measurement in Semiconductor FinFET devices using Moiré and a novel quadrature demodulation technique” - RBSM meeting 2019, Louvain-la-neuve, Belgium, September 2019.

3) “Strain measurement in Semiconductor FinFET devices using Moiré and a novel quadrature demodulation technique” - WOG meeting on Image Reconstruction, Ghent, Belgium, September 2019.

4) “HAADF STEM block scanning strategy for the nanoscale measurement of strain in semiconductor FinFETs” – EMAT poster session (Virtual), October 2020.

References

1. G. E. Moore, "Progress in digital integrated electronics [Technical literaiture, Copyright 1975 IEEE. Reprinted, with permission. Technical Digest. International Electron Devices Meeting, IEEE, 1975, pp. 11-13.]," IEEE Solid-State Circuits Soc. Newsl. **11**(3), 36–37 (2006).
2. Jin Ju Kim, Minwoo Kim, Ukjin Jung, Kyung Eun Chang, Sangkyung Lee, Yonghun Kim, Young Gon Lee, Rino Choi, and Byoung Hun Lee, "Intrinsic Time Zero Dielectric Breakdown Characteristics of HfAlO Alloys," IEEE Trans. Electron Devices **60**(11), 3683–3689 (2013).
3. B. Majkusiak, "Gate tunnel current in an MOS transistors," IEEE Trans. Electron Devices **37**(4), 1087–1092 (1990).
4. J. Qu, H. Zhang, X. Xu, and S. Qin, "Study of Drain Induced Barrier Lowering(DIBL) Effect for Strained Si nMOSFET," Procedia Eng. **16**, 298–305 (2011).
5. C. H. Lee, J. M. Yoon, C. Lee, H. M. Yang, K. N. Kim, T. Y. Kim, H. S. Kang, Y. J. Ahn, Donggun Park, and Kinam Kim, "Novel body tied FinFET cell array transistor DRAM with negative word line operation for sub 60nm technology and beyond," in *Digest of Technical Papers. 2004 Symposium on VLSI Technology, 2004.* (IEEE, 2004), pp. 130–131.
6. G. Sudo, "LOCOS on SOI and HOT semiconductor device and method for manufacturing," U.S. patent US20070262392A1 (2007).
7. P. R. Chidambaram, C. Bowen, S. Chakravarthi, C. Machala, and R. Wise, "Fundamentals of silicon material properties for successful exploitation of strain engineering in modern CMOS manufacturing," IEEE Trans. Electron Devices **53**(5), 944–964 (2006).
8. I. De Wolf, H. E. Maes, and Y. Kevin, "Raman spectroscopy measurement of local stress induced by LOCOS and trench structures in the silicon substrate," in (1993), pp. 565–568.
9. I. De Wolf, R. Rooyackers, and H. E. Maes, "Stress variation across arrays of lines and its influence on LOCOS oxidation," Microelectron. Eng. **28**(1–4), 79–82 (1995).
10. A. Sharma, M. Goswami, and B. R. Singh, "Optimization and Stress Analysis of Local Oxidation of Silicon (LOCOS) Process for Isolation," in *2013 International Conference on Communication Systems and Network Technologies* (IEEE, 2013), pp. 736–740.
11. D.-M. D. Hwang, "Strain relaxation in lattice-mismatched epitaxy," Mater. Chem. Phys. **40**(4), 291–297 (1995).
12. S. E. Thompson, Guangyu Sun, Youn Sung Choi, and T. Nishida, "Uniaxial-process-induced strained-Si: extending the CMOS roadmap," IEEE Trans. Electron Devices **53**(5), 1010–1020 (2006).
13. K. Rim, K. Chan, L. Shi, D. Boyd, J. Ott, N. Klymko, F. Cardone, L. Tai, S. Koester, M. Cobb, D. Canaperi, B. To, E. Duch, I. Babich, R. Carruthers, P. Saunders, G. Walker, Y. Zhang, M. Steen, and M. Ieong, "Fabrication and mobility characteristics of ultra-thin strained Si directly on insulator (SSDOI) MOSFETs," in *IEEE International Electron Devices Meeting 2003* (IEEE, 2003), p. 3.1.1-3.1.4.
14. M. Glicksman, "Magnetoresistance of Germanium-Silicon Alloys," Phys. Rev. **100**(4), 1146–1147 (1955).
15. E. Kasper, H. J. Herzog, and H. Kibbel, "A one-dimensional SiGe superlattice grown by UHV epitaxy," Appl. Phys. **8**(3), 199–205 (1975).
16. G. C. Osbourn, "Strained-layer superlattices from lattice mismatched materials," J. Appl. Phys. **53**(3), 1586–1589 (1982).
17. S. E. Thompson, M. Armstrong, C. Auth, S. Cea, R. Chau, G. Glass, T. Hoffman, J. Klaus, Z. Ma, B. Mcintyre, A. Murthy, B. Obradovic, L. Shifren, S. Sivakumar, S. Tyagi, T. Ghani, K. Mistry, M. Bohr, and Y. El-Mansy, "A Logic Nanotechnology Featuring Strained-Silicon," IEEE Electron Device Lett. **25**(4), 191–193 (2004).
18. K. Rim, J. Welser, J. L. Hoyt, and J. F. Gibbons, "Enhanced hole mobilities in surface-channel strained-Si p-MOSFETs," in *Proceedings of International Electron Devices Meeting* (IEEE, 1995), pp. 517–520.

19. T. Tezuka, S. Nakaharai, Y. Moriyama, N. Sugiyama, and S. Takagi, "High-mobility strained SiGe-on-insulator pMOSFETs with Ge-rich surface channels fabricated by local condensation technique," IEEE Electron Device Lett. **26**(4), 243–245 (2005).
20. Y. Sun, S. E. Thompson, and T. Nishida, "Physics of strain effects in semiconductors and metal-oxide-semiconductor field-effect transistors," J. Appl. Phys. **101**(10), 104503 (2007).
21. G. SUN, "STRAIN EFFECTS ON HOLE MOBILITY OF SILICON AND GERMANIUM P-TYPE METAL-OXIDE-SEMICONDUCTOR FIELD-EFFECT-TRANSISTORS," PhD Thesis, UNIVERSITY OF FLORIDA (2007).
22. S. Kim, S. Lee, Y. Oshima, Y. Kondo, E. Okunishi, N. Endo, J. Jung, G. Byun, S. Lee, and K. Lee, "Scanning moiré fringe imaging for quantitative strain mapping in semiconductor devices," Appl. Phys. Lett. **102**(16), 161604 (2013).
23. A. Ishizuka, M. Hytch, and K. Ishizuka, "STEM moiré analysis for 2D strain measurements," J. Electron Microsc. (Tokyo) **66**(3), 217–221 (2017).
24. A. Pofelski, S. Y. Woo, B. H. Le, X. Liu, S. Zhao, Z. Mi, S. Löffler, and G. A. Botton, "2D strain mapping using scanning transmission electron microscopy Moiré interferometry and geometrical phase analysis," Ultramicroscopy **187**, 1–12 (2018).
25. M. J. Hÿtch, F. Houdellier, F. Hüe, and E. Snoeck, "Dark-field electron holography for the measurement of geometric phase," Ultramicroscopy **111**(8), 1328–1337 (2011).
26. A. Béché, J. L. Rouvière, J. P. Barnes, and D. Cooper, "Strain measurement at the nanoscale: Comparison between convergent beam electron diffraction, nano-beam electron diffraction, high resolution imaging and dark field electron holography," Ultramicroscopy **131**, 10–23 (2013).
27. A. Armigliato, A. Spessot, R. Balboni, A. Benedetti, G. Carnevale, S. Frabboni, G. Mastracchio, and G. Pavia, "Convergent beam electron diffraction investigation of strain induced by Ti self-aligned silicides in shallow trench Si isolation structures," J. Appl. Phys. **99**(6), 064504 (2006).
28. A. Béché, L. Clément, and J.-L. Rouvière, "Improved accuracy in nano beam electron diffraction," J. Phys. Conf. Ser. **209**, 012063 (2010).
29. P. Favia, M. Bargallo Gonzales, E. Simoen, P. Verheyen, D. Klenov, and H. Bender, "Nanobeam Diffraction: Technique Evaluation and Strain Measurement on Complementary Metal Oxide Semiconductor Devices," J. Electrochem. Soc. **158**(4), H438 (2011).
30. L. Bruas, V. Boureau, A. P. Conlan, S. Martinie, J.-L. Rouviere, and D. Cooper, "Improved measurement of electric fields by nanobeam precession electron diffraction," J. Appl. Phys. **127**(20), 205703 (2020).
31. J.-L. Rouviere, A. Béché, Y. Martin, T. Denneulin, and D. Cooper, "Improved strain precision with high spatial resolution using nanobeam precession electron diffraction," Appl. Phys. Lett. **103**(24), 241913 (2013).
32. A. S. Eggeman and P. A. Midgley, "Precession Electron Diffraction," in *Advances in Imaging and Electron Physics* (Elsevier, 2012), **170**, pp. 1–63.
33. G. Guzzinati, W. Ghielens, C. Mahr, A. Béché, A. Rosenauer, T. Calders, and J. Verbeeck, "Electron Bessel beam diffraction for precise and accurate nanoscale strain mapping," Appl. Phys. Lett. **114**(24), 243501 (2019).
34. F. Pezzoli, E. Bonera, E. Grilli, M. Guzzi, S. Sanguinetti, D. Chrastina, G. Isella, H. von Känel, E. Wintersberger, J. Stangl, and G. Bauer, "Raman spectroscopy determination of composition and strain in heterostructures," Mater. Sci. Semicond. Process. **11**(5–6), 279–284 (2008).
35. I. De Wolf, "Relation between Raman frequency and triaxial stress in Si for surface and cross-sectional experiments in microelectronics components," J. Appl. Phys. **118**(5), 053101 (2015).
36. T. Nuytten, J. Bogdanowicz, L. Witters, G. Eneman, T. Hantschel, A. Schulze, P. Favia, H. Bender, I. De Wolf, and W. Vandervorst, "Anisotropic stress in narrow sGe fin field-effect transistor channels measured using nano-focused Raman spectroscopy," APL Mater. **6**(5), 058501 (2018).
37. M. Hÿtch, F. Houdellier, F. Hüe, and E. Snoeck, "Nanoscale holographic interferometry for strain measurements in electronic devices," Nature **453**(7198), 1086–1089 (2008).
38. Y.-C. Yeo and J. Sun, "Finite-element study of strain distribution in transistor with silicon–germanium source and drain regions," Appl. Phys. Lett. **86**(2), 023103 (2005).

39. J.-L. Rouviere, L. Clement, and R. Pantel, "Method for measuring physical parameters of at least one micrometric or nanometric dimensional phase in a composite system," U.S. patent WO2005010479 (n.d.).
40. Yu. V. Milman, I. V. Gridneva, and A. A. Golubenko, "Construction of stess-strain curves for brittle materials by indentation in a wide temperature range," Sci. Sinter. **39**(1), 67–75 (2007).
41. M. A. Slawinski, ed., "Chapter 3 - Stress-strain equations," in *Seismic Waves and Rays in Elastic Media*, Handbook of Geophysical Exploration: Seismic Exploration (Pergamon, 2003), **34**, pp. 61–68.
42. M. A. Slawinski, ed., "Chapter 4 - Strain energy," in *Seismic Waves and Rays in Elastic Media*, Handbook of Geophysical Exploration: Seismic Exploration (Pergamon, 2003), **34**, pp. 69–84.
43. L. Zhang, R. Barrett, P. Cloetens, C. Detlefs, and M. Sanchez del Rio, "Anisotropic elasticity of silicon and its application to the modelling of X-ray optics," J. Synchrotron Radiat. **21**(3), 507–517 (2014).
44. V. Giurgiutiu, "Fundamentals of Aerospace Composite Materials," in *Structural Health Monitoring of Aerospace Composites* (Elsevier, 2016), pp. 25–65.
45. R. S. Pal, S. Sharma, and S. Dasgupta, "Recent trend of FinFET devices and its challenges: A review," in *2017 Conference on Emerging Devices and Smart Systems (ICEDSS)* (IEEE, 2017), pp. 150–154.
46. R. Loo, A. Y. Hikavyy, L. Witters, A. Schulze, H. Arimura, D. Cott, J. Mitard, C. Porret, H. Mertens, P. Ryan, J. Wall, K. Matney, M. Wormington, P. Favia, O. Richard, H. Bender, A. Thean, N. Horiguchi, D. Mocuta, and N. Collaert, "Processing Technologies for Advanced Ge Devices," ECS J. Solid State Sci. Technol. **6**(1), P14–P20 (2017).
47. I. De Wolf, V. Simons, V. Cherman, R. Labie, B. Vandevelde, and E. Beyne, "In-depth Raman spectroscopy analysis of various parameters affecting the mechanical stress near the surface and bulk of Cu-TSVs," in *2012 IEEE 62nd Electronic Components and Technology Conference* (IEEE, 2012), pp. 331–337.
48. S. Di Fonzo, W. Jark, S. Lagomarsino, C. Giannini, L. De Caro, A. Cedola, and M. Müller, "Non-destructive determination of local strain with 100-nanometre spatial resolution," Nature **403**(6770), 638–640 (2000).
49. "Imec and Cadence Tape Out Industry’s First 3nm Test Chip," (n.d.).
50. B. Berkels, P. Binev, D. A. Blom, W. Dahmen, R. C. Sharpley, and T. Vogt, "Optimized imaging using non-rigid registration," Ultramicroscopy **138**, 46–56 (2014).
51. M. J. Hÿtch, E. Snoeck, and R. Kilaas, "Quantitative measurement of displacement and strain fields from HREM micrographs," Ultramicroscopy **74**(3), 131–146 (1998).
52. E. Guerrero, P. L. Galindo, A. Yáñez, J. Pizarro, M. P. Guerrero-Lebrero, and S. I. Molina, "Accuracy assessment of strain mapping from Z-contrast images of strained nanostructures," Appl. Phys. Lett. **95**(14), 143126 (2009).
53. D. Cooper, T. Denneulin, N. Bernier, A. Béché, and J.-L. Rouvière, "Strain mapping of semiconductor specimens with nm-scale resolution in a transmission electron microscope," Micron **80**, 145–165 (2016).
54. A. Béché, J. L. Rouvière, J. P. Barnes, and D. Cooper, "Dark field electron holography for strain measurement," Ultramicroscopy **111**(3), 227–238 (2011).
55. D. Cooper, J.-P. Barnes, J.-M. Hartmann, A. Béché, and J.-L. Rouviere, "Dark field electron holography for quantitative strain measurements with nanometer-scale spatial resolution," Appl. Phys. Lett. **95**(5), 053501 (2009).
56. R. E. Blahut, "Information Theory and Coding," in *Reference Data for Engineers* (Elsevier, 2002), pp. 25-1-25–31.
57. M. S’ari, J. Cattle, N. Hondow, R. Brydson, and A. Brown, "Low dose scanning transmission electron microscopy of organic crystals by scanning moiré fringes," Micron **120**, 1–9 (2019).
58. A. B. Naden, K. J. O’Shea, and D. A. MacLaren, "Evaluation of crystallographic strain, rotation and defects in functional oxides by the moiré effect in scanning transmission electron microscopy," Nanotechnology **29**(16), 165704 (2018).
59. N. Endo and Y. Kondo, "Strain Analysis of Semiconductor Device by Moiré Fringes in STEM Image," Microsc. Microanal. **19**(S2), 346–347 (2013).

60. N. Endo and Y. Kondo, "Accuracy of Strain in Strain Maps Improved by Averaging Multiple Maps," Microsc. Microanal. **20**(S3), 1068–1069 (2014).
61. C. Mahr, K. Müller-Caspary, T. Grieb, M. Schowalter, T. Mehrtens, F. F. Krause, D. Zillmann, and A. Rosenauer, "Theoretical study of precision and accuracy of strain analysis by nano-beam electron diffraction," Ultramicroscopy **158**, 38–48 (2015).
62. A. Béché, J. L. Rouvière, L. Clément, and J. M. Hartmann, "Improved precision in strain measurement using nanobeam electron diffraction," Appl. Phys. Lett. **95**(12), 123114 (2009).
63. D. B. Williams and C. B. Carter, "Elastic Scattering," in *Transmission Electron Microscopy* (Springer US, 2009), pp. 39–51.
64. K. Müller, A. Rosenauer, M. Schowalter, J. Zweck, R. Fritz, and K. Volz, "Strain Measurement in Semiconductor Heterostructures by Scanning Transmission Electron Microscopy," Microsc. Microanal. **18**(5), 995–1009 (2012).
65. J. P. Morniroli, F. Houdellier, C. Roucau, J. Puiggalí, S. Gestí, and A. Redjaïmia, "LACDIF, a new electron diffraction technique obtained with the LACBED configuration and a Cs corrector: Comparison with electron precession," Ultramicroscopy **108**(2), 100–115 (2008).
66. J.-L. Rouviere, "METHOD TO FACILITATE POSITIONING OF DFFRACTION SPOTS," U.S. patent US 2013/0206968 A1 (August 15, 2013).
67. V. Grillo, J. Harris, G. C. Gazzadi, R. Balboni, E. Mafakheri, M. R. Dennis, S. Frabboni, R. W. Boyd, and E. Karimi, "Generation and application of bessel beams in electron microscopy," Ultramicroscopy **166**, 48–60 (2016).
68. K. Saitoh, K. Hirakawa, H. Nambu, N. Tanaka, and M. Uchida, "Generation of Electron Bessel Beams with Nondiffractive Spreading by a Nanofabricated Annular Slit," J. Phys. Soc. Jpn. **85**(4), 043501 (2016).
69. G. Guzzinati, Wannes Ghielens, C. Mahr, A. Béché, A. Rosenauer, T. Calders, and J. Verbeeck, "Electron Bessel beam diffraction patterns, line scan of Si/SiGe multilayer," (2019).
70. W. Ghielens, G. Guzzinati, and T. Calders, *TEM Strain Calculation* (2019).
71. V. Prabhakara, D. Jannis, A. Béché, H. Bender, and J. Verbeeck, "Strain measurement in semiconductor FinFET devices using a novel moiré demodulation technique," Semicond. Sci. Technol. **35**(3), 034002 (2020).
72. X. Qu and Q. Deng, "Damage and recovery induced by a high energy e-beam in a silicon nanofilm," RSC Adv. **7**(59), 37032–37038 (2017).
73. G. H. Loechelt, N. G. Cave, and J. Menéndez, "Polarized off-axis Raman spectroscopy: A technique for measuring stress tensors in semiconductors," J. Appl. Phys. **86**(11), 6164–6180 (1999).
74. A. Tarun, N. Hayazawa, H. Ishitobi, S. Kawata, M. Reiche, and O. Moutanabbir, "Mapping the “Forbidden” Transverse-Optical Phonon in Single Strained Silicon (100) Nanowire," Nano Lett. **11**(11), 4780–4788 (2011).
75. A. Gawlik, J. Bogdanowicz, T. Nuytten, A.-L. Charley, L. Teugels, J. Misiewicz, and W. Vandervorst, "Critical dimension metrology using Raman spectroscopy," Appl. Phys. Lett. **117**(4), 043102 (2020).
76. A. Gawlik, J. Bogdanowicz, A. Schulze, J. Misiewicz, and W. Vandervorst, "Photonic properties of periodic arrays of nanoscale Si fins," in *Photonic and Phononic Properties of Engineered Nanostructures IX*, A. Adibi, S.-Y. Lin, and A. Scherer, eds. (SPIE, 2019), p. 76.
77. T. Nuytten, J. Bogdanowicz, T. Hantschel, A. Schulze, P. Favia, H. Bender, I. De Wolf, and W. Vandervorst, "Advanced Raman Spectroscopy Using Nanofocusing of Light: Advanced Raman Spectroscopy Using Nanofocusing…," Adv. Eng. Mater. **19**(8), 1600612 (2017).
78. V. Poborchii, T. Tada, and T. Kanayama, "Enhancement of the Strained Si Forbidden Doublet Transverse Optical Phonon Raman Band for Quantitative Stress Measurement," Jpn. J. Appl. Phys. **51**, 078002 (2012).
79. A. Pofelski, S. Ghanad-Tavakoli, D. A. Thompson, and G. A. Botton, "Sampling optimization of Moiré geometrical phase analysis for strain characterization in scanning transmission electron microscopy," Ultramicroscopy **209**, 112858 (2020).
80. E. McCune, *Practical Digital Wireless Signals*, The Cambridge RF and Microwave Engineering Series (Cambridge University Press, 2010).

81. A. Zobelli, S. Y. Woo, A. Tararan, L. H. G. Tizei, N. Brun, X. Li, O. Stéphan, M. Kociak, and M. Tencé, "Spatial and spectral dynamics in STEM hyperspectral imaging using random scan patterns," Ultramicroscopy **212**, 112912 (2020).
82. "Attolight," https://attolight.com/.
83. P. Thakur, *Advanced Reservoir and Production Engineering for Coal Bed Methane* (Gulf Professional Publishing is an imprint of Elsevier, 2017).
84. N. Cherkashin, T. Denneulin, and M. J. Hÿtch, "Electron microscopy by specimen design: application to strain measurements," Sci. Rep. **7**(1), 12394 (2017).
85. P. Jin and X. Li, "Correction of image drift and distortion in a scanning electron microscopy: CORRECTION FOR DISTORTION IN SEM," J. Microsc. **260**(3), 268–280 (2015).
86. R. J. I. Marks, *Introduction to Shannon Sampling and Interpolation Theory.* (Springer, 2012).
87. L. Jones and P. D. Nellist, "Identifying and Correcting Scan Noise and Drift in the Scanning Transmission Electron Microscope," Microsc. Microanal. **19**(4), 1050–1060 (2013).
88. X. Sang and J. M. LeBeau, "Revolving scanning transmission electron microscopy: Correcting sample drift distortion without prior knowledge," Ultramicroscopy **138**, 28–35 (2014).
89. X. Sang, A. R. Lupini, R. R. Unocic, M. Chi, A. Y. Borisevich, S. V. Kalinin, E. Endeve, R. K. Archibald, and S. Jesse, "Dynamic scan control in STEM: spiral scans," Adv. Struct. Chem. Imaging **2**(1), 6 (2016).
90. C. Ophus, J. Ciston, and C. T. Nelson, "Correcting nonlinear drift distortion of scanning probe and scanning transmission electron microscopies from image pairs with orthogonal scan directions," Ultramicroscopy **162**, 1–9 (2016).
91. W. H. Press, ed., *Numerical Recipes: The Art of Scientific Computing*, 3rd ed (Cambridge University Press, 2007).
92. S. Bals, W. Albrecht, H. Vanrompay, E. Bladt, A. Skorikov, T. M. De Oliveira, N. Winckelmans, J.-W. Buurlage, D. Pelt, K. J. Batenburg, and S. Van Aert, "Novel Approaches for Electron Tomography to Investigate the Structure and Stability of Nanomaterials in 3 Dimensions.," Microsc. Microanal. **26**(S2), 1128–1130 (2020).
93. T. Altantzis, I. Lobato, A. De Backer, A. Béché, Y. Zhang, S. Basak, M. Porcu, Q. Xu, A. Sánchez-Iglesias, L. M. Liz-Marzán, G. Van Tendeloo, S. Van Aert, and S. Bals, "Three-Dimensional Quantification of the Facet Evolution of Pt Nanoparticles in a Variable Gaseous Environment," Nano Lett. **19**(1), 477–481 (2019).
94. P. A. Midgley and M. Weyland, "3D electron microscopy in the physical sciences: the development of Z-contrast and EFTEM tomography," Ultramicroscopy **96**(3–4), 413–431 (2003).
95. S. Bals, S. Van Aert, and G. Van Tendeloo, "High resolution electron tomography," Curr. Opin. Solid State Mater. Sci. **17**(3), 107–114 (2013).
96. J. Frank, *Electron Tomography: Methods for Three-Dimensional Visualization of Structures in the Cell* (Springer, 2006).
97. B. Fultz and J. Howe, "Diffraction Contrast in TEM Images," in *Transmission Electron Microscopy and Diffractometry of Materials*, Graduate Texts in Physics (Springer Berlin Heidelberg, 2013), pp. 349–427.
98. R. K. Leary and P. A. Midgley, "Electron Tomography in Materials Science," in *Springer Handbook of Microscopy*, P. W. Hawkes and J. C. H. Spence, eds., Springer Handbooks (Springer International Publishing, 2019), pp. 1279–1329.
99. B. Martins, S. Sorrentino, W.-L. Chung, M. Tatli, O. Medalia, and M. Eibauer, "Unveiling the polarity of actin filaments by cryo-electron tomography," Structure **29**(5), 488-498.e4 (2021).
100. H. Vanrompay, A. Skorikov, E. Bladt, A. Béché, B. Freitag, J. Verbeeck, and S. Bals, "Fast versus conventional HAADF-STEM tomography of nanoparticles: advantages and challenges," Ultramicroscopy **221**, 113191 (2021).
101. A. Skorikov, W. Albrecht, E. Bladt, X. Xie, J. E. S. van der Hoeven, A. van Blaaderen, S. Van Aert, and S. Bals, "Quantitative 3D Characterization of Elemental Diffusion Dynamics in Individual Ag@Au Nanoparticles with Different Shapes," ACS Nano **13**(11), 13421–13429 (2019).

102. J. C. Hernández-Garrido, M. S. Moreno, C. Ducati, L. A. Pérez, P. A. Midgley, and E. A. Coronado, "Exploring the benefits of electron tomography to characterize the precise morphology of core–shell Au@Ag nanoparticles and its implications on their plasmonic properties," Nanoscale **6**(21), 12696–12702 (2014).
103. S. Bals, M. Casavola, M. A. van Huis, S. Van Aert, K. J. Batenburg, G. Van Tendeloo, and D. Vanmaekelbergh, "Three-Dimensional Atomic Imaging of Colloidal Core–Shell Nanocrystals," Nano Lett. **11**(8), 3420–3424 (2011).
104. J. Radon, "Uber die bestimmung von funktionen durch ihre integralwerte langs gewisser mannigfaltigkeiten.," J. Math. Phys. **69**, 262–277 (1917).
105. T. Özge Onur, "An application of filtered back projection method for computed tomography images," Int. Rev. Appl. Sci. Eng. **12**(2), 194–200 (2021).
106. H. Heidari Mezerji, W. Van den Broek, and S. Bals, "A practical method to determine the effective resolution in incoherent experimental electron tomography," Ultramicroscopy **111**(5), 330–336 (2011).
107. R. Gordon, R. Bender, and G. T. Herman, "Algebraic Reconstruction Techniques (ART) for three-dimensional electron microscopy and X-ray photography," J. Theor. Biol. **29**(3), 471–481 (1970).
108. S. Kaczmarz, "Approximate solution of systems of linear equations†," Int. J. Control **57**(6), 1269–1271 (1993).
109. P. Gilbert, "Iterative methods for the three-dimensional reconstruction of an object from projections," J. Theor. Biol. **36**(1), 105–117 (1972).
110. W. van Aarle, W. J. Palenstijn, J. De Beenhouwer, T. Altantzis, S. Bals, K. J. Batenburg, and J. Sijbers, "The ASTRA Toolbox: A platform for advanced algorithm development in electron tomography," Ultramicroscopy **157**, 35–47 (2015).
111. W. van Aarle, W. J. Palenstijn, J. Cant, E. Janssens, F. Bleichrodt, A. Dabravolski, J. De Beenhouwer, K. Joost Batenburg, and J. Sijbers, "Fast and flexible X-ray tomography using the ASTRA toolbox," Opt. Express **24**(22), 25129 (2016).
112. W. J. Palenstijn, K. J. Batenburg, and J. Sijbers, "Performance improvements for iterative electron tomography reconstruction using graphics processing units (GPUs)," J. Struct. Biol. **176**(2), 250–253 (2011).
113. B. Goris, S. Bals, W. Van den Broek, E. Carbó-Argibay, S. Gómez-Graña, L. M. Liz-Marzán, and G. Van Tendeloo, "Atomic-scale determination of surface facets in gold nanorods," Nat. Mater. **11**(11), 930–935 (2012).
114. N. Winckelmans, T. Altantzis, M. Grzelczak, A. Sánchez-Iglesias, L. M. Liz-Marzán, and S. Bals, "Multimode Electron Tomography as a Tool to Characterize the Internal Structure and Morphology of Gold Nanoparticles," J. Phys. Chem. C **122**(25), 13522–13528 (2018).
115. S. Bals, B. Goris, T. Altantzis, H. Heidari, S. Van Aert, and G. Van Tendeloo, "Seeing and measuring in 3D with electrons," Comptes Rendus Phys. **15**(2–3), 140–150 (2014).
116. L. H. Germer, "Diffuse Rings Produced by Electron Scattering," Phys. Rev. **49**(2), 163–166 (1936).
117. L. A. Giannuzzi, R. Geurts, and J. Ringnalda, "2 keV Ga+ FIB Milling for Reducing Amorphous Damage in Silicon," Microsc. Microanal. **11**(S02), (2005).
118. A. Alba, R. M. Aguilar-Ponce, J. F. Vigueras-Gómez, and E. Arce-Santana, "Phase Correlation Based Image Alignment with Subpixel Accuracy," in *Advances in Artificial Intelligence*, I. Batyrshin and M. González Mendoza, eds., Lecture Notes in Computer Science (Springer Berlin Heidelberg, 2013), **7629**, pp. 171–182.
119. P. A. Penczek, "Fundamentals of Three-Dimensional Reconstruction from Projections," in *Methods in Enzymology* (Elsevier, 2010), **482**, pp. 1–33.
120. A. Pofelski, V. Whabi, S. Ghanad-Tavakoli, and G. Botton, "Assessment of the strain depth sensitivity of Moiré sampling Scanning Transmission Electron Microscopy Geometrical Phase Analysis through a comparison with Dark-Field Electron Holography," Ultramicroscopy **223**, 113225 (2021).

121. A. Sandryhaila and J. M. F. Moura, "Big Data Analysis with Signal Processing on Graphs: Representation and processing of massive data sets with irregular structure," IEEE Signal Process. Mag. **31**(5), 80–90 (2014).
122. D. Kosemura, S. Yamamoto, K. Takeuchi, K. Usuda, and A. Ogura, "Examination of phonon deformation potentials for accurate strain measurements in silicon–germanium alloys with the whole composition range by Raman spectroscopy," Jpn. J. Appl. Phys. **55**(2), 026602 (2016).
123. E. Anastassakis, A. Pinczuk, E. Burstein, F. H. Pollak, and M. Cardona, "Effect of static uniaxial stress on the Raman spectrum of silicon," Solid State Commun. **8**(2), 133–138 (1970).
124. I. D. Wolf, "Micro-Raman spectroscopy to study local mechanical stress in silicon integrated circuits," Semicond. Sci. Technol. **11**(2), 139–154 (1996).
125. I. Loa, S. Gronemeyer, C. Thomsen, O. Ambacher, D. Schikora, and D. J. As, "Comparative determination of absolute Raman scattering efficiencies and application to GaN," J. Raman Spectrosc. **29**(4), 291–295 (1998).
126. R. Loudon, "The Raman effect in crystals," Adv. Phys. **13**(52), 423–482 (1964).
127. J. A. Steele, P. Puech, and R. A. Lewis, "Polarized Raman backscattering selection rules for (*hhl*)-oriented diamond- and zincblende-type crystals," J. Appl. Phys. **120**(5), 055701 (2016).
128. M. Erdelyi, J. Simon, E. A. Barnard, and C. F. Kaminski, "Analyzing Receptor Assemblies in the Cell Membrane Using Fluorescence Anisotropy Imaging with TIRF Microscopy," PLoS ONE **9**(6), e100526 (2014).
129. K. Bahlmann and S. W. Hell, "Electric field depolarization in high aperture focusing with emphasis on annular apertures," J. Microsc. **200**(1), 59–67 (2000).
130. S. C. Tidwell, D. H. Ford, and W. D. Kimura, "Generating radially polarized beams interferometrically," Appl. Opt. **29**(15), 2234 (1990).
131. A. Yu, G. Chen, Z. Zhang, Z. Wen, L. Dai, K. Zhang, S. Jiang, Z. Wu, Y. Li, C. Wang, and X. Luo, "Creation of Sub-diffraction Longitudinally Polarized Spot by Focusing Radially Polarized Light with Binary Phase Lens," Sci. Rep. **6**(1), 38859 (2016).
132. X. Wang, H. Ren, and C. Nah, "Linearly to radially polarized light conversion and tight focus," J. Appl. Phys. **117**(24), 243101 (2015).
133. A. V. Krasavin, P. Segovia, R. Dubrovka, N. Olivier, G. A. Wurtz, P. Ginzburg, and A. V. Zayats, "Generalization of the optical theorem: experimental proof for radially polarized beams," Light Sci. Appl. **7**(1), 36 (2018).
134. M. Bashkansky, D. Park, and F. K. Fatemi, "Azimuthally and radially polarized light with a nematic SLM," Opt. Express **18**(1), 212 (2010).
135. C. F. Phelan, J. F. Donegan, and J. G. Lunney, "Generation of a radially polarized light beam using internal conical diffraction," Opt. Express **19**(22), 21793 (2011).
136. K. S. Youngworth and T. G. Brown, "Focusing of high numerical aperture cylindrical-vector beams," Opt. Express **7**(2), 77 (2000).
137. R. H. Jordan and D. G. Hall, "Free-space azimuthal paraxial wave equation: the azimuthal Bessel–Gauss beam solution," Opt. Lett. **19**(7), 427 (1994).
138. K. S. Youngworth and T. G. Brown, "Inhomogenous polarization in scanning optical microscopy," in J.-A. Conchello, C. J. Cogswell, A. G. Tescher, and T. Wilson, eds. (2000), pp. 75–85.
139. R. J. Harrach, "Electric Field Components in a Focused Laser Beam," Appl. Opt. **12**(1), 133 (1973).
140. T. S. Perova, J. Wasyluk, K. Lyutovich, E. Kasper, M. Oehme, K. Rode, and A. Waldron, "Composition and strain in thin Si1−xGex virtual substrates measured by micro-Raman spectroscopy and x-ray diffraction," J. Appl. Phys. **109**(3), 033502 (2011).
141. W. Liang, J. Li, and H. He, "Photo-Catalytic Degradation of Volatile Organic Compounds (VOCs) over Titanium Dioxide Thin Film," in *Advanced Aspects of Spectroscopy*, M. Akhyar Farrukh, ed. (InTech, 2012).
142. R. Ossikovski, Q. Nguyen, G. Picardi, and J. Schreiber, "Determining the stress tensor in strained semiconductor structures by using polarized micro-Raman spectroscopy in oblique backscattering configuration," J. Appl. Phys. **103**(9), 093525 (2008).

143. E. Anastassakis, A. Cantarero, and M. Cardona, "Piezo-Raman measurements and anharmonic parameters in silicon and diamond," Phys. Rev. B **41**(11), 7529–7535 (1990).
144. E. Anastassakis, "Strained superlattices and heterostructures: Elastic considerations," J. Appl. Phys. **68**(9), 4561–4568 (1990).
145. "Stress-strain equations," in *Handbook of Geophysical Exploration: Seismic Exploration* (Elsevier, 2003), **34**, pp. 61–68.
146. R. Camattari, L. Lanzoni, V. Bellucci, and V. Guidi, "*AniCryDe* : calculation of elastic properties in silicon and germanium crystals," J. Appl. Crystallogr. **48**(3), 943–949 (2015).
147. H. Mei, J. H. An, R. Huang, and P. J. Ferreira, "Finite element modeling of stress variation in multilayer thin-film specimens for in situ transmission electron microscopy experiments," J. Mater. Res. **22**(10), 2737–2741 (2007).
148. L. Clément, R. Pantel, L. F. Tz. Kwakman, and J. L. Rouvière, "Strain measurements by convergent-beam electron diffraction: The importance of stress relaxation in lamella preparations," Appl. Phys. Lett. **85**(4), 651–653 (2004).
149. M. Kakkala, "Vibrational spectroscopic studies of olivines, pyroxenes, and amphiboles at high temperatures and pressures," PhD Thesis, University of Hawaii at Manoa (1993).
150. S. K. Marella and S. S. Sapatnekar, "The impact of shallow trench isolation effects on circuit performance," in *2013 IEEE/ACM International Conference on Computer-Aided Design (ICCAD)* (IEEE, 2013), pp. 289–294.
151. "Phases and Crystal Structures," in *Pergamon Materials Series* (Elsevier, 2007), **12**, pp. 1–86.
152. Prabhakara, Viveksharma, Jannis, Daen, Guzzinati, Giulio, Béché, Armand, Bender, Hugo, and Verbeeck, Johan, "Block scanning strain measurement in Transmission electron microscope," (2020).
153. M. J. Williamson, P. van Dooren, and J. Flanagan, "Effects of Image Processing on Electron Diffraction Patterns Used for Nanobeam Diffraction Strain Measurements," (n.d.).
154. JEOL, "Scanning Electron Microscope A to Z," (n.d.).
155. A. Tarun, N. Hayazawa, and S. Kawata, "Tip-enhanced Raman spectroscopy for nanoscale strain characterization," Anal. Bioanal. Chem. **394**(7), 1775–1785 (2009).
156. T. Yano, T. Ichimura, S. Kuwahara, F. H'Dhili, K. Uetsuki, Y. Okuno, P. Verma, and S. Kawata, "Tip-enhanced nano-Raman analytical imaging of locally induced strain distribution in carbon nanotubes," Nat. Commun. **4**(1), 2592 (2013).
157. *Titan Condenser Manual* (n.d.).
158. D. B. Williams and C. B. Carter, *Transmission Electron Microscopy* (Springer US, 2009).
159. "Incoherent imaging of crystals using thermally scattered electrons," Proc. R. Soc. Lond. Ser. Math. Phys. Sci. **449**(1936), 273–293 (1995).
160. F. Hüe, M. Hÿtch, H. Bender, F. Houdellier, and A. Claverie, "Direct Mapping of Strain in a Strained Silicon Transistor by High-Resolution Electron Microscopy," Phys. Rev. Lett. **100**(15), 156602 (2008).
161. N. B. Kavukcuoglu and N. Pleshko, "Infrared and Raman Microscopy and Imaging of Biomaterials," in *Comprehensive Biomaterials* (Elsevier, 2011), pp. 365–378.
162. M. Bauer, A. M. Gigler, A. J. Huber, R. Hillenbrand, and R. W. Stark, "Temperature-depending Raman line-shift of silicon carbide: Temperature-depending Raman line-shift of silicon carbide," J. Raman Spectrosc. **40**(12), 1867–1874 (2009).
163. R. Petry, M. Schmitt, and J. Popp, "Raman Spectroscopy-A Prospective Tool in the Life Sciences," ChemPhysChem **4**(1), 14–30 (2003).